8-30-2019

Lithium-Ion Hybrid Capacitor Devices: Towards High-Performance Electrochemical Capacitive Energy Storage

Ebenezer Dotun Adelowo
Florida International University, eadel004@fiu.edu

FLORIDA INTERNATIONAL UNIVERSITY

Miami, Florida

LITHIUM-ION HYBRID CAPACITOR DEVICES: TOWARDS HIGH-PERFORMANCE ELECTROCHEMICAL CAPACITIVE ENERGY STORAGE

A dissertation submitted in partial fulfillment of the

requirements for the degree of

DOCTOR OF PHILOSOPHY

in

MATERIALS SCIENCE AND ENGINEERING

by

Ebenezer Dotun Adelowo

2019

To: Dean John L. Volakis
College of Engineering and Computing

This dissertation, written by Ebenezer Dotun Adelowo, and entitled Lithium-Ion Hybrid Capacitor Devices: Towards High-performance Electrochemical Capacitive Energy Storage, having been approved in respect to style and intellectual content, is referred to you for judgment.

We have read this dissertation and recommend that it be approved.

_____
Norman D. H. Munroe

_____
Nezih Pala

_____
Wenzhi Li

_____
Benjamin Boesl

_____
Chunlei Wang, Major Professor

Date of Defense: August 30, 2019

The dissertation of Ebenezer Dotun Adelowo is approved.

_____
John L. Volakis
Dean of College of Engineering and Computing

_____
Andrés G. Gil
Vice President for Research and Economic Development
and Dean of the University Graduate School

Florida International University, 2019

DEDICATION

I dedicate this dissertation to God Almighty, the giver of all good things.

ACKNOWLEDGMENTS

I express my deep gratitude to my advisor, Dr. Chunlei Wang for her encouragement and support throughout my doctoral studies at Florida International University (FIU). I am indeed very thankful to her for providing me with several opportunities and giving dedicated effort, guidance and tremendous patience towards developing my research skills during my time in her group.

I appreciate Dr. Norman Munroe, Dr. Benjamin Boesl, Dr. Nezih Pala and Dr. Whenzi Li, for accepting to serve as members of my dissertation committee. I thank them for their valuable input and support towards my dissertation. I also appreciate Dr. Bilal El-Zahab and Dr. Meer Safa for giving several valuable suggestions on my research work.

Many thanks to my amazing colleagues in Dr. Wang's research group. I thank Chunhui Chen, Yong Hao, Richa Agarwal Amin Rabiei, Iman Khakpour, Omena Okpowe, and Shahrzad Forouzanfar who encouraged and supported me, especially during difficult periods.

I acknowledge the Advanced Materials Engineering Research Institute (AMERI) at FIU for providing excellent facilities for my experiments. I highly appreciate Mr. Patrick Roman, Dr. Alex Franco. Steward Schwarz and Jonathan Comparan for their time in providing training support on several equipment for my experiments in the institute.

I also acknowledge all funding sources that made this doctoral research a reality. I recognize funding from the national science foundation (NSF) and I thank the department of mechanical and materials Engineering (MME) at FIU for supporting me through teaching assistantship. I am also very grateful to the university graduate school (UGS) at FIU for supporting me through Dissertation Year Fellowship (DYF) awards.

I would like to thank my parents Prof. and Mrs. Adelowo for helping in shaping my life with love, kindness and positivity. To my wife Abimbola, and my daughters, Alexandra and Katerina, I cannot thank you enough for the great sacrifices you made individually and collectively. I appreciate your unconditional love and support throughout my studies.

ABSTRACT OF THE DISSERTATION

LITHIUM-ION HYBRID CAPACITOR DEVICES: TOWARDS HIGH-PERFORMANCE ELECTROCHEMICAL CAPACITIVE ENERGY STORAGE

by

Ebenezer Dotun Adelowo

Florida International University, 2019

Miami, Florida

Professor Chunlei Wang, Major Professor

Hybridization of lithium-ion batteries (LIBs) and electrochemical capacitors (ECs) at electrode level can potentially provide high-performance capacitive energy storage having a good combination of high energy density, high power density, and moderate cycling longevity. Lithium-ion hybrid capacitor (LIHC) system consisting of battery-type and capacitor-type electrodes represents an attractive hybridization approach aimed at bridging the performance gap between the two energy storage systems. The application of such an energy storage system may extend the functionalities of many electronic devices.

The battery-type electrode in LIHCs restrains their power densities due to sluggish lithium-ion storage kinetics. On the other hand, the limited specific capacity of the capacitor-type electrode is a restraining factor for high energy density in the hybrid system. In this regard, the push for high-performance LIHCs highlights the importance of the application of new electrode materials combination capable of providing high capacity and

rapid lithium storage kinetics. Reduced graphene oxide-carbon nanotubes (rGO-CNT) prepared by electrostatic spray deposition exhibits high specific capacity, high rate capability, and fast ion transport kinetics, thus making it an attractive candidate for LIHC. A LIHC system comprising rGO-CNT material as both anode and cathode was assembled and studied using an organic liquid electrolyte. Both electrochemical and direct lithium contact prelithiation approaches were explored to achieve high electrochemical performance in the system. The LIHCs show high electrochemical performance output intermediate between the energy density and power density characteristics of LIBs and ECs.

A novel on-chip LIHC with 3D interdigital carbon microelectrode platform derived by carbon microelectromechanical systems (C-MEMS) technique to address the need for high-performance compact and integrable ECs for microelectronic devices. The 3D carbon structures played the dual role of the current collector and capacitor electrode, while $LiFePO_4$ was employed as the battery-type electrode. The on-chip LIHC generated a maximum footprint area normalized energy density of about 5.03 $\mu Wcm^{-2,}$ which was about five times more than symmetric ECs of the same footprint area.

This study opens a new path for realizing high-performance LIHC by exploiting the fast and high capacity surface storage properties of rGO-CNT electrode fabricated by electrostatic spray deposition as well as the extension of LIHC concept to C-MEMS based on-chip ECs. The application of the rGO-based electrode as both anode and cathode suggest new possibilities for the development of high-performance LIHC. Additionally, the C-MEMS approach employed represents a facile and CMOS processing-compatible method for the development of on-chip LIHC. The study also broadens the prospects of the application of a high aspect ratio 3D platform based on C-MEMS technology beyond symmetric on-chip ECs.

TABLE OF CONTENTS

LIST OF TABLES

TABLE PAGE

LIST OF FIGURES

FIGURE PAGE

CHAPTER 1

Introduction

1.1 Overview

The continuous development of mobile electronics, electrified transportation systems, and renewable energy sources has created an ever-growing demand for energy storage devices capable of providing high-performance characteristics. The key performance features of an ideal energy storage device are high energy-power density output and excellent cyclability. Among the energy storage devices, batteries are attractive because they are essentially based on a simple concept and exhibit the ability to moderately meet the requirements of many electronic devices. They typically consist of two electrodes with different chemical potential internally connected together with an ionic conductor (electrolyte) in-between them [1]. For primary batteries, when the two electrodes are externally connected, electrons flow spontaneously from the more negative potential to the more positive electrode to reach a charge balance. Secondary or rechargeable batteries work on the same principle as primary batteries but the charge storage process is reversible. However, there is a concern about the ability of battery technology to adequately meet the growing demands of various electronic devices currently in existence and emerging ones. Rechargeable lithium-ion batteries (LIBs) have been key enabler for energy storage technology applied in many electronic devices providing high volumetric (ca. 650 Whl^{-1}) and gravimetric energy densities (ca. 250 $Whkg^{-1}$) [2]. Considering the energy storage process in LIBs, lithium-ions are inserted in the bulk of electrode materials through

faradaic redox reactions providing the high energy density characteristics. However, the storage process is diffusion-controlled and slow which limits their power density output [3]. Moreover, the redox reactions in LIBs present challenges related to low reversibility, instabilities of the electrode materials, and unpredictable side reactions at electrode-electrolyte interface, limiting their cyclability. Solutions to these challenges require efforts on new electrode structures and optimizing their compatibility with electrolytes [4]. Extensive research efforts have significantly improved the performance level of LIBs over the years, but redox reaction storage principle still restricts their power density output and cyclability.

Electrochemical capacitors (ECs) or supercapacitors are capable of providing high power density (i.e., rapid power uptake and delivery) over multiples of thousands of cycles [5,6]. ECs are similar to batteries in construction with a two-electrode setup and a suitable electrolyte between them. But unlike batteries, ECs store charges physically by an electric double layer mechanism at the interface between the electrolyte and high surface area electrodes (e.g activated carbon(AC)) [7]. A potential build-up takes place at each electrode-electrolyte interfacial region during charge operation leading to the attraction and adsorption of electrolyte ion of opposite charges to the electrode [8]. The reverse occurs during discharge with a rapid release of the adsorbed ions. This process is non-diffusion controlled, which explains why ECs are able to provide rapid power uptake and delivery as well as high cycling longevity. Electrolytes employed in ECs may be aqueous, organic, or ionic liquids [9]. However, the main drawback of ECs is their low energy density which hinders their widespread application in electronic devices [10]. Another mechanism of ECs known as ‘pseudocapacitance’ is based on surface limited redox reactions using electrodes

such as transition metal oxides or conducting polymers. Pseudocapacitance mechanism can boost the energy density of ECs but not to the level achievable in batteries involving bulk storage mechanism. Moreover, ECs based on pseudocapacitive electrodes usually exhibit poor electrical conductivity, structural instability and overall, the ECs usually give lower power density output than those based on electric double-layer mechanism [6].

ECs have been improved by the concept of hybridization where one of the electrodes in the electrochemical energy storage device is based on surface storage mechanism, while the other electrode is dominated by bulk storage process. The emergence of lithium-ion hybrid capacitors (LIHCs) is considered a promising hybridization approach capable of effectively overcome the poor energy density limitation of ECs (5-10 $Whkg^{-1}$) [11,12]. A LIHC system is primarily the internal combination of LIB and EC at electrode level. For instance, LIHCs may consist of graphite as the batter-type electrode and AC as the capacitor-type electrode. During charge/discharge operation of the system, intercalate/deintercalation of lithium-ions takes place in the graphite while anion adsorption/desorption process occurs in the AC giving higher working voltage and higher energy density compared to ECs [13]. LIHCs typically involves the consumption of both electrolyte cations and anions to give faster kinetics than the “rocking-chair” type reaction in LIBs [14]. Based on its working principle, LIHCs are of great interest to serve as a single standalone energy storage units with the ability to provide high energy and high power density characteristics for existing and emerging electronic devices.

1.2 Research Objectives and Approaches

Figure 1.1 shows the flow chart of the research plan in this dissertation. The ultimate goal is to develop new concepts to realize high energy density and high power density scale-up and on-chip hybrid ECs based on LIHC system. Traditional LIHCs comprising the combination of a battery-type and a capacitor-type electrodes giving bulk storage and surface storage mechanisms, respectively, present kinetics imbalance. Additionally, there is usually a significant disparity between the specific capacities of the anode and cathode materials in LIHCs. The surface storage process in capacitor-type electrodes offers significantly lower specific capacities than battery-type electrodes which tend to restrict the energy density output of LIHCs [15]. Furthermore, while the battery-type electrodes enable high energy density, they exhibit poor cyclability which represents a major obstacle against reaching high cycling longevity in the electrochemical energy storage system[16,17]. Thus, modifying or designing new materials to ensure the improved kinetics and specific capacity matching between the anode and cathode is of great significance for enhancing the electrochemical performance LIHCs. In this dissertation, we fabricated reduced graphene oxide-carbon nanotubes electrode (rGO-CNT) film as an electrode material capable of providing high capacity and fast ion transport kinetics. The electrochemical performance of a LIHC system using the material as both anode and cathode was examined. Two anode prelithiation approaches, electrochemical and direct lithium were explored to achieve high electrochemical performance in the all rGO-based LIHC.

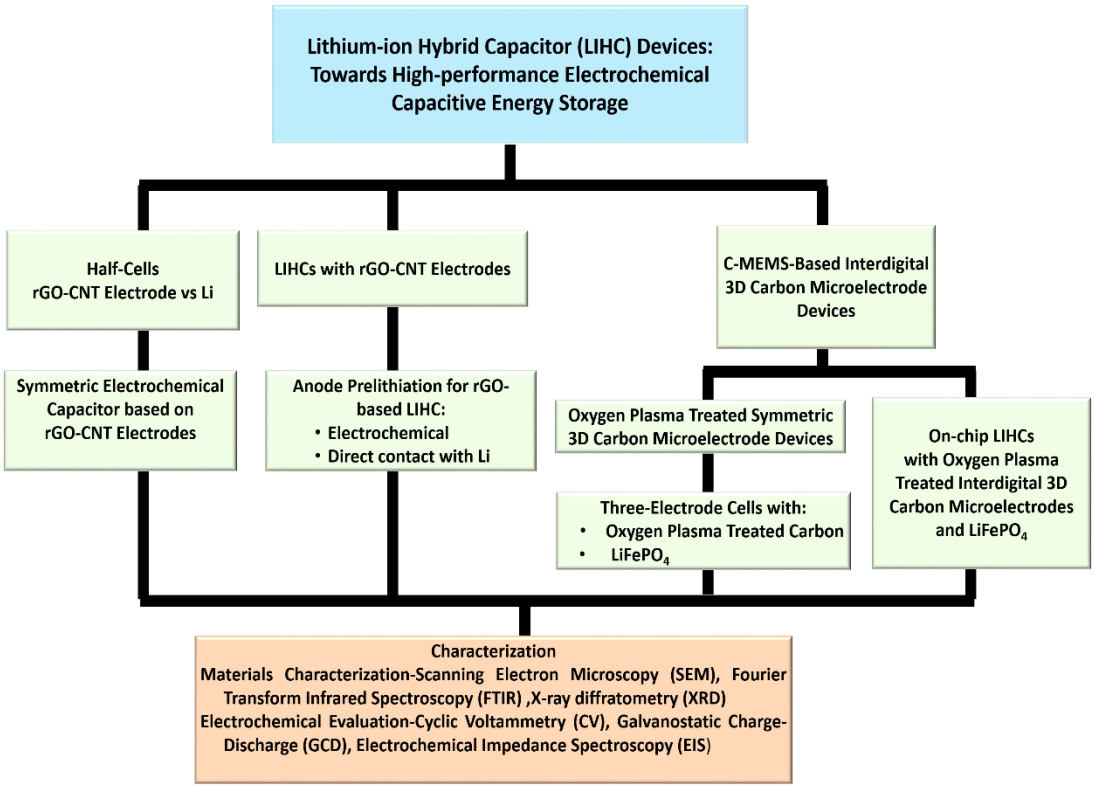

Figure 1.1: Research plan

Despite the promising performance features of LIHCs, fewer efforts have been directed towards its miniaturization for on-chip energy storage units to meet the demands of microelectronic devices. On-chip LIHC can facilitate autonomy and advanced capability for future and existing miniature electronic devices such as wireless communication systems or energy harvesting devices, or other devices where microscale energy storage units with high energy and high power densities are required. Under this condition, the performance of an on-chip LIHC will not only be influenced by electrode material properties, design concept adopted will play significant role because of footprint area constraints. Design concepts that can enable high mass loading of electrode materials are essential in building high-performance on-chip LIHCs. In this regard, 3D microelectrode

architecture is more advantageous than planar designs. In this dissertation, a 3D interdigital carbon microelectrode platform derived by carbon microelectromechanical systems (C-MEMS) technique was used to realize an on-chip LIHC and examined. This study adds important literature not only to miniaturized energy storage systems but also to the development of high aspect ratio 3D platform based on C-MEMS technology beyond symmetric microsupercapacitors.

1.3 Hypotheses

The electrochemical performance of LIHC depends on the charge storage characteristics of each electrode as previously mentioned. A high charge storage capacity in both electrodes of the hybrid system is of utmost importance. The most widely used porous carbon cathode materials do not offer sufficient capacity to improve the electrochemical performance of LIHCs. Moreover, typical anode materials used in LIHCs based on bulk storage mechanism exhibit kinetics limitations. A high charge storage capacity, however, can be achieved with carefully designed rGO-based materials as cathode to replace porous carbon materials in LIHCs. Similarly, rGO-based material can give high surface lithium storage capacity when employed as the anode. However, their optimal electrochemical performance properties are not fully realized due to restacking of their layers during cycling. It is therefore posited that the introduction of CNT in rGO will minimize the restacking problem, improve its charge storage kinetics, and enable enhanced discharge capacity. Anode prelithiation in LIHC with the resulting rGO-CNT electrodes will enable wider operating voltage range and higher energy density than symmetric EC.

For microscale on-chip ECs, facile scalable fabrication processing techniques exhibiting high footprint area performance is still challenging. It is posited that well-designed porous 3D carbon structures derived by C-MEMs technique can play the dual role of a current collector as well as the capacitor-type electrode for a simplified fabrication of on-chip symmetric ECs. The energy density of the on-chip ECs can be further improved by hybridization through the integration of LFP as the battery-type cathode material.

1.4 Scope of the Dissertation

Chapter 2 provides background information about capacitive energy storage and basic energy storage principles of LIHCs. It also discusses the electrode materials and electrolytes employed in the hybrid system. Chapter 3 discusses the methodology adopted in this dissertation. Chapter 4 presents the results of ESD-based rGO-CNT as both anode and cathode for LIHC. The half-cell electrochemical performance of the material were evaluated with lithium metal as the counter and reference electrode. The anode was first electrochemically prelithiated before coupling with fresh rGO-CNT as cathode to realize the LIHC. Chapter 5 discusses the direct contact prelithaition approach for the rGO-based LIHC. Chapter 6 focusses on the development of on-chip LIHC with 3D interdigital carbon microelectrode platform. The 3D carbon microelectrode platform was derived by carbon microelectromechanical systems (C-MEMS) technique and used as both the current collector and capacitor electrode, while LFP was employed as the battery-type electrode. Chapter 7 gives a summary of the main findings from this work and provide the direction for future efforts.

1.5 References

1. Yan J, Wang Q, Wei T, Fan Z. Recent Advances in Design and Fabrication of Electrochemical Supercapacitors with High Energy Densities. *Adv Energy Mater*. 2014;4:1300816. doi:10.1002/aenm.201300816.

2. Manthiram A. An Outlook on Lithium Ion Battery Technology. *ACS Cent Sci*. 2017;3:1063-1069. doi:10.1021/acscentsci.7b00288.

3. Simon P, Gogotsi Y, Dunn B. Where Do Batteries End and Supercapacitors Begin? *Science* 2014;343(March):1210-1212. doi:10.1126/science.1249625.

4. Choi JW, Aurbach D. Promise and reality of post-lithium-ion batteries with high energy densities. *Nat Rev*. 2016;1. doi:10.1038/natrevmats.2016.13.

5. Miller J, Simon P. Electrochemical Capacitors for Energy Management. *Science (80-).* 2008;321(August):651-653. doi:10.1126/science.1158736.

6. Zhai Y, Dou Y, Zhao D, Fulvio PF, Mayes RT. Carbon Materials for Chemical Capacitive Energy Storage. *Adv Mater*. 2011;23:4828-4850. doi:10.1002/adma.201100984.

7. Zhang S, Pan N. Supercapacitors Performance Evaluation. *Adv Energy Mater*. 2015;5:1-19. doi:10.1002/aenm.201401401.

8. Salanne M, Rotenberg B, Naoi K, et al. Efficient storage mechanisms for building better supercapacitors. *Nat energy*. 2016;1. doi:10.1038/NENERGY.2016.70.

9. Béguin F, Presser V, Balducci A, Frackowiak E. Carbons and Electrolytes for Advanced Supercapacitors. *Adv Mater*. 2014;26:2219-2251. doi:10.1002/adma.201304137.

10. Zhao H, Liu L, Vellacheri R, Lei Y. Recent Advances in Designing and Fabricating Self-Supported Nanoelectrodes for Supercapacitors. *Adv Sci*. 2017;4. doi:10.1002/advs.201700188.

11. Naoi K, Ishimoto S, Jun-ichi M, Wako N. Environmental Science Second generation ‘ nanohybrid supercapacitor ’: Evolution of capacitive. *Energy Environ Sci*. 2012;5:9363-9373. doi:10.1039/c2ee21675b.

12. Jagadale A, Zhou X, Xiong R, Dubal DP, Xu J, Yang S. Lithium ion capacitors (LIHCs): Development of the materials. *Energy Storage Mater*. 2019;(December 2018). doi:10.1016/j.ensm.2019.02.031.

13. Cericola D, Kötz R. Electrochimica Acta Hybridization of rechargeable batteries and electrochemical capacitors : Principles and limits. *Electrochim Acta*. 2012;72:1-17. doi:10.1016/j.electacta.2012.03.151.

14. Wang H, Zhu C, Chao D, Yan Q, Fan HJ. Nonaqueous Hybrid Lithium-Ion and Sodium-Ion Capacitors. *Adv Mater*. 2017;29:1702093. doi:10.1002/adma.201702093.

15. Han P, Xu G, Han X, Zhao J, Zhou X, Cui G. Lithium Ion Capacitors in Organic Electrolyte System : Scientific Problems , Material Development , and Key Technologies. *Adv Energy Mater*. 2018;8:1801243. doi:10.1002/aenm.201801243.

16. Aravindan V, Gnanaraj J, Lee Y, Madhavi S. Insertion-Type Electrodes for Nonaqueous Li-Ion Capacitors. *Chem Rev*. 2014;114:11619-11635. doi:10.1021/cr5000915.

17. Zuo W, Li R, Zhou C, Li Y, Xia J, Liu J. Battery-Supercapacitor Hybrid Devices : Recent Progress and Future Prospects. *Adv Sci*. 2017;4:16000539. doi:10.1002/advs.201600539.

18. Li B, Zheng J, Zhang H, et al. Electrode Materials , Electrolytes , and Challenges in Nonaqueous Lithium-Ion Capacitors. *Adv Mater*. 2018;30:1-19. doi:10.1002/adma.201705670.

CHAPTER 2

Background and Literature Review

2.1 Historical Overview

Capacitive energy storage has come of age since the invention of the Leyden Jar, the first known capacitor in the 1740s [1]. Thereafter, the two-plate conventional capacitor was invented, but these early inventions can only store small amounts of energy due to the area and geometric constraints. In the 19th century, however, von Helmholtz gave an insight into capacitive energy storage at the interfaces between two metal electrodes and liquid electrolytes [2]. He described the electrical double layer concept when he revealed the behavior of oppositely charged ions at electrode/electrolyte interface. He proposed that a double layer of opposite charges are formed at the interface between electrode and electrolyte with an atomic distance separation as illustrated in Figure 2.1a. Gouy and Chapman modified the concept involving the presence of a continuous distribution of electrolyte ions which gives rise to what they described as diffusion layer Figure 2.1b. The Gouy-Chapman However, model results in the overestimation of capacitance. Later, the presence of two regions of ion distribution; the compact layer and the diffuse layer was described by Stern (Figure 2.1c). The Stern model is a combination of the Helmholtz and Gouy–Chapman concepts earlier described. The two ion distribution zones are separated by the inner and outer Helmholtz planes. The overall double layer capacitance C_{dl} , can be expressed by equation 2.1, where C_H and C_{diff} are the capacitance of the compact and diffusion regions, respectively.

$$\frac{1}{C_{dl}} = \frac{1}{C_H} + \frac{1}{C_{diff}} \qquad (2.1)$$

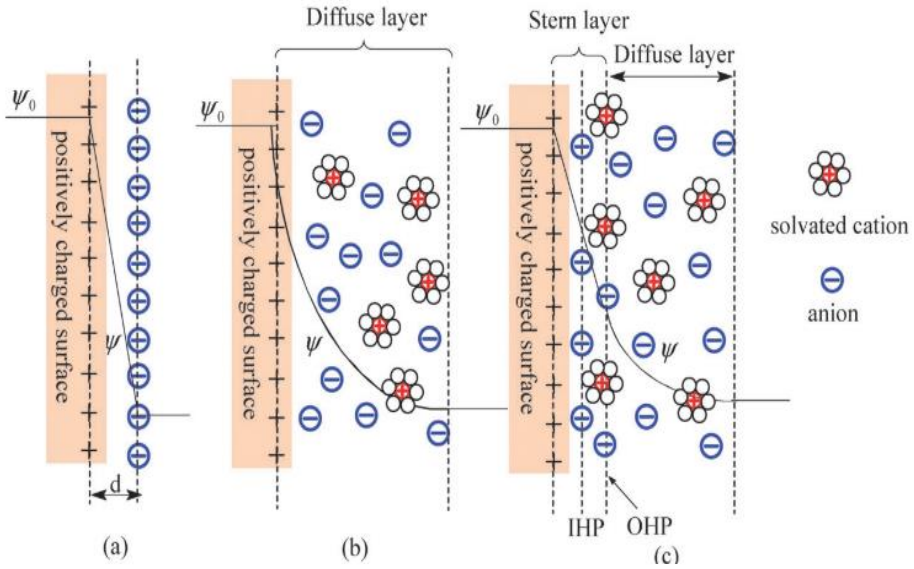

Figure 2.1: Schematic illustration of (a) Helmholtz model, (b) Gouy–Chapman model, and (c) Stern model, showing the inner Helmholtz plane and outer Helmholtz plane [2].

Following these early concepts, H. I Becker of General Electric demonstrated the first EC in 1954 using highly porous carbon electrodes with aqueous electrolyte [3]. An illustration of the capacitive storage mechanism in porous electrode materials is presented in Figure 2.2. As indicated, the EC construction is like two capacitors with capacitance C_1 and C_2 connected in series. Capacitive behavior in porous electrodes is somewhat more complicated than planar electrodes. In this type of EC, several parameters such as ion transport in sub-micron pore and electrolyte properties play important role in the determination of capacitance output. Robert Rightmire working for Standard Oil Company of Ohio (SOHIO) later invented the first EC with non-aqueous electrolytes which could give higher voltage range and much higher energy density than Becker's EC [4].

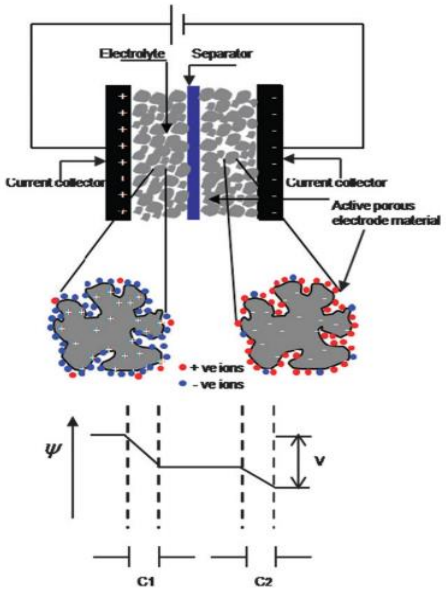

Figure 2.2: An illustration of the double layer storage mechanism in porous electrode materials [2].

A different capacitive storage mechanism in ECs known as pseudocapacitance was demonstrated with RuO_2 in 1971[5]. The mechanism involves surface faradaic reaction and therefore exhibit rapid charge-discharge characteristic like double-layer mechanism. Although the ECs can provide higher energy density than double-layer ECs, the high cost of RuO_2 constitute a major constraint towards its further commercialization. The field of capacitive energy storage has since advanced due to increasing amounts of possible applications. New insights over the past years have led to the emergence of new materials and capacitive energy storage concepts.

Hybrid capacitors are relatively new energy storage devices based on mixing two energy storage mechanisms internally in a single device for enhanced electrochemical performance [6]. In 2001, Amatucci et al. demonstrated the LIHC concept, a lithium-based hybrid capacitor enabled by two dissimilar storage mechanism involving faradaic

reversible lithium-ion intercalation obtainable in LIBs at the anode, while non-faradaic storage process (like ECs) occurs at the cathode [7]. The Ragone plot in Figure 2.3 shows the performance range of LIHC, LIBs, and ECs in terms of energy and power density.

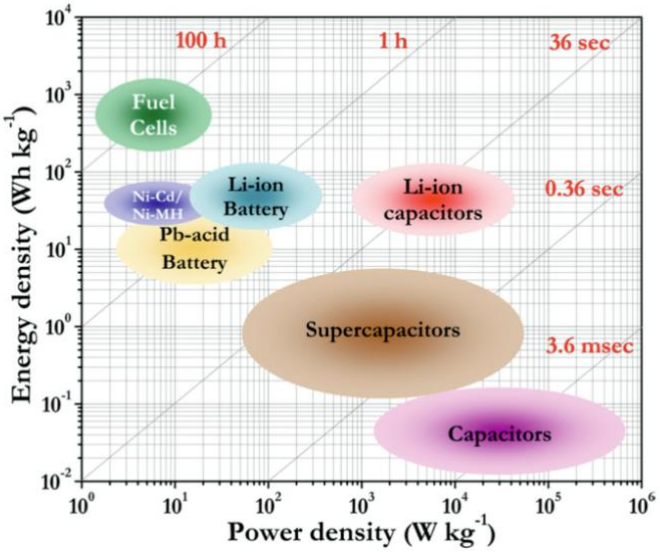

Figure 2.3: Ragone plot showing LIHC with other energy-storage devices [8].

The energy storage principles in LIHCs offer an opportunity to widen the energy-power density output of capacitive energy storage beyond LIBs and ECs individually. LIHC is able to withstand fast charging operation without the risk of hazardous lithium plating and subsequent cell deterioration [7]. The energy density of LIBs is almost stable when discharge operation is slow [9]. However, LIBs typically show deteriorating energy densities during fast discharge due to their bulk storage mechanism. ECs with double-layer surface storage mechanism can provide fast discharge operation up to milliseconds without significant energy density deterioration. In terms of fast charge/discharge, LIHC can provide optimal performance between the domains of ECs and LIBs which may effectively meet the need of present and future electronic devices.

2.2 Fundamentals of LIHC Operation

In order to gain insight into the operating principles of LIHCs, it is essential to first consider the energy storage mechanism of both ECs and LIBs, which are the internal energy storage components of the system. In this section, we will discuss ECs and LIBs with a focus on their basic operating principles. Thereafter, we discuss the operating principle resulting from combining the two mechanisms, thus creating the LIHC system.

2.2.1 Working Principles of ECs

The charge storage mechanism of ECs involves the well-recognized non-faradaic process in which electrostatic attraction and adsorption of electrolyte ions on electrode surface occur, resulting in the formation of double layers of opposite charges at electrode-electrolyte interface (electric double layer capacitance (EDLC)) [10]. EDLC electrode materials are mainly highly porous carbon, capable of providing high surface area for double layer formation. Based on Helmholtz model, the double-layer capacitance C can be expressed by equation 2.6:

$$C = (\varepsilon_r \varepsilon_0) A/d \qquad (2.6)$$

where ε_r is the relative permittivity of electrolyte, ε_0 represents the permittivity of vacuum, A is the electrode surface area and d represents the thickness of the double layer. One of the strategies of improving the overall performance of EDLC concept is to study the dependence of capacitance on electrode area and pore structure [11].

Another family of ECs involving faradaic redox reactions, pseudocapacitance, are based on electrochemical adsorption of ions at electrode surface which may result in higher

energy densities than EDLC mechanism [12]. As schematically illustrated in Figure 2.4, the three types of electrochemical processes that can generate pseudocapacitance include; (a) underpotential deposition,(b) redox pseudocapacitance (c) intercalation pseudocapacitance. Underpotential takes place when a monolayer of metal ion is adsorbed on a metal surface having higher redox potential. In underpotential deposition, metal ions adsorb on a different metal surface well above their redox potential forming a monolayer. An example is the deposition of lead on gold surface. Redox pseudocapacitance typically involves faradaic process where ions are adsorbed on the surface of a material accompanied by charge-transfer. Intercalation pseudocapacitance describes when electrolyte ion intercalate into the bulk or layers of redox-active material by faradaic charge-transfer process without any phase transformation [13].

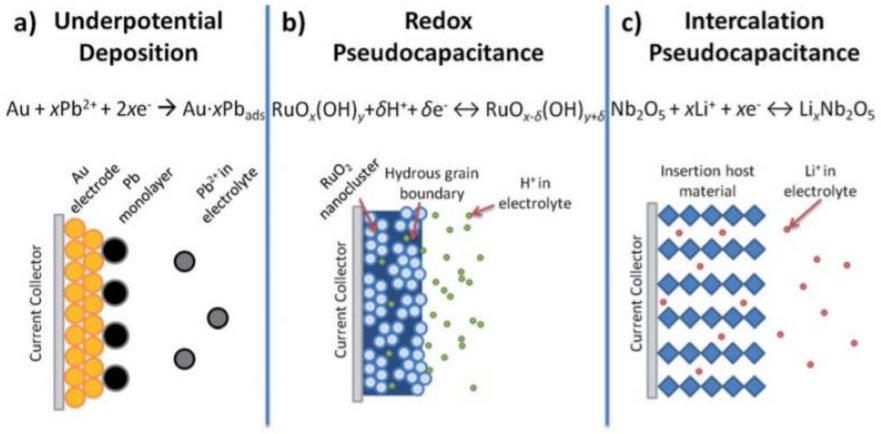

Figure 2.4: Schematic illustration of different electrochemical reactions resulting in pseudocapacitance [13].

Typically transition metal oxides such as RuO_2, MnO_2 or conductive polymers such as polyaniline and polypyrrole give pseudocapacitive properties. A lot of progress has been made with the development of new nanostructured materials aimed at providing high

pseudocapacitance. However, more efforts on how the pseudocapacitance depends on redox chemistry and the structure of the materials are still required [14].

The intrinsic electrode and electrolyte properties determine the optimal performance output of ECs. A significant advantage is realized if ECs are operated in non-aqueous electrolyte rather than aqueous electrolyte because non-aqueous electrolyte exhibit substantially high decomposition voltages (ca 3.5 to 4 V). In practical terms, not only is the decomposition voltage crucial for EC design, it favors the solubility of electrolyte salt in a given solvent. The theoretical energy density achievable in non-aqueous electrolyte can be up 16 times larger than employing aqueous electrolyte media [12].

2.2.2 **Working Principles of LIBs**

As previously mentioned, LIB construction is based on anode and cathode materials with a lithium-based electrolyte sandwiched between them. A simplified description of the basic LIB operating principle is the reversible redox reaction involving reversible lithium-ion intercalation/ deintercalation between the two electrodes through the electrolyte. Lithium deintercalation typically takes place in cathode materials at ca. 3 - 4 V vs lithium while intercalation occurs in anode materials at ca. 0 – 1.5 V vs lithium [15]. The principle of operation of LIBs is schematically illustrated in Figure 2.5 using $LiCoO_2$ cathode and carbon anode (e.g graphite). The half-cell reactions in the cathode and anode are presented in equations 2.2 and 2.3, respectively. The overall full cell reaction is presented in equations 2.4. During charge operation, lithium-ions migrate from the cathode which has higher potential and inserted into the lower potential anode. Thereafter, electron flow takes place from the cathode to the anode through an external circuit. The reverse

scenario plays out during discharge with 100 % efficiency in an ideal cell [16]. A surface film known as the solid electrolyte interface (SEI) is usually formed during this process to passivate the electrode material and prevent undesirable reactions. The SEI formation mechanism and stability plays a key role in the capacity and cyclability of the lithium-ion cell [17]. However, side reactions or abuse conditions limit the efficiency of the energy storage technology during cycling. Side reactions may consume lithium and/or active materials leading to gradual cell capacity degradation. Moreover, the by-products of the side reactions may generate a barrier on the surface of the active materials and prevent easy access of lithium-ions, leading to a poor performance of the cell at high charge/discharge rate.

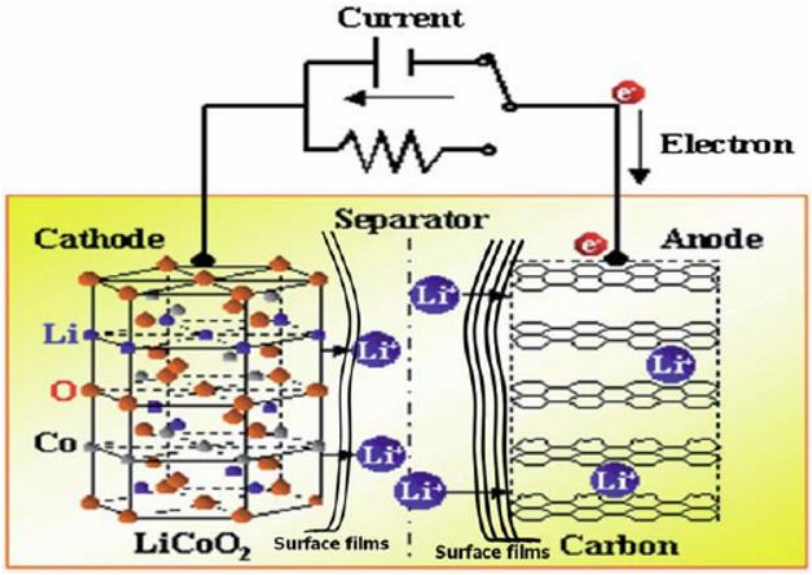

Figure 2.5: The general principle of operation of LIBs with $LiCoO_2$ cathode and carbon anode [16].

$$LiCoO_2 \leftrightarrow \frac{1}{2}Li^+ + \frac{1}{2}e^- + Li_{0.5}CoO_2 \qquad (2.2)\ \text{(Cathode reaction)}$$

$$C_6 + Li^+ + e^- \leftrightarrow LiC_6 \qquad (2.3)\ \text{(Anode reaction)}$$

$$CoO_2 + LiC_6 \leftrightarrow LiCoO_2 + C_6 \qquad (2.4)\ \text{(Overall cell reaction)}$$

A good understanding of the role of SEI is a crucial step in preventing undesirable side reaction in LIBs. Figure 2.6 shows the relative electron energy characteristics in the electrodes and electrolyte of a LIB in thermodynamic equilibrium condition [18**]**.

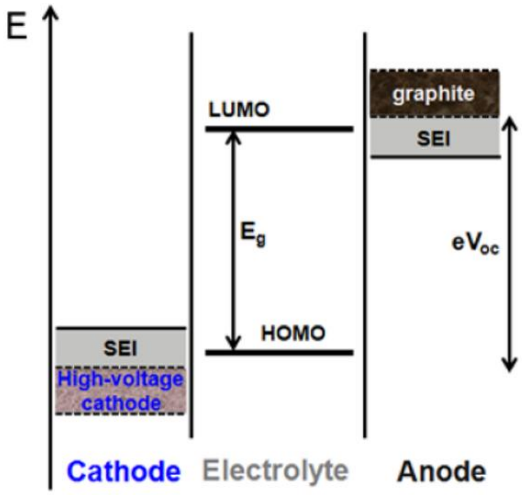

Figure 2.6: Energy levels of anode, cathode and electrolyte at open-circuit voltage [18**]**.

Generally, anode materials in LIBs are reducing agents while the cathode materials are oxidizing agents. The electrolyte window is determined by the energy separation E_g of the lowest unoccupied molecular orbital (LUMO), and the highest occupied molecular orbital (HOMO) of the electrolyte. Anodes exhibit chemical potential μ_A above the LUMO which may lead to electrolyte reduction except a passivating SEI layer exists. The passivation layer will prevent the reduction by blocking the transfer of electrons from the anode to the electrolyte. On the cathode side, the chemical potential μC is below HOMO. Therefore, the cathode may oxidize the electrolyte in the absence of SEI layer to block electron

transfer at electrode-electrolyte interface. The open-circuit voltage eV_{oc} can be expressed in term of as of μ_A, μ_c and E_g by equation 2.5. In order to achieve thermodynamic stability, μ_A and μ_c should be located within the electrolyte window. A very important subject of research over the years is to develop electrolytes compatible with both electrodes and exhibit wide window of operation [19].

$$eV_{oc} = \mu_A - \mu_c \quad \leq E_g \qquad (2.5)$$

2.2.3 **Working Principles of LIHCs**

The primary advantage of LIHCs realized by the combination of EC and LIB at electrode level is their potential to provide high energy density without significant power density loss. Figure 2.7 provides an illustration of energy storage process of the three systems. Pioneering hybridization of EC and LIB employed AC as EC electrode for high power density characteristic, while lithium-containing intercalation compound, $Li_4Ti_5O_{12}$ (LTO) was used as LIB electrode to provide high energy density [7]. Anion adsorption occurs on the AC electrode surface, while lithium-ion intercalation takes place in LTO simultaneously.

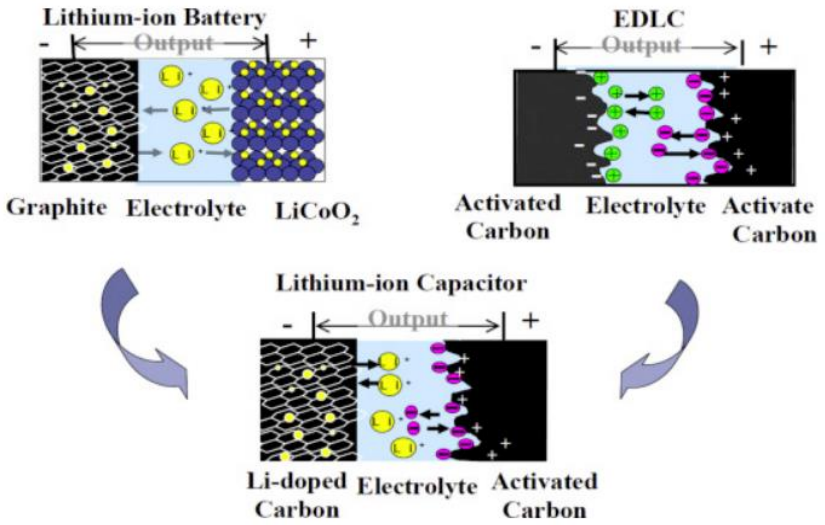

Figure 2.7: Energy storage process of three different types of electrochemical devices [9].

A striking difference exists in terms of the behavior of electrolyte ion species in LIBs and LIHCs during fast charge/discharge operation. In LIBs, lithium-ions migrate from the anode and intercalate into the cathode simultaneously during fast discharge. This leads to localized excess cations (Li^+) and anions (e.g PF_6^-) at the cathode and anode, respectively. However, the anion in the anode side can migrate faster. Therefore, the anion diffuses from the cathode to the anode to maintain charge balance. The reverse scenario takes place during the charge operation. This process results in electrolyte salt depletion at the cathode, and excess electrolyte salt at the anode which limits the rate performance of LIBs. In LIHCs however, a symmetric driving force exists for both cations and anions which would minimize electrolyte concertation gradients in the system. Both ionic species are introduced into the electrolyte simultaneously during fast discharge instead of getting depleted in one electrode by migrating to the other for charge balancing. This process may

explain why LIHCs exhibit better rate capability which also translates to higher power density characteristics than LIBs.

2.3 Capacitor-Type Electrode for LIHC

Typically, the capacity of capacitor-type electrode based on double layer mechanism is mainly influenced by the specific surface area (SSA) and the distribution of pores in the material. The electrical conductivity and compatibility with electrolyte also play important role. Carbonaceous materials such as AC, graphite, graphene, and CNT are currently the most widely employed capacitor-type electrode. As previously mentioned, pioneer work on LIHC utilized AC as the capacitor-type cathode [7]. AC exhibit attractive properties including, stable cycling, good electrolyte compatibility, and facile processing methods. However, it suffers from poor electrical conductivity, low specific capacity low rate capability due to limited ion transport through small-sized pores [20]. While many efforts have been directed towards overcoming these limitations, graphene-based materials are regarded as an alternative. Graphene exhibits better electronic conductivity than AC, good electrochemical stability with various electrolytes and has a high surface area (up to 2630 m^2g^{-1} theoretically). Although graphene-based materials have drawbacks related to restacking during electrochemical cycling which leads to capacity degradation, it can be composited with other materials such as CNT which may act as spacers to minimize the problem [21]. In 2012, Ruoff and coworkers made a significant contribution by demonstrating the application of activated graphene as a viable replacement for AC for LIHC giving a superior specific capacity compared to the later [22]. Many other research

groups have focused on other modified graphene materials to further enhance the performance of capacitor-type cathode for LIHCs [23].

2.4 Battery-Type Electrode for LIHC

Excellent electrochemical properties including high conductivity good cycling performance especially at a high rate are crucial for battery-type electrode in LIHCs. Early generation and commercial LIHCs are based on graphite battery-type anode because of advantages such as moderate specific capacity (372 mAg^{-1}) and conductivity, and low intercalation potential which leads to high energy density. However, there are concerns about its poor rate capability and proximity to lithium plating potential during fast charge operation. The first LIHC concept wa demonstrated with LTO. LTO exhibits negligible volume change, high lithiation potential (~1.55 V vs Li/Li^+) and high rate capability [24]. However it suffers from poor electrical conductivity(10^{-13} Scm^{-1}) [25]. Solution approach for these drawbacks includes, ion doping, introducing conducting agent such as carbonaceous materials, e.g graphene, CNT and nanostructuring to improve ions and electrons transport in the material. Nanostructuring is very advantageous in shortening the lithium-ion diffusion distance in the material leading to improved capability for fast charge /discharge. For example, Dong et al investigated self –doping of LTO nanoparticles with trivalent Ti as battery-type anode aiming enhanced lithium insertion/extraction kinetics for LIHC [26]. The results show that the Ti-doped samples delivered faster charge/discharge characteristics than the original group thus enabling high power performance of LIHC. Naoi et al anchored LTO nanoparticles on carbon nanofibers (CNF) to enable facile lithium-ion diffusion. The material showed extraordinary performance by withstanding up

to 300 C charge/discharge rate with ca.95 % capacity retention after 300 cycles [27]. These electrochemical characteristics provided high energy-power density output for LIHC using AC as capacitor-type cathode. Moreover, Zhao et al. demonstrated excellent electrochemical performance with LTO embedded in AC by simple a vacuum infiltration process (Figure 2.9) [28]. The LTO/AC composite showed great potential for use in LIHC to achieve high energy-power density output when coupled with AC counter electrode. The LIHC based on the composite shows remarkable rate performance, with gravimetric capacities up to ca. 105 mAh g^{-1} at 350C.

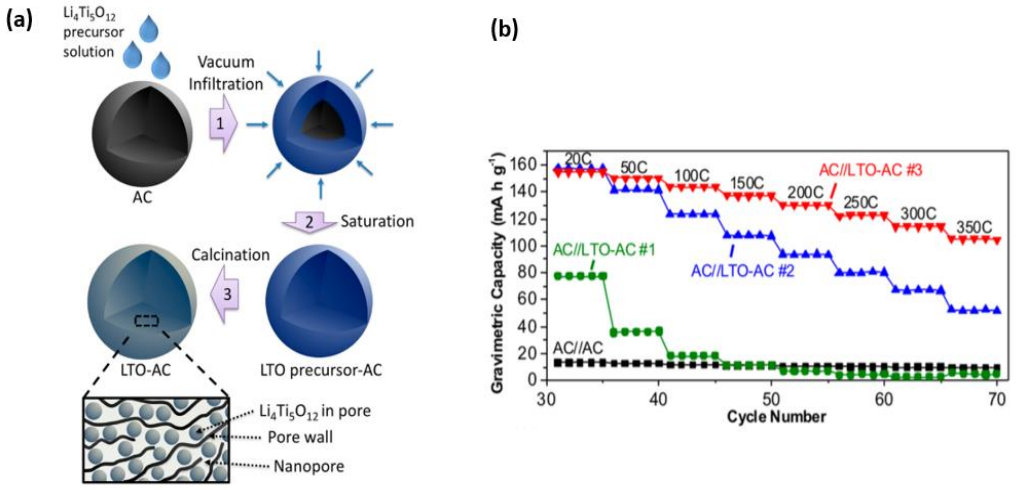

Figure 2.9: (a)Schematic illustration of the synthesis LTO embedded in AC. (b) Gravimetric performances of AC//LTO- AC LIHC compared with the AC//AC full cells [28].

Similarly, battery-type cathodes have also been studied for LIHC. For example, Yoon et al demonstrated an LIHC based on $Li[Ni_{1/3}Co_{1/3}Mn_{1/3}]O_2$ battery-type cathode

realized a specific capacity of 60 F g^{-1} [29]. Also Olivine phase $LiFePO_4$ (LFP) has also been explored as battery-type cathode for LIHC. LFP exhibits a flat discharge profile and possesses theoretical capacity of 170 $mAhg^{-1}$. The material exhibits good thermal properties and it is environmentally friendly. Ping et al evaluated a LIHC with LFP/AC composite as the battery-type cathode using mesoporous microbeads (MCMB) as the counter electrode. The electrochemical performance of the LIHC was found to be multiple times better than the system with AC cathode and reached an energy density of ca. 69 $Whkg^{-1}$with good capacity retention [30].

2.5 **Electrolytes for LIHCs**

LIHC systems are typically based on aqueous or non-aqueous electrolyte media. Aqueous electrolytes offer high ionic conductivity and are suitable for high power performance but they exhibit low break-down voltage of only about 1V (maximum). Non-aqueous electrolytes can provide higher break-down voltage than aqueous electrolytes and are advantageous in enhancing the energy density of LIHCs. Non-aqueous LIHCs typically utilize lithium-based organic liquid electrolytes like those employed in LIBs. Nowadays, polymer electrolytes (PE) are popular solid electrolytes finding application in solid-state LIBs and supercapacitors to provide great advantage in terms of safety. Among PEs, gel polymer electrolytes (GPEs) represents an advantageous electrolyte media to achieve high-performance PE [31]. They are usually prepared by immobilizing liquid electrolyte in polymer matrices such as poly (ethylene oxide), poly (vinylidene fluoride) and poly(vinylidene fluoride co-hexafluoropropylene) (PVDF-HFP), poly(ethyl

cyanoacrylate) and could deliver high ionic conductivity (>10^{-4} S cm^{-1}) [31,32]. They combine the beneficial attributes of polymer matrix such as flexibility and reduced leakage with high ionic conductivity of liquid electrolytes. GPEs also provide better electrode/electrolyte interfacial properties. Solid electrolytes hold immense potential in enabling high-performance electrochemical energy storage with improved safety but still requires more attention. To achieve high-performance LIHC with solid electrolytes, individual electrode materials, electrolyte properties as well as their interfacial interaction needs to be understood and carefully designed towards achieving high-performance characteristics.

2.6 **On-chip ECs**

Microscale on-chip ECs or Microsupercapacitors (MSCs) are small scale integrable energy storage units considered capable of replacing or complementing microbatteries in microelectronic devices [33]. Like conventional (large scale) supercapacitors, microscale ECs store charges by EDLC or pseudocapacitive mechanisms, or a combination of both to give an asymmetric system. The microscale power system is beneficial for electronic microsystems requiring fast release and uptake of high power in microelectronic devices. The ECs are also ideal for applications requiring repeated charge and discharge operations over a long period especially where periodic replacement of power units may be costly, inefficient or even impractical. They may also be coupled with microbatteries or energy harvesting microdevices to provide stable, high peak power and moderately high energy density [34]. The advantages of microscale ECs are revealed in electronic microsystems such as wireless sensors networks, implantable devices.

On-chip EC electrodes can be fabricated based on planar or 3D architectural design. Planar electrode on-chip ECs offer promising performance for various electronic microsystems. The design is simple, cost-effective and well suited for mass production. However, 3D electrode design may provide more interfacial interaction between electrode and electrolyte materials, thereby giving room for improvement of the performance of the device [35]. 3D electrode structures exhibit higher effective surface area than planar structures to help create more room for loading of the electrode materials to achieve higher capacitance values [36]. In this regard, different 3D microelectrode fabrication approaches are being explored in the development of on-chip ECs. Among them, carbon-microelectromechanical systems (C-MEMS) has gained significant attention. The technique is generally based on pyrolysis of photopatterned photoresists followed by the deposition of active materials. C-MEMS technique is a simple fabrication process of 3D carbon microelectrode structures with different complexities for microscale ECs with high reproducibility [38,39, 40]. C-MEMS structures can act as active materials as well as current colletors for other active materials for on-chip ECs. For example Beidaghi et al. showed that the incorporation of polypyrrole (PPy) electrode material with 3D C-MEMS electrode gave significant improvement in the capacitive behavior of the resulting on-chip EC [40]. The SEM image of interdigital 3D C-MEMS structures with PPy electrode material incorporation, and the schematic illustration of the on-chip EC is shown in Figure 2.10.

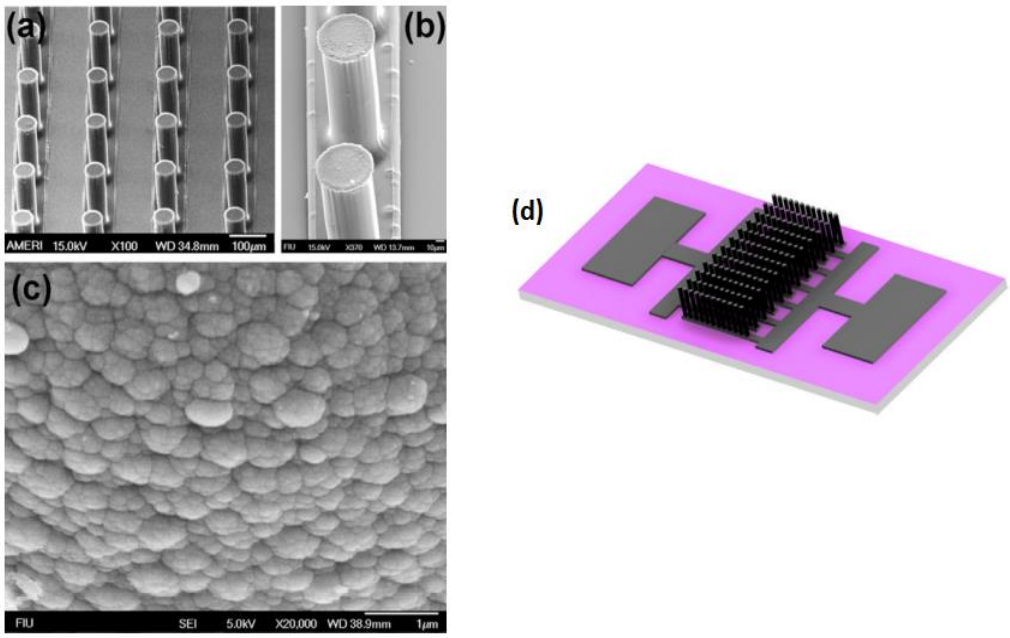

Figure 2.10: SEM images (a) C-MEMS-based 3D carbon microelectrodes, (b) the 3D carbon microelectrode with PPy and (c) the wall of the carbon structure showing PPy film (d) Schematic view of PPy/C-MEMS microsupercapacitor electrodes [40].

A summary of the performance of some microscale ECs reported in literature is presented in Table 2.1. All performance values indicated are maximum values reported. It is still very challenging to scale down the ECs and its components while ensuring suitable performance for various applications. One of the most critical goals in the development of on-chip ECs is the implementation of simple design concept to ensure high energy density to meet various application requirements.

Table 2.1: Summary of typical performance of on-chip ECs.

Fabrication Method	**Electrode Materials**	**Electrolyte**	**Capacitance**	**Energy Density**	**Power Density**	**Ref.**
Photolithography/ etching and electrophoretic deposition	*Onion-like Carbon*	*1M Et_4NBF_4 in PC*	-	*1*	*177 $mWcm^{-2}$*	[41]
CVD	*Silicon nanowires*	*EMI, TFSI in PC*	*0.9* $mFcm^{-2}$	*0.26 $mJcm^{-2}$*	*225 $mWcm^{-2}$*	[42]
C-MEMS/Electropolymerization	*PPy/Carbon*	*0.1 M KCl*	*78.35* $mFcm^{-2}$	-	*0.63 $mWcm^{-2}$*	[40]
Photolithography and etching	*Activated Carbon*	*1M NaNO3*	*90.7* $mFcm^{-2}$	-	*51.5 $mWcm^{-2}$*	[43]
Sputtering/ Photolithography/ ICP etching/FIB and electrodeposition	*RuO_2/Si-SiO_2*	*0.1M Na_2SO_4*	*99* $mFcm^{-2}$	*12 $mJcm^{-2}$*	*5 $mWcm^{-2}$*	[44]
Photolithography and Electropolymerization	*PPy/carbon*	*0.1M KCl*	*162* $mFcm^{-2}$	*25 $mJcm^{-2}$*	*1 $mJcm^{-2}$*	[40]
CVD	*Al/C/MnO2 sandwich*	*1M Na_2SO_4*	*1008.3* $mFcm^{-2}$	*35.2 mWh cm^{-2}*	-	[45]
Electrodeposition	*RuO_2/porous-Au*	*PVA/H_3PO_4*	*3473* $mFcm^{-2}$	*454 $mJcm^{-2}$*	*8 $mWcm^{-2}$*	[46]

Asymmetric systems design is a viable strategy expected to extend the performance range of microscale on-chip ECs. Asymmetric on-chip ECs are based on different electrode materials as anode and cathode exhibiting different charge storage mechanism within a restricted footprint area. The microscale asymmetric system can benefit from the different potential ranges of the dissimilar electrodes to enable enlarged device potential, thus providing improved energy density.

2.7 References

1. Shao Y, El-kady MF, Sun J, et al. Design and Mechanisms of Asymmetric Supercapacitors. *Chem Rev*. 2018;118:9233-9280. doi:10.1021/acs.chemrev.8b00252.

2. Zhang LL, Zhao XS. Carbon-based materials as supercapacitor electrodes. *chem Soc Rev*. 2009;38:2520-2531. doi:10.1039/b813846j.

3. Becker HI. Low Voltage Electrolytic Capacitor. *US Pat*. 1957;2800616.

4. Rightmire RA. Electrical Energy Storage Apparatus. *US Pat*. 1966;3288641.

5. Trasatti S, Buzzanca G. Ruthenium dioxide: a new interesting electrode material. Solid state structure and electrochemical behaviour. *Electroanal Chem INTERFACIAL Electrochem*. 1971;29:4-8.

6. Cericola D, Kötz R. Electrochimica Acta Hybridization of rechargeable batteries and electrochemical capacitors : Principles and limits. *Electrochim Acta*. 2012;72:1-17. doi:10.1016/j.electacta.2012.03.151.

7. Amatucci GG, Badway F, Pasquier A Du, Zheng T. An Asymmetric Hybrid Nonaqueous Energy Storage Cell. *J Electrochem Soc*. 2001;148(8):A930-A939. doi:10.1149/1.1383553.

8. Aravindan V, Gnanaraj J, Lee Y, Madhavi S. Insertion-Type Electrodes for Nonaqueous Li-Ion Capacitors. *Chem Rev*. 2014;114:11619-11635. doi:10.1021/cr5000915.

9. Li B, Zheng J, Zhang H, et al. Electrode Materials , Electrolytes , and Challenges in Nonaqueous Lithium-Ion Capacitors. *Adv Mater*. 2018;30:1-19. doi:10.1002/adma.201705670.

10. Salanne M, Rotenberg B, Naoi K, et al. Efficient storage mechanisms for building better supercapacitors. *Nat energy*. 2016;1. doi:10.1038/NENERGY.2016.70.

11. Merlet C, Rotenberg B, Madden PA, et al. On the molecular origin of supercapacitance in nanoporous carbon electrodes. *Nat Mater*. 2012;11. doi:10.1038/nmat3260.

12. Conway BE. Electrochemical Supercapacitors: Scientific Fundamentals and Technological AppLIHCations. 1997.

13. Augustyn V, Dunn B. Pseudocapacitive oxide materials for high-rate electrochemical energy storage. *Energy Environ Sci*. 2014;7:1597-1614. doi:10.1039/c3ee44164d.

14. Wang Y, Song Y, Xia Y. Electrochemical capacitors: mechanism, materials, characterization and appLIHCations chemical functional materials. *chem Soc Rev*. 2016;45:5925-5950. doi:10.1039/c5cs00580a.

15. Choi N, Chen Z, Freunberger SA, et al. Challenges Facing Lithium Batteries and Electrical Double-Layer Capacitors Angewandte. *Angew Chem Int Ed*. 2012;51:9994-10024. doi:10.1002/anie.201201429.

16. Etacheri V, Marom R, Elazari R, Salitra G, Aurbach D. Environmental Science Challenges in the development of advanced Li-ion batteries : a review. *Energy Environ Sci*. 2011;4:3243-3262. doi:10.1039/c1ee01598b.

17. Verma P, Maire P, Novák P. Electrochimica Acta Review article A review of the features and analyses of the solid electrolyte interphase in Li-ion batteries. *Electrochim Acta*. 2010;55(22):6332-6341. doi:10.1016/j.electacta.2010.05.072.

18. Manthiram A. An Outlook on Lithium Ion Battery Technology. *ACS Cent Sci*. 2017;3:1063-1069. doi:10.1021/acscentsci.7b00288.

19. Goodenough JB, Kim Y. Challenges for Rechargeable Li Batteries. *Chem Mater*. 2010;22:587-603. doi:10.1021/cm901452z.

20. Xie K, Qin X, Wang X, Wang Y, Tao H, Wu Q. Carbon Nanocages as Supercapacitor Electrode Materials. *Adv Mater*. 2012;24:347-352. doi:10.1002/adma.201103872.

21. Cheng Q, Tang J, Ma J, Zhang H. Graphene and carbon nanotube composite electrodes for supercapacitors with ultra-high energy density. *Phys Chem Chem Phys*. 2011;13:17615-17624. doi:10.1039/c1cp21910c.

22. Stoller MD, Murali S, Quarles N, et al. Activated graphene as a cathode material for Li-ion hybrid supercapacitors. *Phys Chem Chem Phys*. 2012;14:3388-3391. doi:10.1039/c2cp00017b.

23. Shan X, Wang Y, Wang D, Li F, Cheng H. Armoring Graphene Cathodes for High-Rate and Long-Life Lithium Ion Supercapacitors. *Adv Energy Mater*. 2016;6:1502064. doi:10.1002/aenm.201502064.

24. Yue J, Badaczewski FM, Voepel P, et al. Critical Role of the Crystallite Size in Nanostructured Li4Ti5O12Anodes for Lithium-Ion Batteries. *ACS Appl Mater Interfaces*. 2018;10(26):22580-22590. doi:10.1021/acsami.8b05057.

25. Coelho J, Pokle A, Park SH, et al. Lithium Titanate/Carbon Nanotubes Composites Processed by Ultrasound Irradiation as Anodes for Lithium Ion Batteries. *Sci Rep*. 2017;7(1):1-11. doi:10.1038/s41598-017-06908-3.

26. Dong S, Wang X, Shen L, et al. Trivalent Ti self-doped Li 4 Ti 5 O 12 : A high-performance anode material for lithium-ion capacitors. *JEAC*. 2015;757:1-7. doi:10.1016/j.jelechem.2015.09.002.

27. Naoi K, Ishimoto S, Isobe Y, Aoyagi S. High-rate nano-crystalline Li 4 Ti 5 O 12 attached on carbon nano-fibers for hybrid supercapacitors. *J Power Sources*. 2010;195(18):6250-6254. doi:10.1016/j.jpowsour.2009.12.104.

28. Zhao E, Qin C, Jung H, et al. Lithium Titanate Con fi ned in Carbon Nanopores for Asymmetric Supercapacitors. *ACS Nano*. 2016;10:3977-3984. doi:10.1021/acsnano.6b00479.

29. Yoon J, Bang HJ, Prakash J, Sun Y. Comparative study of Li [Ni 1 / 3 Co 1 / 3 Mn 1 / 3] O 2 cathode material synthesized via different synthetic routes for asymmetric electrochemical capacitor appLIHCations. *Mater Chem Phys*. 2008;110:222-227. doi:10.1016/j.matchemphys.2008.01.032.

30. Lina P, Jiaming Z, Zhiqiang SHI, Jie QI, Chengyang W. Electrochemical performance of MCMB /(AC + LiFePO 4) lithium-ion capacitors. *Chinese Sci Bull*. 2013;58(6):689-695. doi:10.1007/s11434-012-5456-9.

31. Cheng X, Pan J, Zhao Y, Liao M, Peng H. Gel Polymer Electrolytes for Electrochemical Energy Storage. *Adv Energy Mater*. 2018;8:1702184. doi:10.1002/aenm.201702184.

32. Marcoussis L De. Ion-conductive macromolecular gels and membranes for solid lithium cells. *J Appl Electrochem*. 1975;5:63-69.

33. Liu GB, Feng W, Xu X, et al. On-chip and freestanding elastic carbon films for micro-supercapacitors. *Science (80-).* 2016;351(6274):3717-3720. doi:10.1126/science.aad3345.

34. Xiong G, Meng C, Reifenberger RG, Irazoqui PP, Fisher TS. A review of graphene-based electrochemical microsupercapacitors. *Electroanalysis*. 2014;26(1):30-51. doi:10.1002/elan.201300238.

35. Rolison DR, Long JW, Lytle JC, et al. Multifunctional 3D nanoarchitectures for energy storage and conversion. *Chem Soc Rev*. 2009;38(1):226-252. doi:10.1039/b801151f.

36. Li S, Wang X, Xing H, Shen C. Micro supercapacitors based on a 3D structure with symmetric graphene or activated carbon electrodes. *J Micromechanics Microengineering*. 2013;23(11):114013. doi:10.1088/0960-1317/23/11/114013.

37. Sun W, Chen X. Microelectronic Engineering Fabrication and tests of a novel three dimensional micro supercapacitor. *Microelectron Eng*. 2009;86(4-6):1307-1310. doi:10.1016/j.mee.2008.12.010.

38. Wang C, Jia G, Taherabadi LH, Madou MJ. A novel method for the fabrication of high-aspect ratio C-MEMS structures. *J Microelectromechanical Syst*. 2005;14(2):348-358. doi:10.1109/JMEMS.2004.839312.

39. Song, Y., Agrawal, R., Hao, Y., Chen, C., Wang C. C-MEMS based microsupercapacitors and microsensors.

40. Beidaghi M, Wang C. Micro-supercapacitors based on three dimensional interdigital polypyrrole/C-MEMS electrodes. *Electrochim Acta*. 2011;56(25):9508-9514. doi:10.1016/j.electacta.2011.08.054.

41. Pech D, Brunet M, Durou H, et al. Ultrahigh-power micrometre-sized supercapacitors based on onion-like carbon. *Nat Nanotechnol*. 2010;5(September):651-654. doi:10.1038/nnano.2010.162.

42. Sadki S. Are tomorrow ' s micro-supercapacitors hidden in a forest of siLIHCon nanotrees ? 2014;269:740-746. doi:10.1016/j.jpowsour.2014.05.060.

43. Shen CW, Wang XH, Zhang WF, Kang FY, Du C. A novel three-dimensional micro supercapacitor using self-support nano composite materials. *Proc IEEE Int Conf Micro Electro Mech Syst*. 2011:1285-1288. doi:10.1109/MEMSYS.2011.5734668.

44. Wang X, Yin Y, Li X, You Z. Fabrication of a symmetric micro supercapacitor based on tubular ruthenium oxide on siLIHCon 3D microstructures. *J Power Sources*. 2014;252:64-72. doi:10.1016/j.jpowsour.2013.11.109.

45. He S, Zhang R, Zhang C, et al. Al/C/MnO sandwich nanowalls with highly porous surface for electrochemical energy storage. *J Power Sources*. 2015;299:408-416. doi:10.1016/j.jpowsour.2015.09.029.

46. Ferris A, Garbarino S, Guay D, Pech D. 3D RuO2 Microsupercapacitors with Remarkable Areal Energy. *Adv Mater*. 2015;27(42):6625-6629. doi:10.1002/adma.201503054.

CHAPTER 3

Methodology

3.1 Electrostatic Spray Deposition

Electrode materials with rationally designed architecture are useful to provide improved performance in electrochemical energy storage systems. Among a variety of methods that are being explored, the electrostatic spray deposition (ESD) technique is attractive [1]. The typical setup of ESD process is presented in Figure 3.1. A high voltage is applied to a precursor solution through an attached needle. Due to the applied voltage, the precursor solution gets atomized into charged droplets and deposited on a heated substrate. Thin films of various electrode materials with controllable morphology can be prepared from their precursor solutions by ESD [2-4]. The reduced graphene oxide-carbon nanotubes (rGO-CNT) electrode material in the scale-up systems of this dissertation was fabricated by ESD.

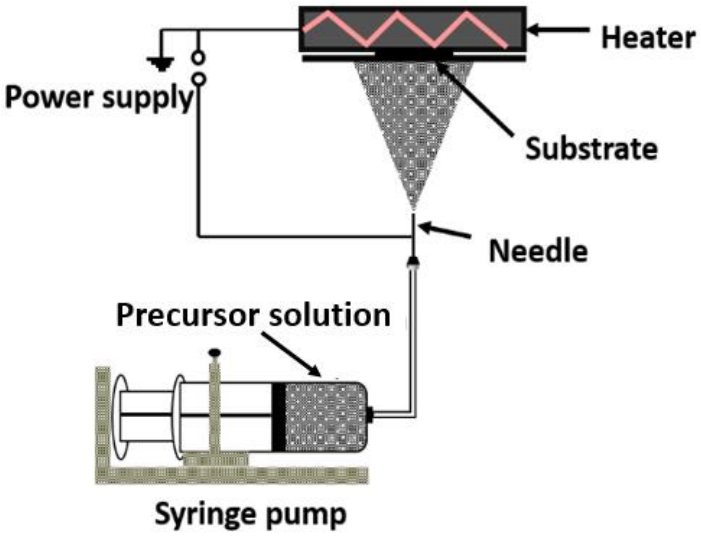

Figure 3.1: A setup of the ESD process.

3.2 Electrophoretic Deposition

Electrophoretic deposition (EPD) is a facile deposition process for various materials from their colloidal suspension. A typical setup of the EPD process is presented in Figure 3.2. An electric field is applied to electrodes immersed in a colloidal suspension of the material to be deposited. The particles of the materials become charged and migrate towards the oppositely charged electrodes where deposition occurs. EPD is an attractive method of preparing thin films of various electrode materials with high deposition rate, good thickness control and good uniformity EPD was used to selectively deposit electrode materials on the interdigital carbon microelectrodes

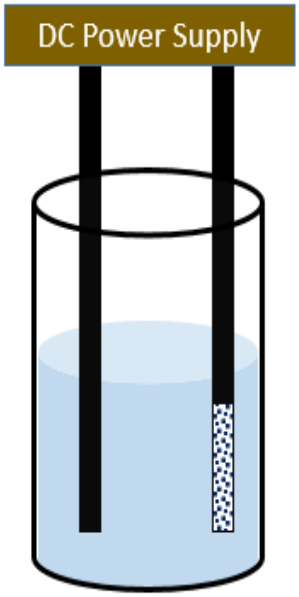

Figure 3.2: An illustration of a typical EPD Setup.

3.3 Carbon Microelectromechanical Systems

The interdigital carbon microelectrodes for on-chip devices were based on carbon microelectromechanical systems (C-MEMS) technique. C-MEMS structures are typically fabricated by the pyrolysis of patterned photoresist. C-MEMS technique is very attractive in the fabrication of a wide variety of carbon microelectrodes with a high aspect ratio for miniature electrochemical energy storage systems. Wang et al. demonstrated that C-MEMS derived carbon micropillars could act as a host for lithium-ion storage for miniature lithium-ion batteries [7]. C-MEMS structures could also play the role of a current collector for the electrode material integration [8, 9]. Figures 3.3a, 3.3b and 3.3c show SEM images of typical carbon structures derived by C-MEMS technique. C-MEMS structures provide an attractive material and microfabrication solution for miniature electrochemical energy storage systems.

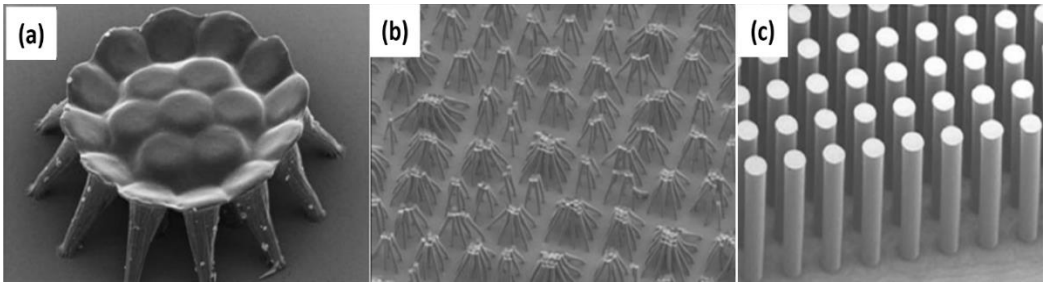

Figure 3.3: (a-c) SEM images of typical carbon structures derived by C-MEMS technique [7].

3.4 Materials Characterization

3.4.1 Scanning Electron Microscopy

Scanning electron microscopy (SEM) is a microstructural characterization tool where samples are imaged with a focused electron beam. The interaction of the electrons with the

sample generates signals containing morphological and compositional information. The resolution of SEM could be up to 10 nm. Microstructural characterizations were carried out in this dissertation using a field emission-scanning electron microscope (JOEL SEM 6330F).

3.4.2 **X-ray Diffractometry**

X-ray diffractometry (XRD) is an important analytical technique for studying the crystallinity of materials. The method involves the scattering of X-rays directed to a target material. The scattered X-rays undergo constructive and destructive interference due to the interaction with crystalline materials. The Braggs Law expressed as $n\lambda = 2dsin\theta$ gives the diffraction condition for the scattered X-rays, where, n is an integer, λ is the wavelength of the incident X-rays, d is the interplanar spacing of the crystalline material and θ is the angle of the X-ray beam. XRD studies were carried out using a Siemens D-5000 diffractometer with CuKα radiation (λ=0.154056 nm).

3.4.3 **Fourier Transform Infrared (FTIR) Spectroscopy**

Fourier transform infrared (FTIR) spectroscopy is a versatile material characterization technique based on the exposure of a test sample to infrared radiation. The infrared exposure causes the transformation of the vibrational energy levels of molecules in the sample from the ground state to excited state. The spectra generated by the techniques can be used to identify the functional groups present in a sample. A JASCO FTIR-4100 was used for FTIR studies.

3.5 **Electrochemical Characterization**

3.5.1 **Cyclic Voltammetry**

Cyclic voltammetry (CV) provides a quick information about the electrochemical behavior of electrode materials in an electrochemical system. In the technique a potential is applied as a function of time while monitoring the resulting current response. The time-dependent potential applied is known as scan rate. A current versus voltage curve is generated at an applied scan rate gives information about the charge storage process involved in an electrochemical system. Figures 3.4a and 3.4b show the typical shape of the CV curves of a capacitor-type and a battery-type electrode, respectively.

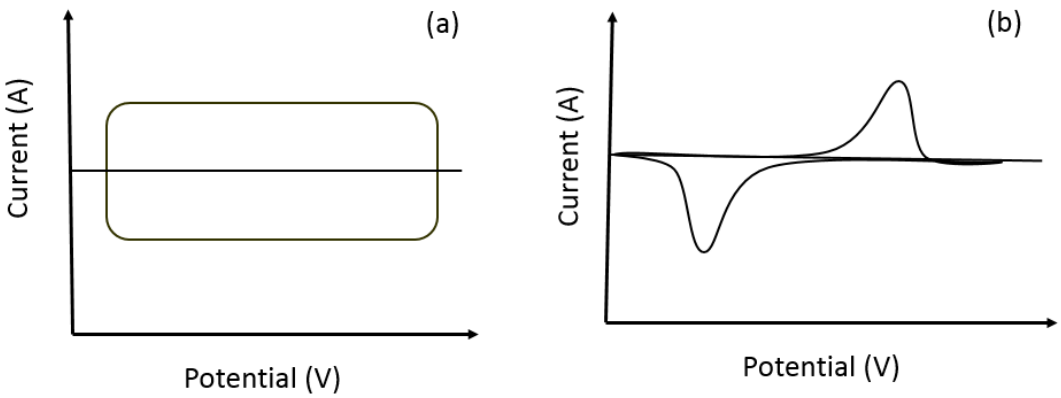

Figure 3.4: Typical CV curves of (a) capacitor-type and (a) battery-type electrodes.

The capacitor-type electrode based on non-faradaic processes typically exhibits a box-like shape with the absence of peaks(Figure 3.4a). The presence of peaks in CV curves of battery-type electrodes as illustrated in Figure 3.4b indicate faradaic charge storage mechanism. A Bio-logic versatile multichannel potentiostat (VMP3, Biologic), was used for CV tests in this dissertation.

3.5.2 **Galvanostatic Charge-Discharge**

This method is usually employed to identify potential changes, capacity, and reversibility of electrochemical processes in a device due to an applied current. Figures 3.5 shows the typical discharge curves produces by galvanostatic charge-discharge (GCD) experiments for batteries and capacitors. An ideal battery exhibits a constant voltage with the extent of discharge while ideal capacitors give a sloppy profile. [10]. GCD is very relevant for the evaluation of an electrochemical system under practical operation. GCD tests were performed by using the VMP3 potentiostat and Neware BTS-610 Battery Test System.

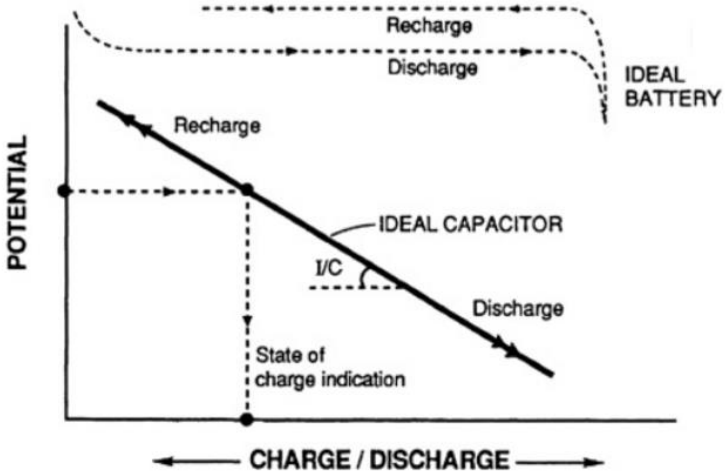

Figure 3.5: Charge/discharge realationships of capacitor and battery behavior: potential as a funtion of state of charge [10].

3.5.3 **Electrochemical Impedance Spectroscopy**

Electrochemical impedance spectroscopy (EIS) measurements are usually performed by applying a small amplitude sinusoidal potential to an electrochemical system over a range of frequencies. The overall potential response E can be related to the initial steady-state potential E_{ST} of the system by the following equation [11]:

$$E = E_{ST} + \delta E(\omega) \quad (1)$$

Where $\delta E(\omega)$ is the probe signal with $\omega = 2\pi f$

The current response to the applied potential I can be expressed as:

$$I = I_{ST} + \delta I(\omega) \quad (2)$$

$$\delta E(\omega) = |\delta E(\omega)|\, exp(j\omega t) \quad (3)$$

$$\delta I(\omega) = |\delta I(\omega)|\, exp(j\omega t + \psi) \quad (4)$$

The ratio between equations (3) and (4) corresponds to the electrochemical impedance $Z(\omega)$

$$Z(\omega) = \frac{\delta E(\omega)}{\delta I(\omega)} = Z'(\omega) + jZ''(\omega) \quad (5)$$

where ψ is the phase angle difference between the current and applied potential. EIS data are commonly represented by the Niquist plot which is a plot of the opposite imaginary part versus the real part of the impedance ($-Z''$versus Z') as shown in Figure 3.6.

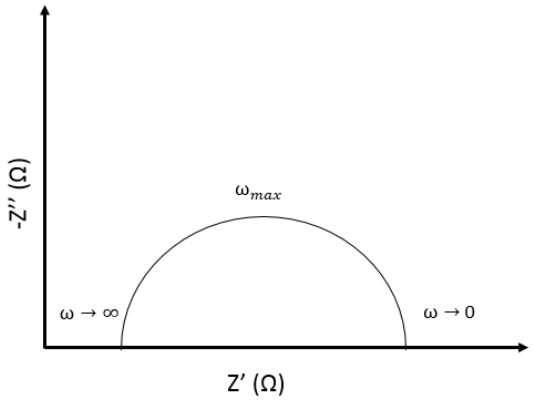

Figure 3.6: A typical Niquist plot of an electrochemical system

EIS is very useful for the estimation of the resistance and kinetics parameters of an electrochemical cell. EIS studies were carried out in this dissertation using the VMP3 potentiostat.

3.6 References

1. C. Zhu, Y. Fu, and Y. Yu, "Designed Nanoarchitectures by Electrostatic Spray Deposition for Energy Storage," *Adv. Mater.*, vol. 31, p. 1803408, 2019.

2. E. D. Adelowo, A. R. Baboukani, R. Agrawal, and C. Wang, "Electrochemical Performance of Lithium-Ion Capacitor Using Reduced Graphene Oxide – Carbon Nanotube Pre-Lithiated by Direct Contact Method," *ECS Trans.*, vol. 85, no. 13, pp. 469–474, 2018.

3. E. Adelowo, A. R. Baboukani, C. Chen, and C. Wang, "for Lithium-Ion Capacitors," *C J. Carbon Res.*, vol. 4, no. 31, 2018.

4. R. Agrawal, E. Adelowo, A. R. Baboukani, M. F. Villegas, A. Henriques, and C. Wang, "Electrostatic Spray Deposition-Based Manganese Oxide Films — From Pseudocapacitive Charge Storage Materials to Three-Dimensional Microelectrode Integrands," *Nanomaterials*, vol. 7, p. 198, 2017.

5. S. J. An *et al.*, "Thin Film Fabrication and Simultaneous Anodic Reduction of Deposited Graphene Oxide Platelets by Electrophoretic Deposition," *J. Phys. Lett.*, vol. 1, pp. 1259–1263, 2010.

6. N. A. Kyeremateng, M. Dinh, and D. Pech, "Electrophoretic deposition of Li4Ti5O12 nanoparticles with a novel additive for Li-ion microbatteries," *RSC Adv.*, vol. 5, pp. 61502–61507, 2015.

7. C. Wang, G. Jia, L. H. Taherabadi, and M. J. Madou, "A novel method for the fabrication of high-aspect ratio C-MEMS structures," *J. Microelectromechanical Syst.*, vol. 14, no. 2, pp. 348–358, 2005.

8. M. Beidaghi and C. Wang, "Electrochimica Acta Micro-supercapacitors based on three dimensional interdigital polypyrrole / C-MEMS electrodes," *Electrochim. Acta*, vol. 56, no. 25, pp. 9508–9514, 2011.

9. W. Chen *et al.*, "Integration of Carbon Nanotubes to C-MEMS for On-chip Supercapacitors," *IEEE Trans. Nanotechnol.*, vol. 9, no. 6, pp. 734–740, 2010.

10. B. E. Conway, “Electrochemical Supercapacitors: Scientific Fundamentals and Technological Applications.” Kluwer Academic/Plenum Publishers, New York, 1997.

11. F. Beguin and E. Frackowiak, “Carbons for Electrochemical Energy Storage and Conversion Systems,.” Taylor and Francis Group, Boca Raton, 2010.

CHAPTER 4

Electrostatically Sprayed Reduced Graphene Oxide-Carbon Nanotubes Electrodes for Lithium-Ion Hybrid Capacitors

4.1 Introduction

The rapid expansion of the global market for consumer electronic and electric vehicles requires high-performance energy storage units, especially with high energy density and high power density, while still retaining good cyclability [1–3]. Lithium-ion battery (LIB) and electrochemical capacitor (EC) are the most widely used energy storage technology in these electronic products, but they occupy opposite ends of performance spectrum [4,5]. Typically, LIBs exhibit high energy density due to their faradaic energy storage processes, but they deliver low power density, slow charge and discharge rate, and limited cyclability. On the other hand, ECs are based on non-faradaic electrochemical double-layer capacitance (EDLC) storage mechanism or pseudocapacitive faradaic reactions, thus enabling higher power density, fast charge, and discharge rate, as well as longer cyclability than LIBs, although they exhibit relatively lower energy density. Lithium-ion hybrid capacitor (LIHC) represents a stand-alone energy storage system that is capable of combining the positive attributes of LIB and EC to provide relatively high energy density, high power density, and good cyclability [6,7]. LIHCs are typically constructed using a LIB electrode as battery-type anode and an EC electrode as capacitor-type cathode. A capacitor-type electrode that is capable of fast charge-discharge kinetics and high surface area, high specific capacity is a key requirement for the high energy performance of LIHCs [1–3,8,9]. Moreover, the energy density of the system is usually constrained by the specific capacity of battery-type graphite electrodes. It is expected that

LIHC energy density can be improved by utilizing electrodes that are capable of offering higher specific capacity in place of traditional activated carbon and graphite.

Owing to the advantageous properties of graphene in terms of specific capacity, specific surface area (SSA), chemical stability, and electrical conductivity, many studies have demonstrated high-performance LIHC using graphene-based electrodes [3,8,10–17]. In recent years, more efforts are being made to fine-tune the material to further enhance its properties to advance the electrochemical performance of LIHCs. Some of the efforts include carrying out activation procedures to achieve improved SSA [8], doping [16], compositing with other materials [14], and functionalization [17], using various approaches**.** However, most of the graphene-based electrode fabrication approaches present challenges, such as cumbersome processes, high-temperature heating in inert atmospheres, and utilization of toxic chemicals, which raises convenience and environmental concerns.

Photoreduction of graphene oxide (GO) has been demonstrated in literature as a simple and environmentally benign approach of preparing graphene-based capacitor electrode [18–20]**.** Electrostatic spray deposition (ESD) is another interesting approach in which the graphene-based electrode may be obtained by simply spraying GO precursor solution electrostatically on a heated current collector**.** Schematic illustration and a practical image of the ESD process are presented in Figure 4.1. ESD offers a rapid and simple electrode fabrication approach [21,22]. GO precursor solution and ESD process parameters can be easily controlled in order to obtain numerous morphologies that may influence the electrochemical properties of the graphene-based electrode. It also enables the direct binder-free deposition and reduction of GO on a current collector simultaneously.

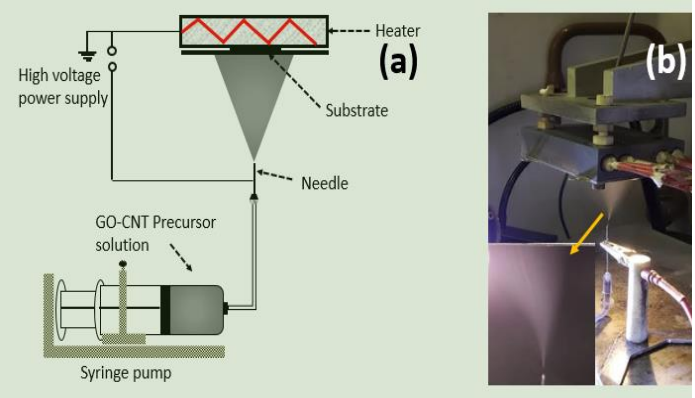

Figure 4.1: (a) Schematic illustration of electrostatic spray deposition (ESD). (b) Digital image of ESD.

Previous work from our group demonstrated promising electrochemical performance of ESD-based reduced graphene oxide-carbon nanotube (rGO-CNT) electrode for micro-supercapacitors [21]. The rGO-CNT exhibits high specific capacity, rate capability, and superior time constant, thus making it an attractive candidate for LIHC, especially as a capacitor-type cathode. Meanwhile, rGO-CNT is considered to be a promising battery-type anode [23]**.** In this work, we exploit the capability of ESD-based rGO-CNT by employing the material as both an anode and cathode for LIHC. The anode was electrochemically pre-lithiated prior to the LIHC cell assembly, while as-prepared rGO-CNT was used as cathode. The LIHC operated within a voltage range of 0.01–4.3 V, and it delivered a maximum energy density of 114.5 Wh Kg^{-1} and maximum power density of 2569 W kg^{-1}.

4.2 Experimental Section

A similar method that was previously reported in [21] was used for the electrode preparation. Briefly, the starting materials, GO powder (0.7–1.2 nm thickness and 300–800 nm dimension) and COOH-functionalized multiwalled CNT (8–15 nm diameter, 10–50 μm length and <1.5 wt. % functional group content) were obtained from Cheaptubes Inc., Cambridgeport, VT, USA. The GO powder (18 mg) was mixed with CNT (2 mg) and was dispersed in 1,2-propanediol (20 mL) by an ultrasonic probe (750 W, 20 KHz, Sonics and materials Inc., Newtown, CT, USA) to obtain a 1 mg mL^{-1} GO-CNT precursor suspension. The precursor was then drawn into a syringe with a stainless steel needle and it was connected to a syringe pump that was kept at a rate of 4 mL h^{-1}. The distance between the tip of the needle and the stainless steel substrates was kept at 4 cm. The substrates were mounted on the ESD set-up and preheated to 250 °C before the deposition process. The precursor solution was sprayed on the heated stainless steel substrates for 2 h by applying a voltage of 5–6 kV through the stainless steel needle of the syringe. The mass loading that was obtained ranged from 0.2 to 0.8 mg cm^{-2} (thickness ca. 2.5 to 5.2 μm). For comparison, pure rGO and CNT electrodes were also prepared using similar steps.

The surface functionalities of the samples were revealed by fourier transform infrared (FTIR) (JASCO FT/IR, 4100, Tokyo, Japan), while the morphology of the samples were examined with scanning electron microscope (SEM) (FE-SEM, JEOL, Peabody, MA, USA). The structural properties of the samples were also studies with X-ray diffractometer (XRD) (Siemens, Munich, Germany) with Cu Kα radiation (λ = 1.5418 Å), which were operated at a current and voltage of 35 mA and 40 kV, respectively.

The samples were assembled in CR2032 coin cells with lithium as both counter and reference electrode for the half-cell experiments. The cells were assembled in an argon filled glove box using 1 M $LiPF_6$ in EC: EMC (Sigma Aldrich, St. Louis, MO, USA) as electrolyte and polypropylene membranes as separators. The potential windows were 0.01–3.0 V and 2.0–4.0 V for the anode and the cathode, respectively. For full cell assembly, electrochemical prelithaition process was first carried out on rGO-CNT anode by cycling six times in a half-cell assembly at a current density of 0.1 Ag^{-1}. Thereafter, the pre-lithiated anode was disassembled and was coupled with fresh rGO-CNT cathode with electrolyte and separator in CR2032 coin cell. The electrochemical performance of the LIHC was evaluated within a voltage window of 0.01–4.3 V (mass ratio of cathode and anode was 4:1). Symmetric ECs were also assembled with the rGO-CNT electrodes for comparison purpose. Electrochemical evaluations were performed on the cells by using a NEWARE battery test system (BTS-610, Shenzhen, China) and a VMP3 multichannel potentiostat (VMP3, Bio Logic, Knoxville, TN, USA). The energy density E (Wh kg^{-1}) and power density P (W kg^{-1}) of the LIHC device were calculated using the following equations [8,9]:

$$E = I \int_{t_1}^{t_2} V dt \quad (1)$$

$$\mathrm{P} = E/t_2 - t_1 \quad (2)$$

where t_1 and t_2 (h) are the initial and final time of discharge with the voltage range V (V) and I (A kg^{-1}) is constant current density.

4.3 Results and Discussion

The surface properties of the rGO-CNT film in comparison with GO, rGO, and CNT were studied with FTIR. The FTIR patterns of the samples are presented in Figure 4.2a. The broad transmission peak centered around 3352 cm^{-1} in the pattern corresponding to GO is related to O–H stretching, while the peak at ca. 1726 cm^{-1} indicates the stretching of the C=O functional group in the GO structure [24]. Furthermore, the peak at ca. 1635 cm^{-1} indicates C=C stretching [25], while the peak at ca. 1361 cm^{-1}, is related O–H bending. Other peaks at ca. 1226 and 1083 cm^{-1} correspond to C–O–C and C–O groups, respectively [26]. The peaks at 3352, 1361, 1226, and 1083 cm^{-1} in the rGO and the rGO-CNT patterns appear to be mitigated, which indicates that GO was thermally reduced after the deposition. No significant peak was observed in the FTIR pattern of CNT. This may be attributed to the marginal functional group content (<1.5 wt. %) in the CNT when compared to that of GO, rGO, and rGO-CNT within the scale of comparison. However, peaks at 1729, 1618, and 1083 cm^{-1} remain in the resulting rGO and rGO-CNT film, indicating the presence of corresponding oxygen functional groups after the deposition. A comparison of surface properties of the rGO-CNT composite and its components can be further analyzed by X-ray photoelectron spectroscopy (XPS), which would be incorporated in our future work. The surface The contribution of residual oxygen functional groups in enhancing the electrochemical performance of graphene-based materials, especially when being used as a capacitive storage material has been shown in previous studies in the literature [27,28].

The XRD patterns of GO, CNT rGO, and rGO-CNT film are presented in Figure 4.2b. The XRD pattern of the starting GO shows a clear diffraction peak at 11.08°,

corresponding to an interlayer spacing of 7.98 Å based on Bragg's equation. The rGO and rGO-CNT XRD patterns show broad diffraction peaks at 24.38° and 23.75°, corresponding to interlayer spacing of 3.65 Å and 3.74 Å, respectively. A broad peak centered around is 23.68° was observed for CNT. The disappearance of 11.08° peak in rGO and rGO-CNT samples signifies the reduction of GO after the ESD process, which is in agreement with the FTIR results. Moreover, the slight shift in the peak position of rGO-CNT to lower 2θ angle with an increase in interlayer spacing when compared with rGO may be attributed to the insertion of CNT in-between rGO layers, which is also in good agreement with previous studies [23]. SEM images of the surface and cross-section of the rGO-CNT film are shown in Figures 4.2c and 4.2d, respectively. The surface SEM image shows wrinkled rGO sheets. The cross-sectional image indicates that the CNTs are entangled within the bulk of the rGO film. As noted in previous studies, the interconnection of CNT with rGO sheets can prevent or minimize restacking of the two-dimensional (2D) material during electrochemical cycling and boost its electron/ionic conductivity [21,23]. Moreover, the cross-sectional SEM image shows that the rGO-CNT film exhibits open channels, which is expected to enable enhanced electrolyte ion accessibility, which is favorable for improved electrochemical performance.

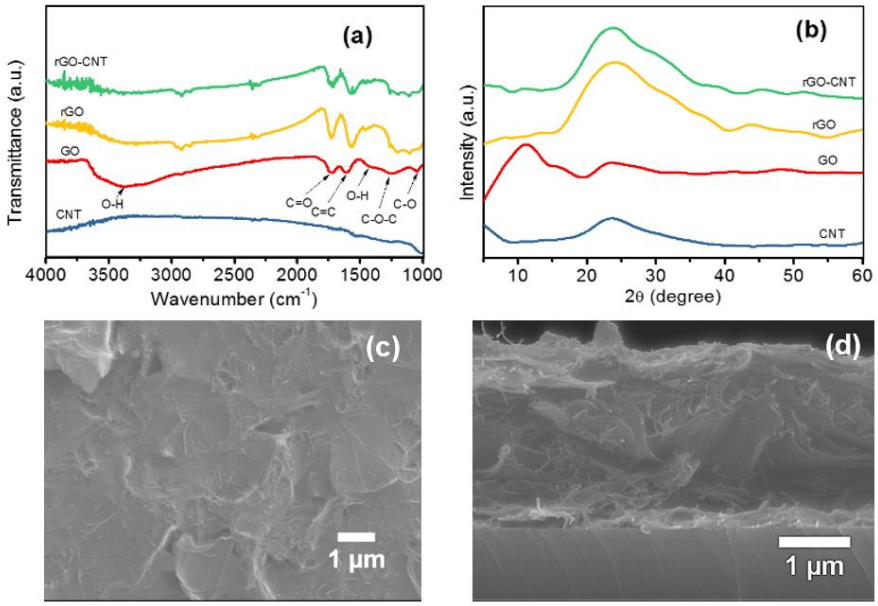

Figure 4.2: (a) FTIR pattern and (b) XRD pattern of reduced graphene oxide-carbon nanotube (rGO-CNT), rGO, GO and CNT. SEM Images of (c) surface, and (d) cross section of the rGO-CNT film.

The cyclic voltammograms (CVs) of the rGO-CNT anode half-cell is presented in Figure 4.3a, within a voltage window of 0.01–3.0 V. An irreversible reduction peaks can be observed at ca. 0.5 V in the first cycle, which may be associated with solid electrolyte interface (SEI) reaction. Thereafter, prominent anodic peaks close to 0.2 V can be observed in the CV curves from the second to the 10th cycle, indicating the reversible lithiation/delithiation reaction ($LiC_3 \leftrightarrow 3C + Li^+ + e^-$) after the first cycle due to the isolation of the anode material and the electrolyte by SEI film [29]. Figure 4.3b shows the galvanostatic charge-discharge (GCD) curves of the material at 0.1 Ag^{-1} current density with an initial discharge capacity of 1917 $mAhg^{-1}$, which also suggests SEI formation on the surface of the rGO-CNT [29,30]. Two flat plateaus can be observed on the initial discharge curve, starting at ca. 0.5 V and ca.0.2 V. Similar to CV test results, the 0.5 V

plateau may be related to SEI reaction while the 0.2 V plateau suggests lithiation potential of the material. The discharge capacity decreased to 1091 mA hg^{-1} in the second cycle, indicating 44.6% initial capacity loss. We can see that, starting from the second cycle; the discharge capacity gradually decreases but became more reversible. Moreover, the disappearance of the ca. 0.5 V plateau related to SEI reaction can be observed. The rate capability test result of the rGO-CNT shown in Figure 4.3c shows that a discharge capacity of 990 $mAhg^{-1}$ was measured at 0.1 Ag^{-1} current density after the first 30 cycles, which is significantly higher than that of rGO and CNT. The capacity rapidly decreases with increasing current density. A similar trend can be seen for both rGO and CNT, but the discharge capacity of rGO-CNT is superior in the current densities from 0.1 to 2 Ag^{-1}. The result shows that the rGO-CNT can still deliver a discharge capacity of 598 mAg^{-1} at high current density of 2 Ag^{-1}. The material also showed good reversibility and cyclability after returning the current density to 0.1 Ag^{-1}, delivering slightly higher discharge capacity of ca.1025 $mAhg^{-1}$ after 70 subsequent cycles. Electrochemical impedance spectroscopy (EIS) was carried out to gain insight into the electrochemical characteristics of the rGO-CNT electrode material. As shown in Figure 4.3d, both rGO-CNT and rGO exhibits suppressed semicircle in the high-frequency region, which corresponds to their charge transfer resistance at electrode/electrolyte interface [31,32]. An inclined line in the low-frequency region can also be observed in the EIS data that is related to lithium-ion diffusion through the electrode. In comparison with rGO, rGO-CNT shows a smaller charge transfer impedance and improved lithium-ion diffusion behavior, which supports the charge-discharge characteristic that was observed.

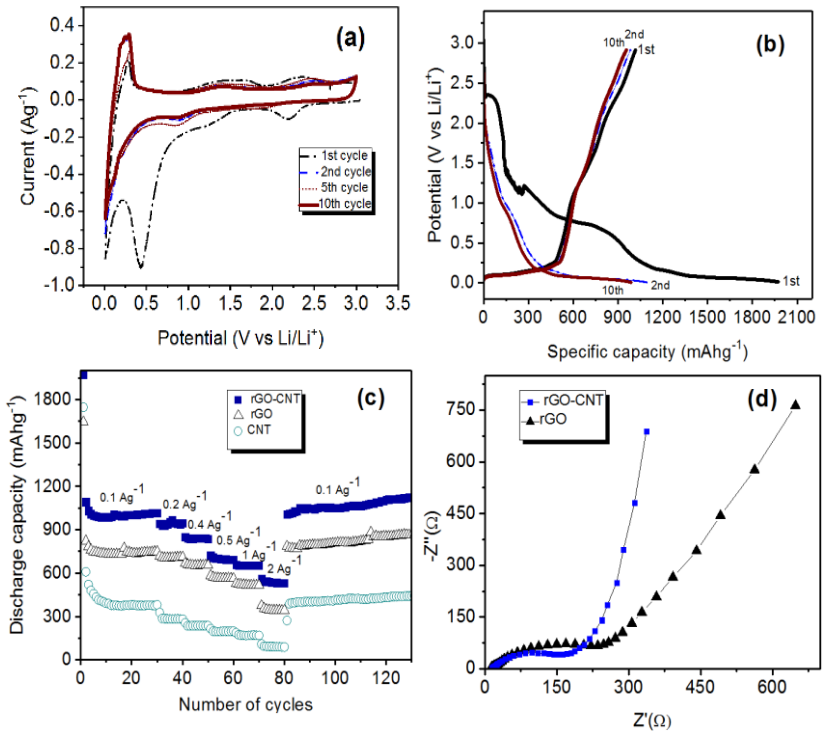

Figure 4.3: (a) CV of the rGO-CNT anode film at 0.2 mV s^{-1} scan rate. (b) GCD curves of the anode film at current density of 0.1 Ag^{-1}. (c) Cycle and rate performance at rGO-CNT, rGO, and CNT at different current densities. (d) EIS plot of rGO-CNT and rGO.

The rGO-CNT cathode material was tested in lithium half-cell configuration within a voltage window of 2.0-4.0 V. The CV curves of the rGO-CNT cathode at scan rates of 5, 10, and 20 mVs^{-1} are presented in Figure 4.4a. Rectangular shapes of typical capacitive storage mechanism can be observed on the curves, but with slight humps. The appearance of these humps suggest faradaic pseudocapacitive storage mechanism contribution besides non-faradaic EDLC mechanism due to the presence of residual oxygen functional groups in the material, which is similar to previous studies in the literature [27,28]. This observation suggests lithium-ion pseudocapacitive interaction with residual functional groups on the rGO-CNT. Charge-discharge curves of the rGO-CNT cathode material at

different current densities are presented in Figure 4.4b. A slight distortion from the typical linear shape can be seen, especially at 0.2 Ag^{-1}, indicating that both EDLC and pseudocapacitive storage mechanisms coexist. The GCD became more linear with increasing the current density. An explanation for this observation is that at low current density, both EDLC and pseudocapacitive storage mechanism, contribute to the capacity of the material. As the current density increases the EDLC storage mechanism dominates. Moreover, an iR drop can be observed on the GCD curves related to the overall resistance of the cell [21]. As shown in Figure 4.4c, after 30 cycles, the rGO-CNT cathode half-cell delivered a discharge capacity of 72 $mAhg^{-1}$ at 0.1 Ag^{-1} after 30 cycles, which exceeds the discharge capacity of 58 and 13 $mAhg^{-1}$ observed for rGO and CNT respectively. Moreover, rGO cathode half-cell showed an increasing discharge capacity until the eighth cycle, when it started decreasing. This behavior can be attributed to the effect of electrochemical activation of the rGO [21].Lithium ions insert between graphene layers and gradually increase the accessibility of ions to the surface of graphene resulting in the increasing capacity in the first eight cycles during cycling. However, the decreasing capacity after the eighth cycle suggests the decreasing accessibility of ions due to the possible restacking of the graphene layers during electrochemical cycling. In contrast, the rGO-CNT showed relatively stable performance during cycling, indicating the effectiveness of CNT, which acts as a nanospacer to prevent/minimize the restacking issue, which is in line with previous report from our group [21]. Rate capability and cyclability test (Figure 4.4c) of the half-cell shows that the rGO-CNT delivered a discharge capacity of 63.4, 60, 50.7, 46, and 41.7 $mAhg^{-1}$ at current densities of 0.2, 0.4, 0.5, 1, and 2 Ag^{-1}, respectively. The discharge capacities that were measured for the rGO-CNT are of similar

values with that of rGO at the current densities of 0.4 to 2 Ag^{-1}, but higher than that of the discharge capacities of CNT. A discharge capacity of 46.7 $mAhg^{-1}$ was observed for the rGO-CNT after 200 subsequent cycles at a current density of 1 Ag^{-1}, which significantly exceeds the CNT discharge capacity, but it only slightly exceeds that of rGO (44.9 $mAhg^{-1}$).

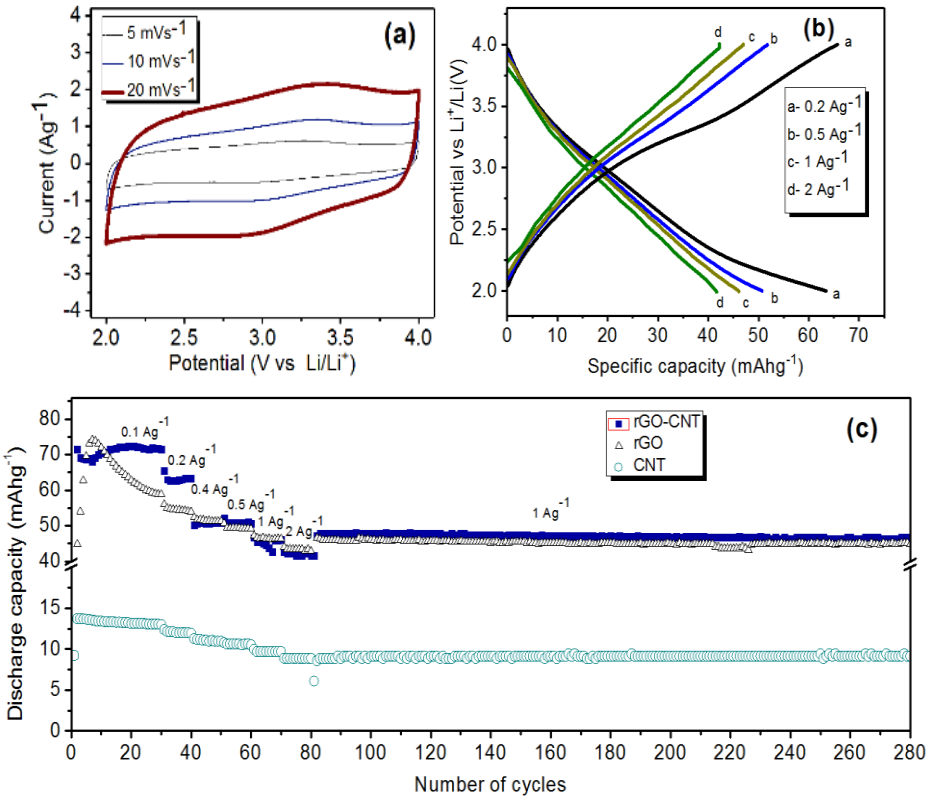

Figure 4.4: (a) CV of the rGO-CNT cathode film at different scan rates. (b) GCD curves of the cathode film. (c) Rate and cycle performance of rGO-CNT, rGO and CNT.

Symmetric ECs assembled with identical rGO-CNT electrodes were assembled and examined. Figure 4.5a shows a box-like shaped CV of the symmetric EC within a voltage range of 0 to 2.7 V at scan rates 50, 100 and 200 mVs^{-1}. The GCD profile of the symmetric

rGO-CNT//rGO-CNT device is shown is Figure 4.5b is nearly rectangular, indicating almost ideal capacitive behavior. The rate performance of the device is presented in Figure 4.5c. The symmetric device delivered discharge capacities ranging from ~8.7 to 3 $mAhg^{-1}$ it at current densities of ranging from 0.1 to 2 Ag^{-1}. The maximum energy and power density of the symmetric device presented in Figure 4.5d reached ~ 11.9 $Whkg^{-1}$ and 2670 Wkg^{-1}, respectively.

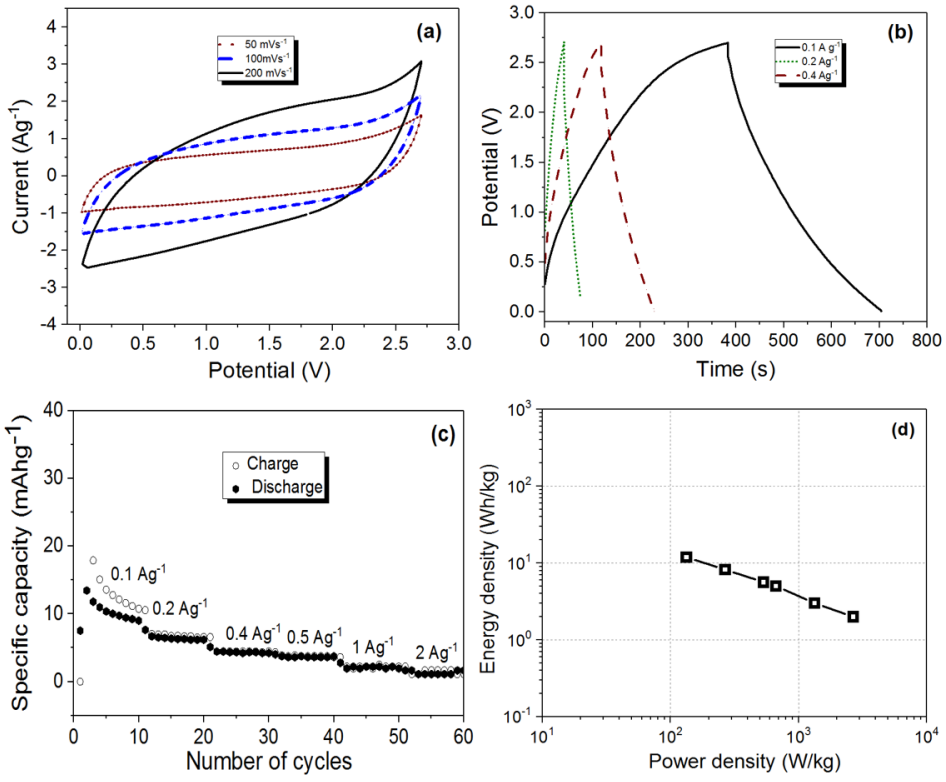

Figure 4.5: (a) CV of the rGO-CNT symmetric EC at different scan rates. (b) GCD curves of the EC. (c) Rate performance and (d) Ragone plot of the symmetric system.

To exploit the advantages of the rGO-CNT electrodes in a hybrid configuration, a LIHC was assembled by coupling the electrochemically prelithiated rGO-CNT as anode and as-prepared rGO-CNT as cathode. The CV curves of the LIHC at different scan rates (20, 50, and 100 $mVs^{-1)}$ are presented in Figure 4.6. The cathode and the anode mass ratio was kept at 4:1 (total mass −1.72 mg). The LIHC could reach up to a maximum voltage limit of 4.3 V. The quasi-rectangular shape of the CV curves indicates the capacitive behavior of the electrochemical system. The deviation from the rectangular shape that was observed in the curve can be attributed to the overlapping faradic and the non-faradaic energy storage mechanism in the LIHC. The GCD curves of the LIHC within the same voltage window of 0.01–4.3 V at 0.1 to 1 Ag^{-1} is presented in Figure 4.7a. We can see that the GCD curves exhibits a slightly distorted triangular shape, also indicating capacitive behavior. The rate capability test (Figure 4.7b) shows that the LIHC delivered a discharge capacity of 66.9, 48.8, 40.4, 22.5, and 15.5 $mAhg^{-1}$ at current densities of 0.1, 0.2, 0.5, 1, and 2 Ag^{-1}, respectively, which were normalized by the weight of both the anode and the cathode. Moreover, as shown in Figure 4.7c, the LIHC delivered a discharge capacity of 9.2 $mAhg^{-1}$ at a current density of 2 Ag^{-1} after 2000 cycles, indicating a 68.5% capacity retention. Our full cell performance indicates that both cathode and anode need to be charge-balanced to maximize the performance of the LIHC. It also requires the matching of ion transport kinetics between the two electrodes which exhibit dissimilar storage mechanisms (intercalation/deintercalation mechanism at anode side and EDLC mechanism at the cathode). In our system, the mass ratio between the cathode and the anode is 4:1, which is far from the idea mass matching according to the half-cell performance. Therefore, the results show that rGO-CNT LIHC system is cathode limiting, indicating that the

capacity of the full cell is mainly determined by the performance of the cathode side. In fact, the specific capacity of the LIHC just based on cathode loading is comparable to that of the cathode half-cell at low current density (<1 Ag^{-1}), while at higher current densities (>1 Ag^{-1}), the anode becomes the limiting electrode because the reaction kinetics of anode is sluggish at a higher rate. Furthermore, if the capacities of the ESD based rGO-CNT electrodes were fully matched in the LIHC system, then a remarkably higher energy and power density could be expected.

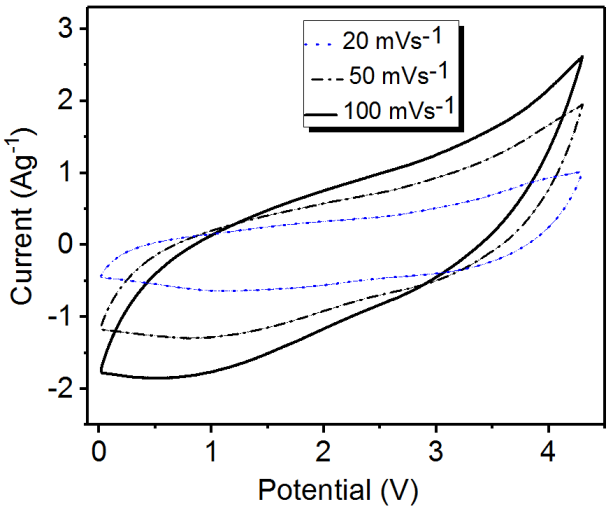

Figure 4.6: CV of the LIHC recorded between 0.01-4.3 V voltage window at different scan rates.

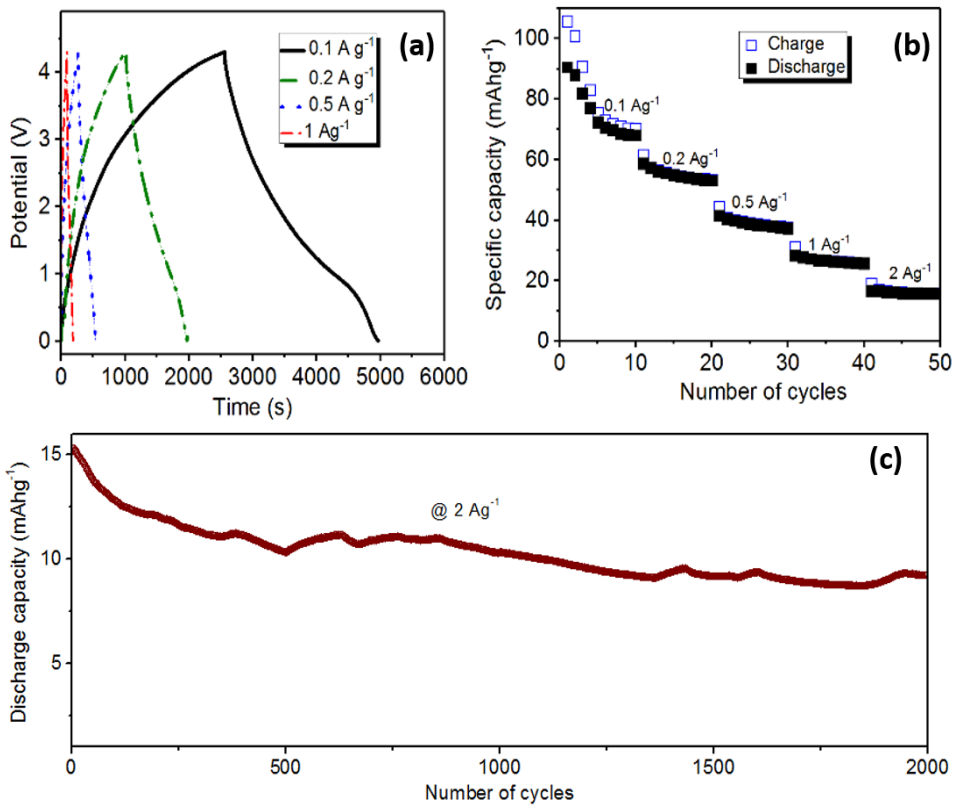

Figure 4.7: (a) GCD curves of the LIHC. (b) Rate performance of the LIHC at different current densities. (c) Cycle performance of the LIHC at a current density of 2 Ag^{-1} for 2000 cycles.

The Ragone chart of the LIHC is presented in Figure 4.8, showing energy density as high as 114.5 Wh Kg^{-1} and a maximum power density of 2569 W kg^{-1}, as calculated from the 10th cycle of discharge curves. The energy density of the LIHC is ~ 9.6 times higher than symmetric rGO-CNT//rGO-CNT EC device. The performance comparison of rGO-CNT//lithiated rGO CNT LIHC with other LIHCs reported in literature is presented in Table 3.1. The energy and power density characteristics of the LIHC are superior to Graphene//AC LIHC system [31]. The LIHC performance is comparable to graphite//functionalized graphene [17], graphitic carbon//AC [33], LIHC in terms of energy density, and Fe_3O_4/graphene//Porous three-dimensional (3D) graphene LIHC

system considering power density [11]. Its performance is however lower than flash-reduced graphene oxide//porous 3D graphene LIHC, which is a fully optimized system [12]. The electrochemical performance of our LIHC system is conceivably limited by capacity and ion transport kinetics mismatch between the two electrodes that exhibit dissimilar storage mechanisms (intercalation/deintercalation mechanism at anode side and EDLC mechanism at the cathode). If the capacities and ion transport kinetics in the ESD based rGO-CNT electrodes are fully matched in the LIHC system, then a significantly improved electrochemical performance could be expected.

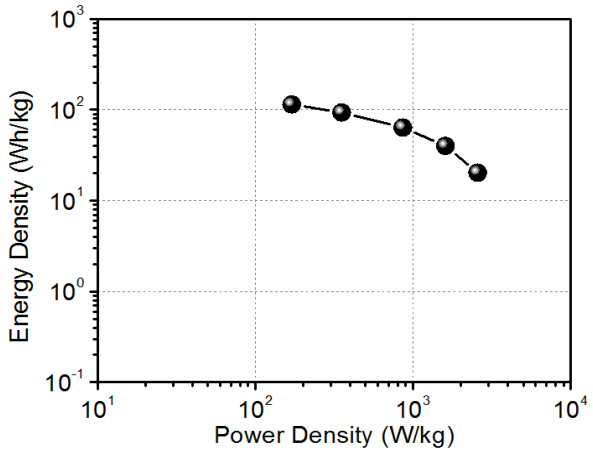

Figure 4.8: Ragone plot showing the energy and power densities of the rGO-CNT//lithiated rGO-CNT LIHC.

Table 4.1: Performance comparison with other reported LIHCs.

Anode	**Cathode**	**Voltage Window**	**Maximum Energy Density (Wh kg^{-1})**	**Maximum Power Density (W kg^{-1})**	**Ref.**
Graphene	*AC*	*2.0–4.0 V*	*61.7*	*222.2*	*[31]*
Graphite	*Funtionalized graphene*	*2.0–4.0 V*	*106*	*4200*	*[17]*
Fe_3O_4/graphene	*Porous 3D graphene*	*1.0–4.0 V*	*147*	*2587*	*[11]*
Flash-reduced graphene oxide	*Porous 3D graphene*	*0.0–4.2 V*	*148*	*10,000*	*[12]*
Graphitic carbon	*AC*	*2.0–4.0 V*	*104*	*6628*	*[33]*
Electrostatically sprayed rGO-CNT	*Electrostatically sprayed rGO-CNT*	*0.01–4.3 V*	*114.5*	*2569*	*This work*

The main mechanism in the LIHC system may involve shuttling of lithium-ions between the anode and cathode. Considering the rGO-based material as an anode, the lithium storage process includes both intercalation and surface mechanisms. Different from conventional graphite, both internal and empty pores existing between randomly oriented rGO layers are available for lithium adsorption. Additionally, the presence of defects at edges of rGO-based electrode materials as well as oxygen-containing functional groups could provide lithium storage sites. The thermal reduction of GO leading to products rich in oxygen functional groups has been well documented. Briefly, according to Acik et al., intercalated water in GO can undergo heterolysis which may result in the generation of radicals at elevated temperature [34]. More radical species are thereafter produced by the reaction of original radicals with oxygen functional groups of the GO [34]. The reaction

products after the propagation and termination of the radical species determine the quantity of oxygen functional groups in the GO material after thermal treatment [34]. The rGO-based material deposited via ESD at 250 ^{o}C contains residual oxygen functional groups. Even without activation procedures which are typically carried out on carbon cathode materials to realize high charge storage capacity for LIHCs, rGO-based material may provide high lithium storage capacity as cathode based on reversible lithiation of the oxygen functional groups. The C=O bond may interact with lithium-ions according to the following reaction: $>C = O + Li^{+} + e^{-} \leftrightarrow -C - O - Li$, to provide pseudocapacitance [35]. The amount of C=O in the rGO-based cathode material could, therefore, be very important to form redox pairs with lithium-ions for high storage capacity. During the LIHC assembly, prelithiation was carried out on the rGO-based anode to provide high amounts of lithium-ions. The ions can shuttle between the surfaces of both anode and cathode without necessarily going through sluggish bulk storage mechanism. The high surface area of the rGO-based material can, therefore, enable high capacity as well as rapid reversible lithium storage characteristics. This may explain why this LIHC configuration gave a good combination of high energy-power density output. The LIHC performance could be further improved by balancing the total charge contributions from both rGO-CNT anode and cathode. This work indicates a promising approach for the facile fabrication of rGO-based electrodes for high performance LIHCs.

4.4 **Conclusions**

In summary, we present the electrochemical performance of a LIHC based on electrostatically sprayed rGO-CNT film electrodes. The rGO-CNT electrodes show a specific capacity of 990 and 72 $mAhg^{-1}$ at a current density of 0.1 Ag^{-1} for anode and cathode, respectively. The LIHC constructed with the rGO-CNT film delivered a maximum energy density of 114.5 Wh kg^{-1} and a maximum power density of 2569 W kg^{-1}, thus indicating the promising potential of ESD approach for the facile fabrication of graphene-based electrodes for high-performance LIHCs.

4.5 References

1. Omar N, Daowd M, Hegazy O, et al. Electrochimica Acta Assessment of lithium-ion capacitor for using in battery electric vehicle and hybrid electric vehicle appLIHCations. *Electrochim Acta*. 2012;86:305-315. doi:10.1016/j.electacta.2012.03.026.

2. Lukatskaya MR, Dunn B, Gogotsi Y. architectures for future hybrid energy storage. *Nat Commun*. 2016;7:1-13. doi:10.1038/ncomms12647.

3. Zhang S, Li C, Zhang X, Sun X, Wang K. High-performance Lithium-Ion Hybrid Capacitors Employing Fe 3 O 4 − Graphene Composite Anode and Activated Carbon Cathode. *ACS Appl Mater Interfaces*. 2017;9(30):17136–17144. doi:10.1021/acsami.7b03452.

4. Simon P, Gogotsi Y. Materials for electrochemical capacitors. *Nature*. 2008;7:845-854. doi:10.1038/nmat2297.

5. Kaufman D, Hudson KL, Mcclamrock R. Where Do Batteries End and Supercapacitors Begin ? *Science*. 2014;343(March):1210-1212. doi:10.1126/science.1249625.

6. Amatucci GG, Badway F, Pasquier A Du, Zheng T. An Asymmetric Hybrid Nonaqueous Energy Storage Cell. *J Electrochem Soc*. 2001;148(8):A930-A939. doi:10.1149/1.1383553.

7. Wang H, Zhu C, Chao D, Yan Q, Fan HJ. Nonaqueous Hybrid Lithium-Ion and Sodium-Ion Capacitors. *Adv Mater*. 2017;29:1702093. doi:10.1002/adma.201702093.

8. Stoller MD, Murali S, Quarles N, et al. Activated graphene as a cathode material for Li-ion hybrid supercapacitors. *Phys Chem Chem Phys*. 2012;14:3388-3391. doi:10.1039/c2cp00017b.

9. Byeon A, Glushenkov AM, Anasori B, et al. Lithium-ion capacitors with 2D Nb2CTx (MXene)- carbon nanotube electrodes. *J Power Sources*. 2016;326:686-694. doi:10.1016/j.jpowsour.2016.03.066.

10. Ma Y, Chang H, Zhang M, Chen Y. Graphene-Based Materials for Lithium-Ion Hybrid Supercapacitors. *Adv Mater*. 2015;27:5296-5308. doi:10.1002/adma.201501622.

11. Zhang F, Zhang T, Yang X, et al. Environmental Science energy storage device based on graphene-enhanced electrode materials with ultrahigh energy density †. *Energy Environ Sci*. 2013;6:1623-1632. doi:10.1039/c3ee40509e.

12. Zhang T, Zhang F, Zhang L, et al. High energy density Li-ion capacitor assembled with all graphene-based electrodes. *Carbon N Y*. 2015;92:106-118. doi:10.1016/j.carbon.2015.03.032.

13. Ajuria J, Arnaiz M, Botas C, et al. Graphene-based lithium ion capacitor with high gravimetric energy and power densities. *J Power Sources*. 2017;363:422-427. doi:10.1016/j.jpowsour.2017.07.096.

14. Salvatierra RV, Zakhidov D, Sha J, et al. Graphene Carbon Nanotube Carpets Grown Using Binary Catalysts for High-Performance Lithium-Ion Capacitors. 2017. doi:10.1021/acsnano.6b07707.

15. Raccichini R, Varzi A, Passerini S, Scrosati B. The role of graphene for electrochemical energy storage. *Nat Mater*. 2015;14(March):271-279. doi:10.1038/NMAT4170.

16. Wang X, Wang Z, Zhang X, Peng H, Xin G. Nitrogen-Doped Defective Graphene Aerogel as Anode for all Graphene-Based Lithium Ion Capacitor. *ChemistrySelect*. 2017;2:8436-8445. doi:10.1002/slct.201701501.

17. Lee JH, Shin H, Ryou M, Jin K, Kim J. Functionalized Graphene for High-performance Lithium Ion Capacitors. 2012:2328-2333. doi:10.1002/cssc.201200549.

18. Gournis D, Miller RJD. Revealing the ultrafast process behind the photoreduction of graphene oxide. *Nat Commun*. 2013;4:2560. doi:10.1038/ncomms3560.

19. Zhang Y, Guo L, Xia H, Chen Q, Feng J, Sun H. Photoreduction of Graphene Oxides : Methods , Properties , and AppLIHCations. *Adv Opt Mater*. 2014;2:10-28. doi:10.1002/adom.201300317.

20. Wang S, Wu Z, Zheng S, et al. Scalable Fabrication of Photochemically Reduced Graphene-Based Monolithic Micro- Supercapacitors with Superior Energy and Power Densities. *ACS Nano*. 2017;11:4283-4291. doi:10.1021/acsnano.7b01390.

21. Beidaghi M, Wang C. Micro-Supercapacitors Based on Interdigital Electrodes of Reduced Graphene Oxide and Carbon Nanotube Composites with Ultrahigh Power Handling Performance. *Adv Funct Mater*. 2012;22:4501-4510. doi:10.1002/adfm.201201292.

22. Agrawal R, Adelowo E, Baboukani AR, Villegas MF, Henriques A, Wang C. Electrostatic Spray Deposition-Based Manganese Oxide Films — From Pseudocapacitive Charge Storage Materials to Three-Dimensional Microelectrode Integrands. *Nanomaterials*. 2017;7(198). doi:10.3390/nano7080198.

23. Yoo E, Kim J, Hosono E, Zhou H, Kudo T, Honma I. Large Reversible Li Storage of Graphene Nanosheet Families for Use in Rechargeable Lithium Ion Batteries 2008. *Nano Lett*. 2008;8(8):2277-2282. doi:10.1021/nl800957b.

24. Mohanta HPD. Hydrazine reduced exfoliated graphene / graphene oxide layers and magnetoconductance measurements of Ge-supported graphene layers. *Appl Phys A*. 2011;103:395-402. doi:10.1007/s00339-011-6351-y.

25. Lai L, Yang H, Wang L, et al. Preparation of Supercapacitor Electrodes through Selection of Graphene Surface Functionalities. *ACS Nano*. 2012;6(7):5941-5951. doi:10.1021/nn3008096.

26. Joon Y, Joon J, Il Y, et al. Electrochimica Acta Oxygen functional groups and electrochemical capacitive behavior of incompletely reduced graphene oxides as a thin-film electrode of supercapacitor. *Electrochim Acta*. 2014;116:118-128. doi:10.1016/j.electacta.2013.11.040.

27. Chen Y, Ma Y. High-performance supercapacitors based on reduced graphene oxide in aqueous and ionic liquid electrolytes. *Carbon N Y*. 2010;49(2):573-580. doi:10.1016/j.carbon.2010.09.060.

28. Huang H, Huang C, Hsieh C, Kuo P, Ting J, Teng H. Photocatalytically Reduced Graphite Oxide Electrode for Electrochemical Capacitors. 2011;3:20689-20695. doi:10.1021/jp205133g

29. Li X, Geng D, Zhang Y, Meng X, Li R, Sun X. Electrochemistry Communications Superior cycle stability of nitrogen-doped graphene nanosheets as anodes for lithium ion batteries. *Electrochem commun*. 2011;13(8):822-825. doi:10.1016/j.elecom.2011.05.012.

30. Hu Y, Li X, Wang J, Li R, Sun X. Free-standing graphene e carbon nanotube hybrid papers used as current collector and binder free anodes for lithium ion batteries. *J Power Sources*. 2013;237:41-46. doi:10.1016/j.jpowsour.2013.02.065.

31. Ren JJ, Su LW, Qin X, et al. Pre-lithiated graphene nanosheets as negative electrode materials for Li-ion capacitors with high power and energy density. *J Power Sources*. 2014;264:108-113. doi:10.1016/j.jpowsour.2014.04.076.

32. Safa M, Hao Y, Chamaani A, et al. Electrochimica Acta Capacity Fading Mechanism in Lithium-Sulfur Battery using Poly (ionic liquid) Gel Electrolyte. *Electrochim Acta*. 2017;258:1284-1292. doi:10.1016/j.electacta.2017.11.185.

33. Li X, Wang Z, Wang J, et al. Graphitic carbon balanced between high plateau capacity and high rate capability for lithium ion capacitor. *J Mater Chem A*. 2017. doi:10.1039/C7TA03862C.

34. M. Acik *et al.*, "The Role of Oxygen during Thermal Reduction of Graphene Oxide Studied by Infrared Absorption Spectroscopy," *The*, vol. 115, pp. 19761–19781, 2011.

35. D. Wang, C. Sun, G. Zhou, F. Li, and L. Wen, "lithium storage as a novel cathode material," *J. Mater. Chem. A*, vol. 1, pp. 3607–3612, 2013.

CHAPTER 5

Anode Prelithiation by Direct Contact with Lithium for Lithium-Ion Hybrid Capacitors Based on rGO-CNT Electrodes

5.1 Introduction

The development of electrochemical energy storage devices capable of providing high energy-power output and long cycle life are required for next-generation electronic products. Carbon materials in various forms are one of the most widely used and examined electrode material in electrochemical energy storage system [1]. Specifically, graphene-based two-dimensional (2D) carbon materials are of great interest for LIHCs due to numerous attractive properties such as high theoretical surface area, high specific capacity, excellent mechanical properties and good electrical conductivity [2]. LIHCs are typically based on coupling LIB anode material and EC cathode materials with a lithium salt containing organic electrolyte to provide relatively higher energy density than electrochemical capacitors, and relatively higher power density and longer cyclability than LIBs. As discussed in chapter 4, a promising electrochemical performance has been achieved in LIHCs based on reduced graphene oxide carbon nanotube (rGO-CNT) electrodes prepared by electrostatic spray deposition (ESD).

Generally, anode prelithiation plays a key role in realizing high electrochemical performance in LIHCs, especially with carbon-based materials. During the prelithiation process, lithium-ions are discharged from a source, for example, auxiliary lithium compound, electrolyte or metallic lithium, and reduced at the surface of the anode. Various anode prelithiation methods including direct contact or electrical shorting with

lithium metal [3], electrochemical prelithiation [4], and insitu prelithiation [5] have been proposed in previous literature reports. Among them, direct contact method appears to be promising from the standpoint of efficacy, simplicity and rapidity. The direct contact prelithiation method is typically carried out by simply placing metallic lithium in direct contact with the anode with few drops of electrolyte in between and kept for a certain period of time. Thereafter, the lithium is removed and the treated anode is used for LIHC assembly. In this work, we evaluate the electrochemical performance of LIHC with ESD-based rGO-CNT anode prelithiated by direct lithium contact method. As-prepared rGO-CNT was used as a cathode. Results obtained show that the LIHC reached maximum energy and power densities of 170 $WhKg^{-1}$ and 1385 WKg^{-1}, respectively.

5.2 Experimental Section

The same preparation and characterization procedures adopted for rGO-CNT electrodes for LIHCs in chapter 4 were employed. For LIHC cell assembly, prelithiation process was first carried out on rGO-CNT anode by direct physical contact of lithium metal with few drops of electrolyte and kept for 4 h as schematically illustrated in Figure 5.1a. Thereafter, the lithiated anode was coupled with fresh rGO-CNT cathode with electrolyte and separator in CR2032 coin cell as illustrated in Figure 5.1b. The electrochemical performance of the LIHC was evaluated within a voltage window of 0.01-4 V (mass ratio of cathode and anode was 4:1). Galvanostatic charge-discharge (GCD) tests were carried out on the LIHC using a Neware battery test system (BTS-610 Shenzhen, China) while cyclic voltammetry (CV) data were recorded with a VMP3 potentiostat (VMP3, Bio Logic,

USA). The energy density E (Wh kg^{-1}) and power density P (W kg^{-1}) of the LIHC were evaluated using equations:

$$E = \int_{t_1}^{t_2} IVdt \quad (1)$$

$$P = E/t_2\text{-}t_1 \quad (2)$$

where t_1, t_2 (h), V (V) and I (A kg-1) correspond to the initial and final discharge time, voltage range and current density applied respectively.

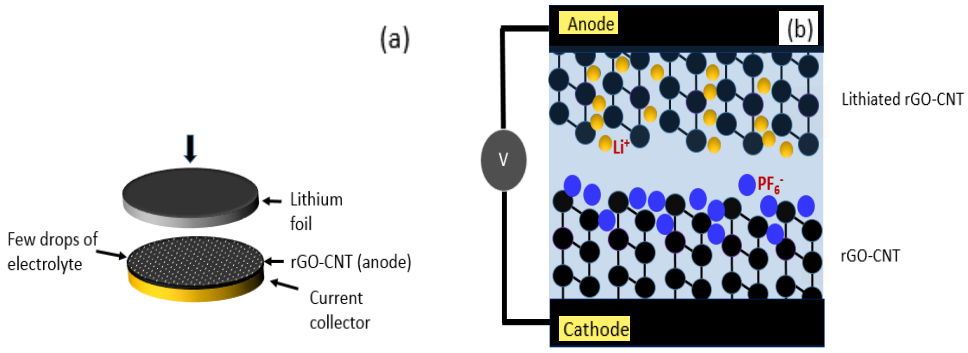

Figure 5.1. Schematic illustration of the (a) anode prelithiation process and (b) LIHC with rGO-CNT electrodes.

5.3 Results and Discussion

Figure 5.2a shows the CV curves at the voltage window of 0.01-4 V for the rGO-CNT//lithiated rGO-CNT at a scan rate of 10, 20 and 50 mVs^{-1}, respectively. The capacitive behavior of the electrochemical system is evident in the quasi-rectangular shape of the CV curves. The deviation from typical rectangular shape of capacitive behavior in the CV curves suggests energy storage mechanism based on both faradic and non-faradaic processes in the LIHC. Similarly, the shape of the GCD curves at current densities of 0.1,

0.2, 0.4, 0.5, 1, and 2 Ag^{-1} presented in Figure 5.2b exhibits a slightly distorted triangular shape indicating a deviation from ideal capacitive energy storage systems. This observation also suggests overlapping faradic and non-faradaic energy storage mechanisms in the LIHC. The rate capability test of the LIHC is presented in Figure 5.2c. A discharge capacity of 94.5 , 66.9 , 48.8 , 40.4 , 22.5 , and 10 $mAhg^{-1}$ at current densities of 0.1, 0.2 , 0.4 , 0.5 , 1 , and 2 Ag^{-1}, respectively, based on the weight of total weight of active anode and cathode. The Ragone chart of the LIHC is presented in Figure 5.2d showing energy density as high as 170 $WhKg^{-1}$ and maximum power density of 1385 Wkg^{-1}. Moreover, as shown in Figure 5.2e, the LIHC delivered a discharge capacity of 31 $mAhg^{-1}$ at a current density of 0.5 Ag^{-1} indicating 76.7 % capacity retention after 2000 cycles. The electrochemical performance of the LIHC in this study is comparable to some graphene-based LIHCs in which anode prelithiation was carried out by electrochemical process, especially in terms of energy density. For example, Zhang et al. reported a maximum energy density of 148 $Whkg^{-1}$ with flash-reduced graphene oxide anode and porous 3D graphene cathode [6]. Moreover, Salvatierra et al. reported a maximum energy density of 120 $Whkg^{-1}$ for LIHC with graphene-CNT electrodes prepared by chemical vapor deposition [7]. Ajuria et al. also reported a LIHC with a maximum energy density of 186 $Whkg^{-1}$ using SnO_2-rGO anode and thermally expanded and physically activated reduced graphene oxide cathode [4].

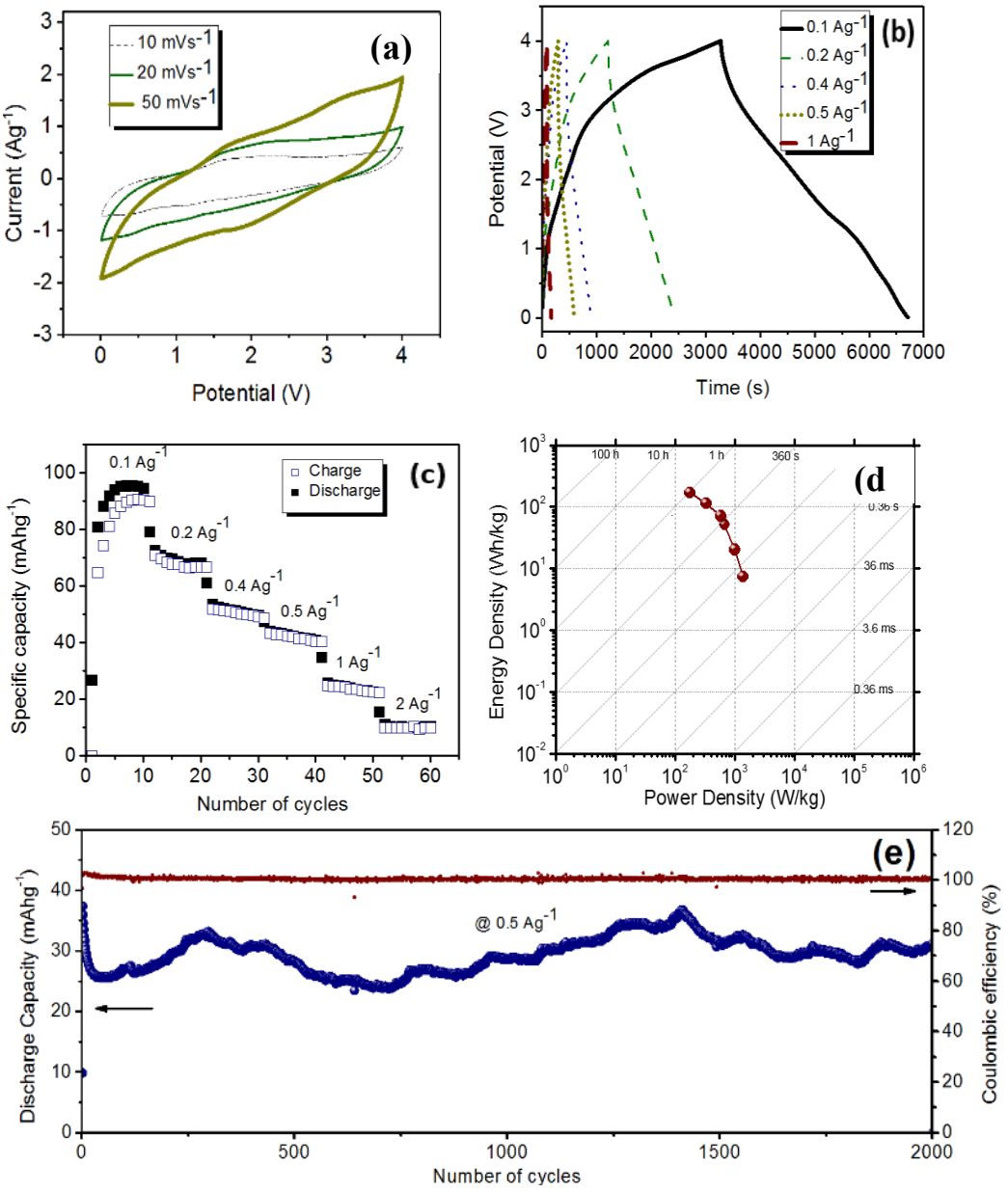

Figure 5.2 (a) CV curves of the LIHC recorded between 0.01-4 V at different scan rates. (b) GCD curves of the LIHC. (c) Rate performance of the LIHC at different current densities. (d) Ragone plot showing the energy and power densities of the LIHC (e) Cycle performance of the LIHC at a current density of 0.5 Ag^{-1} for 2000 cycles.

Generally, the exceptionally high specific surface area (SSA) of rGO leads to a very high irreversible capacity after the first discharge cycle due to SEI formation [8-11]. Although the irreversibility may gradually improve after subsequent cycles, the reversible capacity in the material occurs mostly at higher potential which may result in poor energy efficiency. The implementation of anode prelithiation in the rGO-based LIHC provides extra lithium sources to compensate for the initial lithium loss in the first discharge cycle. The anode prelithiation step may also enable higher potential window of operation in the LIHC, low cell resistance and increased cell capacity thereby giving improved energy density. We can see that the rGO-based EC system without anode prelithiation showed an energy density of ~11.9 $Whkg^{-1}$ within a voltage range of 0-2.7 V. Our prelithiated rGO-based LIHC gave an energy density ~14.3 times higher than the symmetric rGO-based EC system within a higher voltage range of 0.01-4 V. The choice of prelithiation will play a key factor in the large scale commercial manufacturing of the rGO-based LIHC in terms of time and cost. The low standard redox potential of lithium (-3.04 V vs SHE) [12] provides an easy prelithiation method based on direct lithium metal contact which may be attractive for commercial manufacturing of the rGO-based LIHC. The lithium metal foil employed for the direct contact prelithiation can be reused and the LIHC may be assembled in a single straightforward step without the need for a time consuming precycling process to rich optimal performance. However, excessive prelithiation may lead to safety hazards in the LIHC due to lithium metal plating [12-14]. Inadequate prelithiation may also limit the energy and power density output of the LIHC system. Therefore, the challenging aspect of this direct lithium contact approach is related to controlling the prelithiation degree to realize the optimum electrochemical performance. A good control of the prelithiation

degree should be the focus of future effort if this prelithiation method is to be adopted in practical LIHC assembly process.

5.4 **Conclusion**

A LIHC using ESD-based rGO-CNT anode prelithiated by direct contact method and as-prepared rGO-CNT as the cathode was described. The LIHC showed promising electrochemical performance with a specific capacity up to 94.5 $mAhg^{-1}$ at 0.1A g^{-1}. The LIHC delivered a maximum energy density of 170 $Whkg^{-1}$ and a maximum power density of 1385 Wkg^{-1}. A capacity retention of 76.7 % was also obtained after 2000 cycles. The ESD-based rGO-CNT appeared to be a promising anode and cathode material for LIHC. We envisage that the electrochemical performance characteristics of the LIHC could be further enhanced by balancing the LIHC system and optimizing the direct lithium contact anode prelithiation process.

5.5 References

1. Yoo E, Kim J, Hosono E, Zhou H, Kudo T, Honma I. Large Reversible Li Storage of Graphene Nanosheet Families for Use in Rechargeable Lithium Ion Batteries 2008. *Nano Lett*. 2008;8(8):2277-2282. doi:10.1021/nl800957b.

2. Ma Y, Chang H, Zhang M, Chen Y. Graphene-Based Materials for Lithium-Ion Hybrid Supercapacitors. *Adv Mater*. 2015:5296-5308. doi:10.1002/adma.201501622.

3. Kim M, Xu F, Lee JH, et al. A fast and efficient pre-doping approach to high energy density lithium-ion hybrid capacitors. *J Mater Chem A*. 2014;2:10029. doi:10.1039/c4ta00678j.

4. Ajuria J, Arnaiz M, Botas C, et al. Graphene-based lithium ion capacitor with high gravimetric energy and power densities. *J Power Sources*. 2017;363:422-427. doi:10.1016/j.jpowsour.2017.07.096.

5. P. Jeżowski, K. Fic, O. Crosnier TB and FB. Lithium rhenium (VII) oxide as novel material for graphite prelithaition in high-performance Lithium- ion capacitors. *J Mater Chem A*. 2016;4:12609-12615.

6. Zhang T, Zhang F, Zhang L, et al. High energy density Li-ion capacitor assembled with all graphene-based electrodes. *Carbon N Y*. 2015;92:106-118. doi:10.1016/j.carbon.2015.03.032.

7. Salvatierra RV, Zakhidov D, Sha J, et al. Graphene Carbon Nanotube Carpets Grown Using Binary Catalysts for High-Performance Lithium-Ion Capacitors. 2017. doi:10.1021/acsnano.6b07707.

8. B. M. Winter, J. O. Besenhard, M. E. Spahr, and P. Novμk, "Insertion Electrode Materials for Rechargeable Lithium Batteries **," *Adv. Mater.*, vol. 10, no. 10, pp. 725–763, 1998.

9. Z. Wu, G. Zhou, L. Yin, and W. Ren, "Graphene / metal oxide composite electrode materials for energy storage," *Nano Energy*, vol. 1, no. 1, pp. 107–131, 2012.

10. D. A. Links, "RSC Advances Graphene sheets as anode materials for Li-ion batteries : preparation , structure , electrochemical properties and mechanism for lithium storage {," *RSC Adv.*, vol. 2, pp. 6792–6799, 2012.

11. R. Raccichini, A. Varzi, S. Passerini, and B. Scrosati, "The role of graphene for electrochemical energy storage," *Nat. Mater.*, vol. 14, no. March, pp. 271–279, 2015.

12. F. Holtstiege, P. Bärmann, R. Nölle, M. Winter, and T. Placke, "Prelithaition Strategies for Rechargeable Energy Storage Technologies : Concepts , Promises and Challenges," *Batteries*, vol. 4, pp. 1–39, 2018.

13. E. De Llave *et al.*, "Comparison between Na-Ion and Li-Ion Cells : Understanding the Critical Role of the Cathodes Stability and the Anodes Pretreatment on the Cells Behavior," *ACS Appl. Mater. Interfaces*, vol. 8, pp. 1867–1875, 2016.

14. C. Uhlmann, J. Illig, M. Ender, and R. Schuster, "In situ detection of lithium metal plating on graphite in experimental cells," *J. Power Sources*, vol. 279, pp. 428–438, 2015.

CHAPTER 6

A High-Energy Aqueous On-Chip Lithium-Ion Hybrid Capacitor Based on Interdigital 3D C-MEMS Platform

6.1 Introduction

The need for high-performance microscale energy storage units for rapidly growing microelectronic devices have continued to attract much attention [1]. Miniaturized batteries and electrochemical capacitors (ECs) are attractive candidates for on-chip energy storage [2]. According to their energy storage mechanisms, ECs are based on electric double-layer capacitance (EDLC) or pseudocapacitance [3]. While EDLC involves charge storage through non-faradic adsorption/desorption of electrolyte ions on the surface of electrode materials, pseudocapacitance mechanism involves surface or near-surface faradaic reactions of electrolyte ions with metal oxides or conductive polymer electrodes. Typically, ECs can give advantageous characteristics such as higher power density, faster charge/discharge properties, and ultralong cyclability than batteries.

However, the limited energy density of ECs represents a significant drawback [4]. Over the years, asymmetric ECs realized by the combination of EDLC and pseudocapacitive electrodes have been shown to be a promising strategy to achieve improved performance trade-off in terms of energy and power density due to enlarged cell voltage window [5-8]. Another interesting asymmetric device concept is based on the combination of the bulk and surface storage mechanisms enabled by a battery-type electrode and a capacitor-type electrode, respectively. Lithium-ion hybrid capacitor (LIHC) is one of such systems,

consisting of high energy battery-type electrode and high power capacitor-type electrode [9, 10].

The electrochemical performance reports on LIHCs are mostly based on large cells which are not well suited for on-chip integration. On-chip LIHCs could potentially be favorable for integration along with other components in microelectronic devices to provide a good combination of high energy and power densities. Li et al. reported a prototype on-chip LIHC with lithiated graphite and activated carbon (AC) as the battery-type and capacitor-type electrodes, respectively, by injecting slurries of the electrode materials in an interdigital microchannel giving promising results [11]. More facile fabrication methods are however, desirable for the practical application of the on-chip LIHCs. In terms of device architecture, the fabrication of on-chip energy storage devices are targeted at ensuring high effective microelectrode surface area within a restricted space using scalable and facile approaches. 3D microelectrode designs offers higher effective surface area and better electrolyte accessibility than planar designs, which could result in enhanced areal capacity [12-16]. One of the most interesting 3D microelectrode fabrication approaches is the carbon microelectromechanical systems (C-MEMS) technique which generally involves photolithographic patterning and pyrolyzing photoresists in an inert atmosphere to obtain glassy carbon structures [17-20]. C-MEMS process is a facile route of obtaining a wide variety of ordered 3D carbon microelectrode structures with high resolution [19-21]. Various symmetric on-chip ECs with 3D carbon microelectrodes based on C-MEMS platform have previously been demonstrated [18, 22, 23]. It has been shown that the electrochemical properties of the carbon microelectrodes could be enhanced by introducing nanofeatures, for example, electrochemical activation [18], the incorporation

of CNT, [22] or by integrating pseudocapacitive materials such as MnO_2 [17] and polypyrrole (PPy) [23].

The present study demonstrates a novel on-chip LIHC based on C-MEMS-derived interdigital 3D carbon microelectrodes. Our method involved subjecting the carbon microelectrode to oxygen plasma treatment to achieve improved capacitive properties and using it as the capacitor-type electrode. The battery-type electrode in the LIHC was realized by the integration of $LiFePO_4$ (LFP) on the 3D carbon microelectrodes by electrophoretic deposition (EPD). The carbon//LFP on-chip LIHC evaluated using 1 M Li_2SO_4 aqueous electrolyte delivered an areal energy density up to ~ 5.03 $\mu Whcm^{-2}$ which was ~ 5 times higher than symmetric carbon microelectrode EC. This study broadens the prospects of the application of C-MEMS technology beyond symmetric systems in the development of high-performance on-chip capacitive energy storage.

6.2 Experimental Section

6.2.1 Interdigital Carbon Microelectrode Fabrication and LFP Integration

An illustration of the C-MEMS-based on-chip LIHC fabrication process is presented in Figure 6.1a. First, a negative tone photoresist, SU-8 25 (MicroChem Corp.), was spin-coated on a 550 μm thick Si/Si_3N_4 (10, 000 Å) wafer at 500 rpm for 12 sec and then at 3000 rpm for 30 sec. The photoresist coated wafer was baked at 65 oC for 3 min and at 95 oC for 7 min on a hot plate. UV exposure through a photomask was then carried out using an OAI mask aligner with a dose of 300 mJcm-2. Thereafter, a post-exposure bake was performed at 65 ^oC for 1 min followed by baking at 95 ^oC for 5 min. The resulting baked photoresist was developed to reveal a 2D interdigital finger pattern using a NANO^{TM} SU-8 developer solution (MicroChem Corp.). In order to build an array of 3D structures on the

2D interdigital finger pattern, a second negative photoresist, SU-8 100 (MicroChem Corp.), was spin-coated at 500 rpm for 12 sec and then at 2000 rpm for 30 sec, followed by baking (65 ºC for 10 min, and 95 ºC for 30 min) on a hot plate. The baked photoresist was patterned using a UV exposure dose of 700 $mJcm^{-2}$. Post-exposure bake (65 ºC for 3 min and 95 ºC for 10 min) was carried out followed by the development process to reveal the patterned photoresist using the SU-8 developer. The resulting samples were pyrolyzed by using a YFT 1700 tube furnace in a continuous flow of Ar (about 2000 sccm flow rate).The samples were initially heated at 350 ºC (ramp 3 ºC/min) for 30 min and then at 900 ºC (ramp 5 ºC/min) for 1 h, followed by natural cooling to room temperature in the Ar atmosphere. The interdigital patterned glassy carbon microelectrode devices obtained after the pyrolysis step were treated with oxygen plasma using a reactive ion etch (RIE) system (RIE-1701, MARCH) for 1, 5 and 10 min. An oxygen flow rate of 60 sccm, 400 mTorr pressure and 250 watts power were used during the plasma treatment process. For LFP integration, both sides of the interdigital carbon microelectrode device were connected to the positive and negative sides of a DC power source for electrophoretic deposition (EPD) process. 18 mg commercial LFP powder comprising carbon coating purchased from MTI Corporation, 1.5 mg conductive agent (Super P Li) and 0.5 mg $MgCl_2$ as an EPD process additive [24], were dispersed in 20 ml acetone-water mixture (9:1 v/v) by ultrasonication for 4 min to obtain a suspension. The suspension obtained after ultrasonication was immediately used for EPD process by applying a constant voltage of 30 V for 5, 10 and 20 sec. The devices fabricated were then washed several times with ethanol and dried overnight at 70 ºC. A schematic 3D view of the on-chip microdevice is presented in Figure 6.1b.

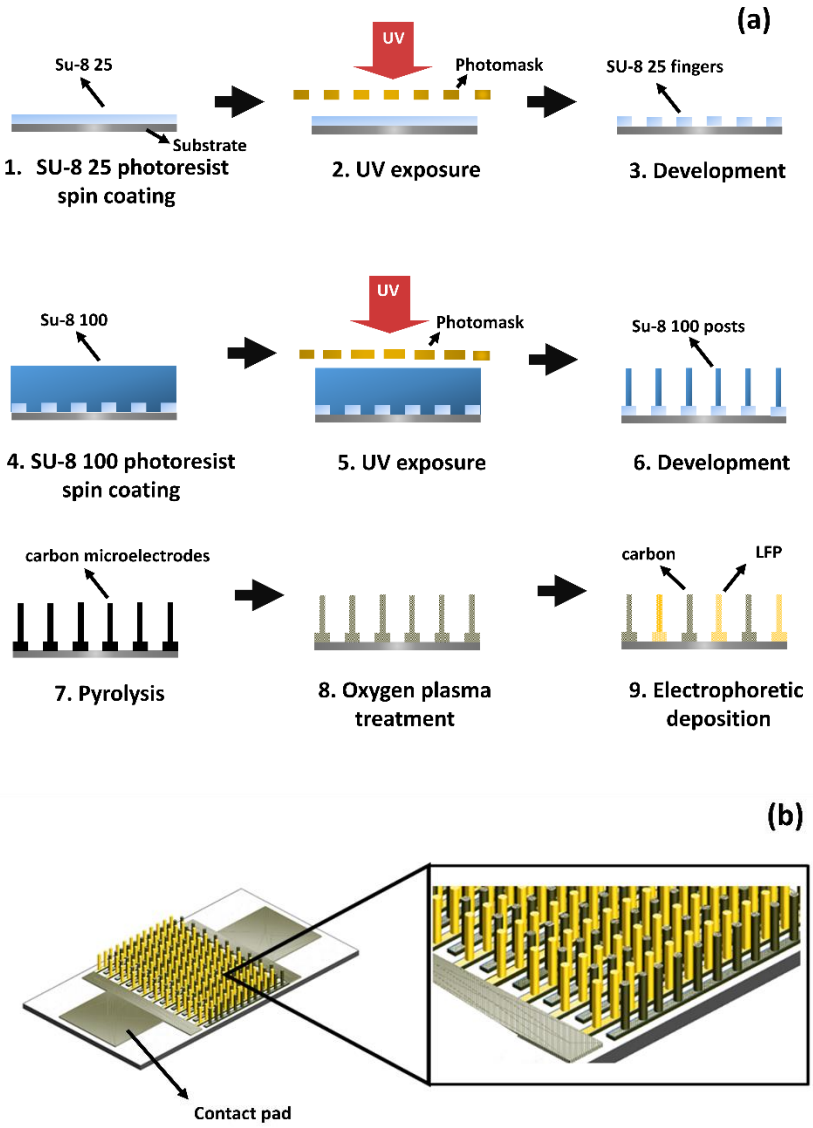

Figure 6.1: (a) Illustration of the fabrication process of the C-MEMS-based on-chip LIHC. (b) Schematic 3D view of the microdevice.

6.2.2 **Characterization**

Scanning electron microscopy (SEM) (JEOL 6330, Peabody, MA, USA) was used to reveal the surface of the carbon structures. The surface functionalities of the carbon microelectrodes were investigated by Fourier transform infrared (FTIR) (JASCO FT/IR,

4100, Tokyo, Japan). Electrochemical evaluations were carried out with 1 M Li_2SO_4 aqueous electrolyte using a VMP3 multichannel potentiostat (VMP3, Princeton Applied Research). Electrochemical impedance spectroscopy (EIS) experiments were performed with frequency ranging from 1 MHz to 100 mHz. Cyclic voltammetry (CV) and galvanostatic charge-discharge (GCD) tests were carried out in a three-electrode setup using the oxygen plasma-treated carbon anode or LFP incorporated carbon microelectrode cathode as the working electrode, while a graphite rod and Ag/AgCl served as the counter and reference electrodes, respectively. The anode was evaluated within a voltage range of - 0.9 to 0.1 V, while the cathode was tested within - 0.3 to 0.6 V. CV and GCD tests were carried out on oxygen plasma-treated carbon//carbon symmetric devices as well as carbon//LFP hybrid devices in a two-electrode setup within a voltage range of 0 to 1.4 V. The cell capacity values Q_c in the unit of $Ahcm^{-2}$ from CV curves were calculated from the following equations:

$$Q_c = C \times \Delta V / (3600 \times A) \quad (1)$$

$$C = \frac{\int I(V) dV}{2 s \Delta V} \quad (2)$$

where C is the cell capacitance in the unit of F, $\int I(V) dV$ is the integral of the CV curve over the entire test voltage range in the unit of AV, s is the scan rate in the unit of Vs^{-1}, ΔV is the width of the test voltage range in the unit of V and A is the device footprint area in the unit of cm^2. The discharge capacities Q_d in the unit of $Ahcm^{-2}$ were calculated from the discharge curves of GCD experiments using the following equation:

$$Q_d = I \times \Delta t \times / A \quad (3)$$

where I is the discharge current in the unit of A, t is the discharge time in in the unit of h and A is the total electrode geometric surface area (or the device footprint area) in the unit of cm^2.

The areal energy density E in the unit of $Whcm^{-2}$ (or $Whcm^{-3}$ for the volumetric energy density) and the areal power density P in the unit of Wcm^{-2} (or Wcm^{-3} for the volumetric power density) of the microdevices were calculated from the discharge profile of the GCD tests based on the following equations:

$$E = \Delta V \times \frac{I}{\alpha} \times t \quad (5)$$

$$P = \frac{E}{t} \quad (6)$$

$$\Delta V = (V_1 + V_2)/2 \quad (7)$$

6.3 Results and Discussion

6.3.1 Materials Characterization

The SEM image of a typical device and a single 3D carbon microelectrode obtained after the pyrolysis processes is presented in Figures 6.2a, respectively. An array of 3D carbon microelectrodes can be seen on top of planar interdigital carbon fingers. There are 20 interdigital fingers (10 for each electrode side) with length and width of about 4800 μm and 79 μm, respectively. The thickness of the fingers was about 15 μm. A typical device comprises 460 3D carbon microelectrodes (23 on each finger) with an average height of about 106 μm and diameter of about 46 μm. The total electrode geometric surface area of each side of the interdigital microelectrode (surface area of planar fingers and the projected 3D carbon structure) was ~ 0.07 cm^2. The device footprint area (planar area of the

interdigital microelectrodes and the interspaces) was ~ 0.29 cm^2. The surface morphology of the as-prepared carbon electrode sample is shown in Figure 2b. Oxygen plasma treatment resulted in roughening of the surface of the samples with the appearance of pits (Figures 6.2c, 6.2d and 6.2e) because of the etching effect on the carbon material. The pits became larger with increasing plasma treatment duration. The heights of the 3D carbon microelectrodes measured after the plasma treatment process were about 105, 104 and 96 μm for 1, 5, and 10 min treatment durations, respectively.

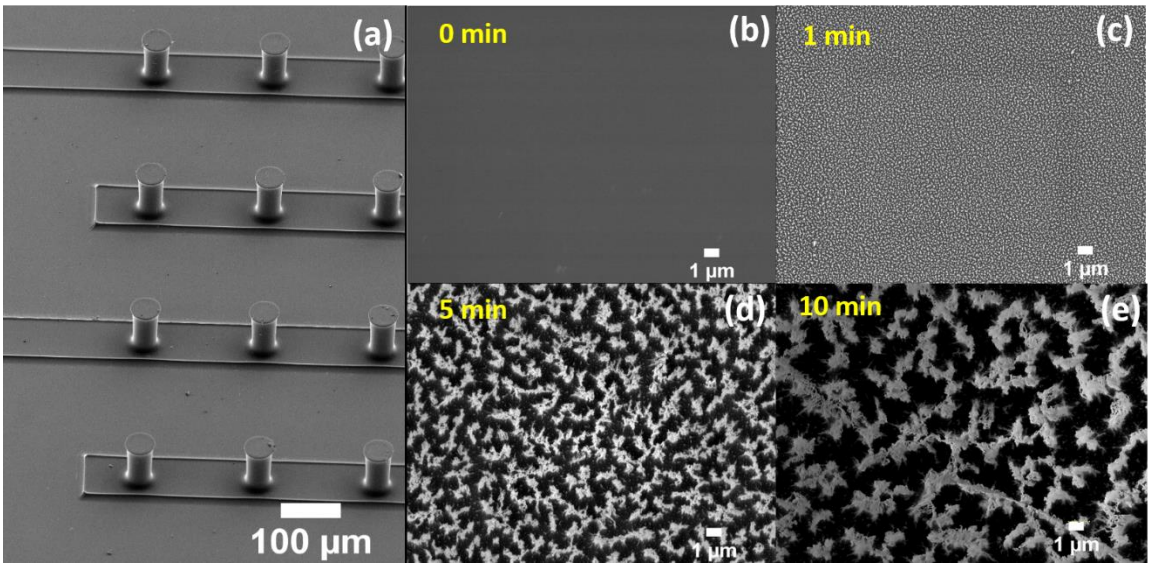

Figure 6.2. (a) SEM image of interdigital 3D carbon microelectrodes. Surface morphology of the carbon microelectrodes with (b) 0 min, (c) 1 min, (d) 5 min and (e) 10 min oxygen plasma treatment durations.

Figure 6.3a shows the on-chip LIHC with interdigital 3D microelectrodes comprising LFP electrode material and bare carbon. An enlarged view of the sample presented in Figure 6.3b shows the LFP electrode material integrated on the 3D carbon microelectrode after EPD process, while Figure 3c shows a bare 3D carbon microelectrode. Figures 6.4a, 6.4b,

6.4c and 6.4d show the microelectrodes with increasing LFP electrode deposition durations. LFP electrode thicknesses of about 0.93, 1.19 and 2.90 µm for 5, 10, and 20 sec deposition durations, were measured, respectively.

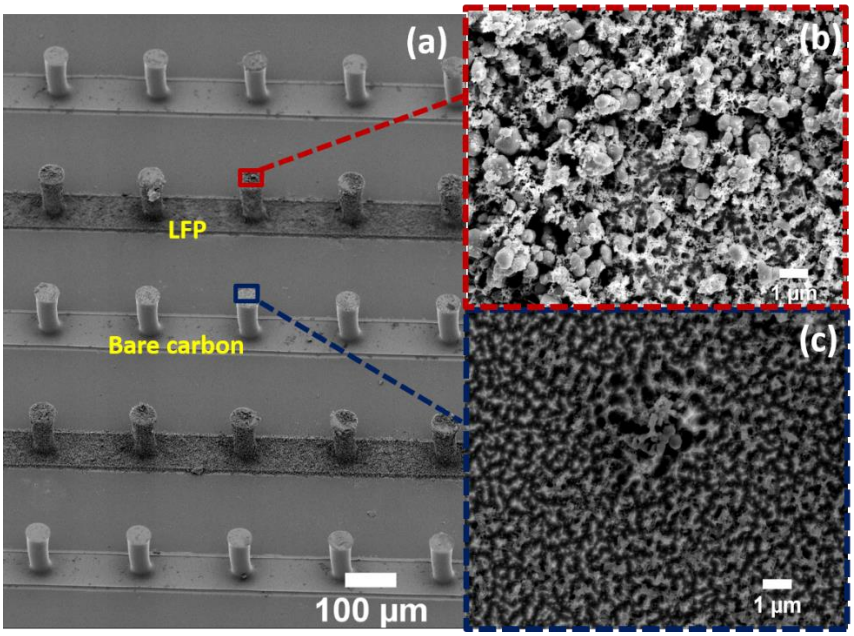

Figure 6.3**.** (a) SEM image showing the on-chip LIHC with interdigital 3D microelectrodes comprising LFP electrode material and bare carbon. An enlarged surface morphology of (b) LFP electrode material integrated on 3D carbon microelectrode after EPD process and (c) bare 3D carbon microelectrode.

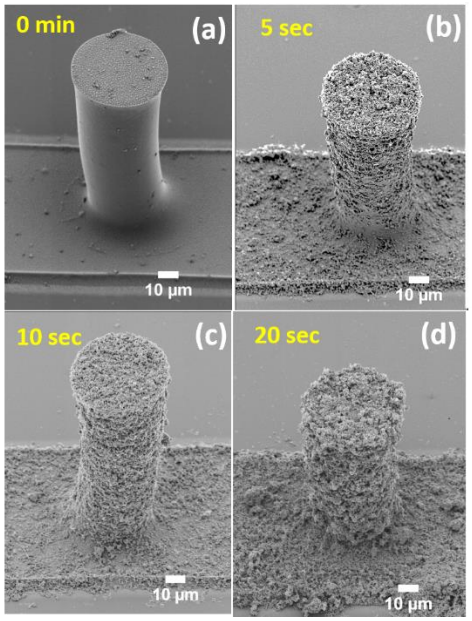

Figure 6.4. SEM images of the interdigital 3D microelectrodes with (a) 0 sec, (b) 5 sec, (c) 10 sec and (d) 20 sec LFP deposition durations.

The surface functional groups produced after plasma treatment can be observed in the FTIR pattern shown in Figure 5. An increase in the intensity of the functional group signals can be observed as plasma treatment duration increases. The broad peak at 3450 cm^{-1} is related to -OH groups of phenol or carboxylic functionalities [24], while the peak at 2930 cm^{-1} corresponds asymmetric stretching of the CH_2 functional groups [25]. The peaks at 1735 cm^{-1} can be assigned to C=O stretching of carboxyl group [26], while the 1610 cm^{-1} peak is related to C=C stretching of aromatic rings or C=O groups conjugated with aromatic rings [25]. Other peaks at 1502, 1237 and 1108 cm^{-1} are ascribed to, C=C stretching, C-O-C and C-O vibrations respectively [25,26, 28].

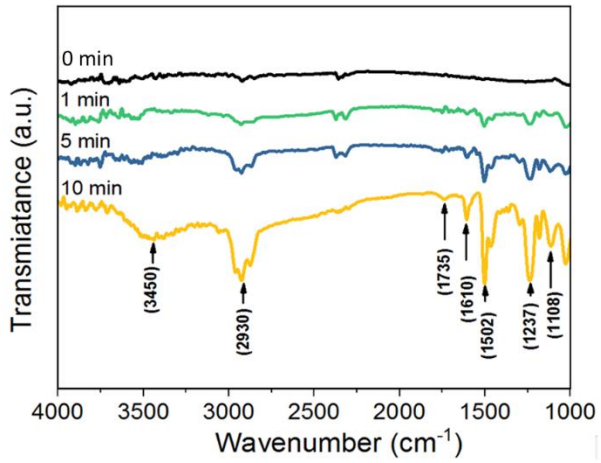

Figure 6.5**.** FTIR pattern of C-MEMS-based carbon microelectrodes with different oxygen plasma treatment times.

6.4 **Electrochemical Evaluation**

6.4.1 **Carbon//Carbon symmetric EC devices**

The third cycle CV curves of carbon//carbon symmetric ECs before and after plasma treatment based on a two-electrode configuration at a scan rate of 1 Vs^{-1} are shown in Figure 6.6a. The area under the CV curve of the treated sample is about 9 times larger than the untreated sample indicating improved charge storage behavior after plasma exposure [18]. The 5 min plasma-treated and the untreated ECs gave capacities of about 0.030 and 0.003 $\mu Ahcm^{-2}$ (normalized by device footprint area), respectively, at the 1 Vs^{-1} scan rate. Figure 6.6b shows the third cycle CV curves of 5 min plasma-treated sample at different scan rates. The corresponding capacities calculated for 5, 10, and 20 Vs^{-1} were about 0.015, 0.010 and 0.008 $\mu Ahcm^{-2}$, respectively, based on device footprint area. The enhanced capacitive performance can be attributed to the enlarged surface area as well as

pseudocapacitance contribution from surface functional groups in the oxygen plasma-treated carbon material [18, 28].

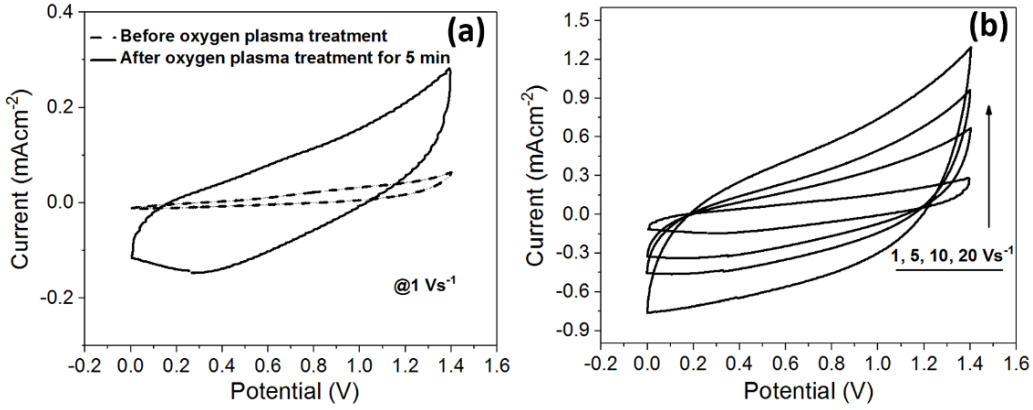

Figure 6.6: (a) CV curves of symmetric ECs with 3D carbon microelectrodes before and after oxygen plasma treatment. (b) CV curves of EC with 3D carbon microelectrodes plasma-treated for 5 min at different

The GCD curves in the two-electrode test of the 5 min plasma-treated sample at 0.12 $mAcm^{-2}$ for 10 cycles are presented in Figure 6.7. The discharge capacity based on device footprint area calculated from the GCD curves of the sample was about 1.97 $\mu Ahcm^{-2}$ after the first cycle. A slightly lower discharge capacity of ~ 1.52 $\mu Ahcm^{-2}$ was obtained after the tenth cycle.

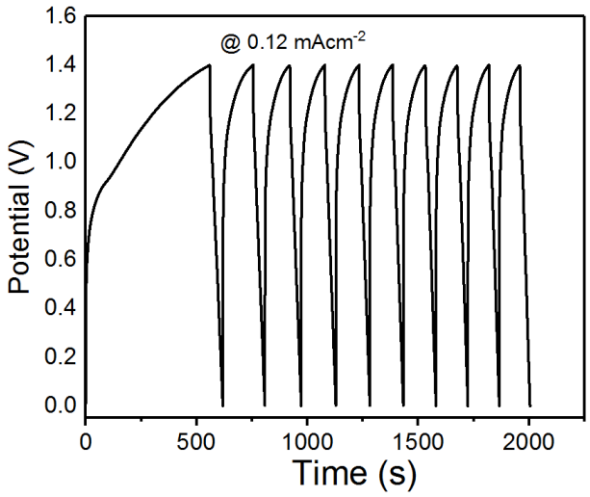

Figure 6.7: GCD curves of 5 min oxygen plasma treated sample at 0.12 mAcm-2.

The tenth cycle GCD curves of the devices at 0.36 $mAcm^{-2}$ current density for different plasma treatment durations are presented in Figure 6.8a. Among the devices, the 5 min plasma-treated sample gives the highest discharge capacity. The discharge capacities calculated from the GCD curves in Figure 6.8a for 0, 1, 5, and 10 min plasma treatment durations were about 0.001, 0.041, 0.297 and 0.138, $\mu Ahcm^{-2}$, respectively, based on device footprint area. The rate performance results presented in Figure 6.8b also shows that the 5 min plasma-treated device gave the highest discharge capacities at different current densities. The discharge capacities after the tenth cycle for the 5 min plasma-treated sample at current densities of 0.24, 0.48 and 0.60 $mAcm^{-2}$ were about 0.63, 0.18 and 0.13 $\mu Ahcm^{-2}$, respectively, based on device footprint area. A discharge capacity of 1.32 $\mu Ahcm^{-2}$ was obtained when the current density was returned to the original of level of 0.12 $mAcm^{-2}$ (after the tenth cycle) indicating that the initial capacity was fairly recovered after high current density test. Figure 6.8c shows that the 5 min plasma-treated device gave the highest capacity after 200 cycles at a constant current density of 0.24 $mAcm^{-2}$. Discharge

capacities of about 0.002, 0.060, 0.870 and 0.190 μAhcm^{-2} were obtained for 0, 1, 5, and 10 min plasma-treated samples, respectively, at 0.24 mAcm^{-2} after 200 cycles.

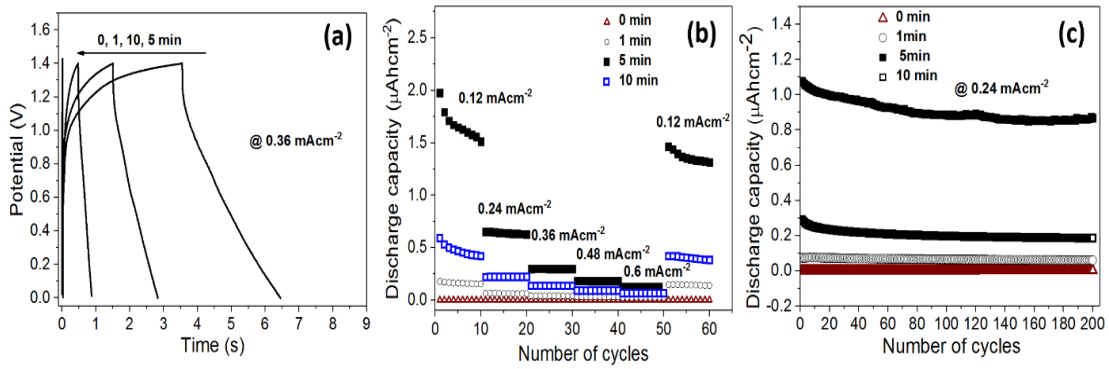

Figure 6.8 (a) GCD curves of symmetric ECs with 3D carbon microelectrodes at different oxygen plasma treatment durations. (b) Rate capability of the ECs at different current densities. (c) Cycling performance of the ECs.

6.4.2 **Three-Electrode Cells**

Figure 6.9a shows the third cycle CV curves of a carbon microelectrode after 5 min plasma treatment at different scan rates in a three-electrode setup. The shape of the CV curves is typical of capacitive behavior with the absence of obvious redox peaks within the test voltage range. The tenth cycle GCD curves of the sample at different current densities shown in Figure 6.9b. The deviation from ideal capacitive behavior may be due to redox contributions from oxygen surface functionalities in the material. The discharge capacity of the carbon microelectrode normalized by the geometric surface area is given in Figure 6.9c. The carbon microelectrode delivered about 1.70, 1.06, 0.88, 0.77, 0.68 μAhcm^{-2} discharge capacities at current densities of 0.12, 0.24, 0.36, 0.48 and 0.60 mAcm^{-2}, respectively. A discharge capacity of 1.71 μAhcm^{-2} was measured when the current density was returned to the initial level indicating the ability of the material to recover after high

current density test. The discharge capacity of the material was also stable at 0.97 μAhcm^{-2} after 200 cycles at a constant current density of 0.24 mAcm^{-2} (Figure 6.9d). The three-electrode configuration gave lower discharge capacity values than the two-electrode setup. For example, the discharge capacity value of 0.77 μAhcm^{-2} at 0.48 mAcm^{-2} for the carbon electrode material in a two-electrode configuration corresponds to about 16 times lower than the value obtained from the two-electrode test (12.47 μAhcm^{-2} at 0.12 mAcm^{-2}). The reason for this wide capacity difference is unclear at present and needs to be further examined. However, capacitance values of an electrode material depends of test cell configuration [29].

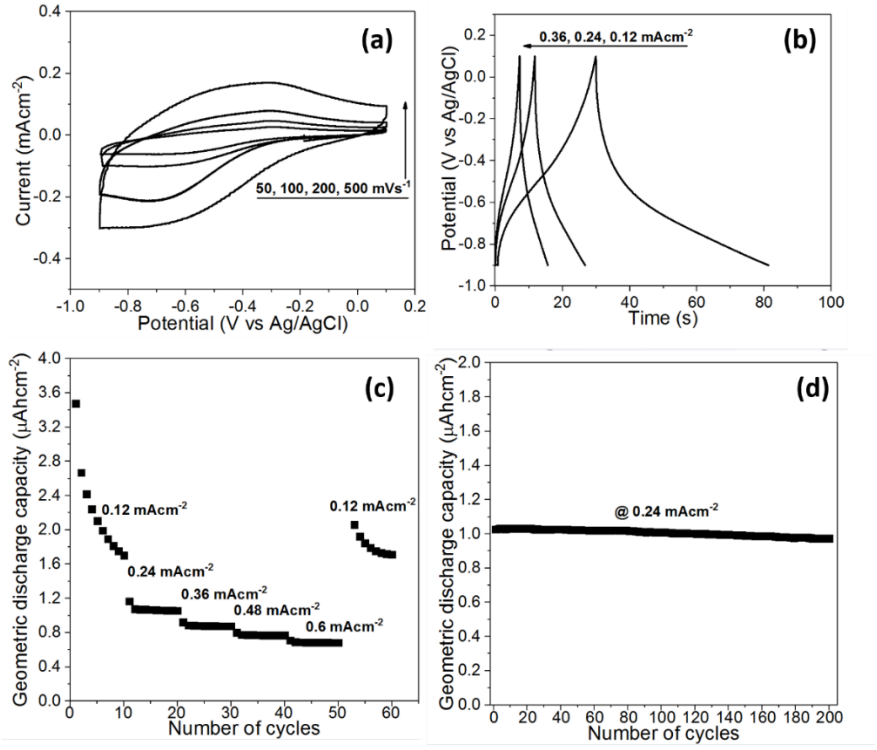

Figure 6.9. (a) CV curves of the 3D carbon microelectrode anode at different scan rates. (b) GCD curves of the anode at 0.12, 0.24, and 0.36 mAcm^{-2}. (c) Rate and (d) cycle performance of the 5 min plasma-treated carbon anode.

The charge applied across an electrode material to be analyzed (the working electrode) in a three-electrode configuration is different from a two-electrode setup. Under this condition, the capacitance value obtained from the two test configurations may not be comparable. The CV and GCD tests were also carried out on the LFP integrated on carbon microelectrode structure in a three-electrode setup. Figure 6.10a shows the typical CV curves of a sample comprising LFP electrode material with 5 sec deposition duration at a scan rate of 5 mVs^{-1}. The presence of redox activities in the material is indicated by the anodic and cathodic peaks at - 0.01 and 0.44 V, respectively. The peaks can be ascribed to the intercalation/deintercalation of lithium-ion in the LFP ($FePO_4 + xLi^+ + xe^- \leftrightarrow xLiFePO_4 + (1-x)LiFePO_4$) [30]. The tenth cycle GCD curves of the material at different current densities shown in Figure 6.10b exhibit plateau regions for both charge and discharge profile at different test current densities which also indicate the occurrence of reversible lithium-ion intercalation/deintercalation in the material [31]. The rate performance presented in Figure 6.10c shows that the LFP electrode delivered a maximum discharge capacity of 17.12 $\mu Ahcm^{-2}$ at 0.12 $mAcm^{-2}$. Discharge capacities of 9.51, 6.98, 5.28 and 4.12 $\mu Ahcm^{-2}$ were measured after 10 cycles at current densities of 0.24, 0.36, 0.48, and 0.60 $mAcm^{-2}$, respectively. A discharge capacity of 16.70 $\mu Ahcm^{-2}$ was obtained after the current density was returned to 0.12 $mAcm^{-2}$ indicating good reversibility of the LFP electrode. Result of the long term cyclability of the LFP half-cell is presented in Figure 6.10d shows a stable discharge capacity of about 8.57 $\mu Ahcm^{-2}$ at a current density of 0.24 $mAcm^{-2}$ after 100 cycles.

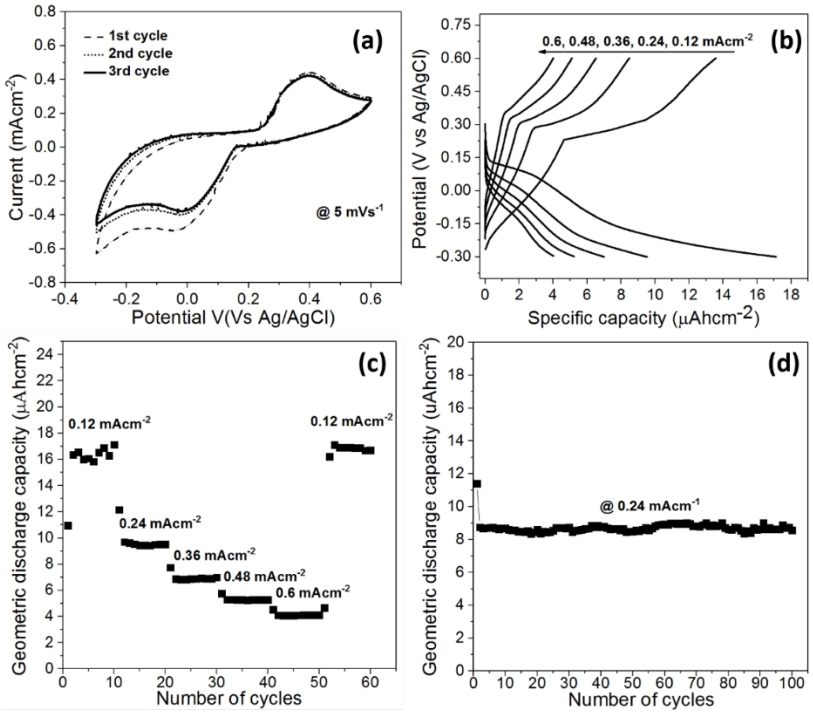

Figure 6.10**.** (a) CV curves of the LFP cathode at a scan rate of 5 mVs^{-1}. (b) GCD curves of the cathode at different current densities. (c) Rate and (d) cycle performance of the LFP cathode.

6.4.3 **Carbon//LFP LIHC Devices**

The microscale LIHCs were fabricated with 5 min plasma-treated carbon microelectrodes as anode and LFP as the cathode. To achieve optimal electrochemical performance, the LFP electrode thickness was adjusted by controlling the EPD process duration. Figure 6.11 shows the GCD curves of the first 10 cycles of the on-chip LIHC with 10 sec LFP deposition duration tested within a voltage range of 0 to 1.4 V at a current density of 0.12 $mAcm^{-2}$. The discharge capacities obtained after the first and tenth cycles were about 8.36 and 7.29 $\mu Ahcm^{-2}$, respectively, based on the device footprint area.

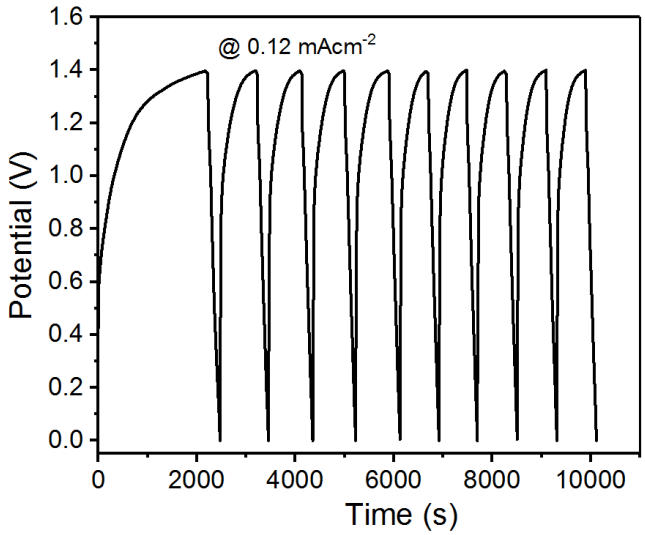

Figure 6.11: GCD curves of LIHC with 10 sec LFP deposition duration at 0.12 $mAcm^{-2}$.

Figure 6.12a shows the CV of a LIHC device with 10 sec LFP deposition duration at scan rates from 20, 50 and 200 mVs^{-1}. The nearly rectangular shape with the absence of obvious peaks on the CV curves indicate that capacitive behavior dominates in the device within a voltage range of 0 to 1.4 V. Figure 6.12b shows the tenth cycle GCD curves of the on-chip LIHC with 5, 10 and 20 sec LFP deposition durations at a current density of 0.36 $mAcm^{-2}$. The GCD curves signifies that the sample with 10 sec LFP deposition duration gave the highest discharge capacity. The discharge capacities calculated from the GCD curves were respectively about 0.46, 3.33 and 0.76 $\mu Ahcm^{-2}$ for the on-chip LIHC with 5, 10 and 20 sec LFP deposition durations. The rate performance of the on-chip LIHCs with different LFP deposition durations is presented in Figure 6.12c indicating that the on-chip LIHC with 10 sec LFP deposition duration showed the highest discharge capacities in all current densities. For example, at the highest current density of 0.60 $mAcm^{-2}$ the devices

gave discharge capacities of about 1.61, 0.35 and 0.16 μAhcm^{-2} for devices with 5, 10 and 20 sec LFP deposition durations, respectively.

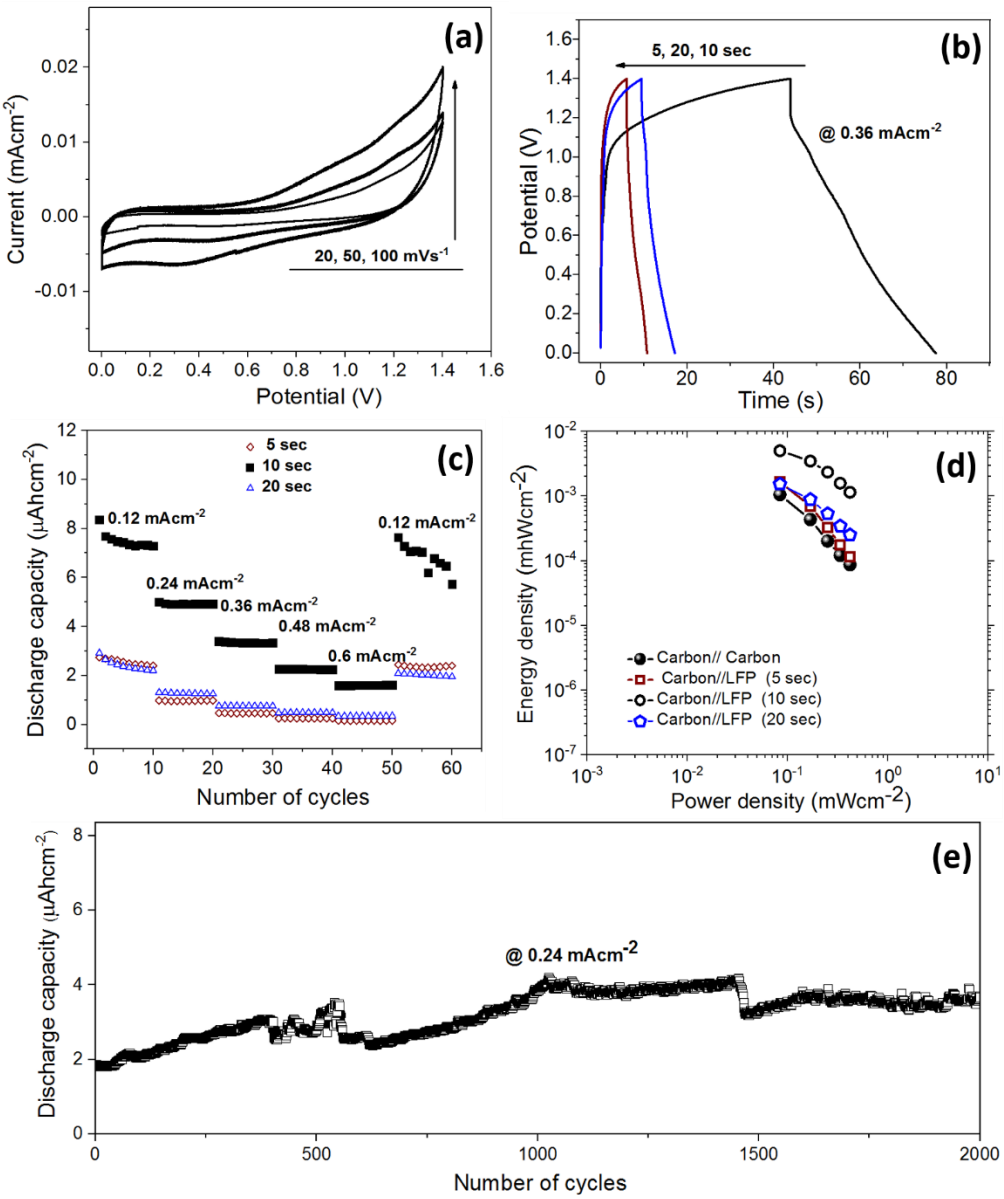

Figure 6.12. (a) CV curves at different scan rates of LIHC with 10 sec LFP deposition duration. (b) GCD profiles, (c) rate performance and (d) Ragone plot of LIHCs with different LFP deposition duration. (e) Cycle performance of LIHC with 10 sec LFP deposition at a current density of 0.24 mAcm^{-2} for 2000 cycles.

Moreover, the on-chip LIHC with 10 sec LFP deposition durations gave a discharge capacity of about 7.64 after the current density was returned to the initial level of 0.24 $mAcm^{-2}$. However, some sharp capacity decrease can be observed at about the sixth and tenth cycles upon further cycling at this current density. This may be attributed to slight detachment of LFP electrode material particles from the carbon microelectrode after being subjected to high current density. The detachment may result in the exposure of fresh electrode material particles leading to some capacity recovery as we can see in the curve. A discharge capacity of about 5.72 $\mu Ahcm^{-2}$ was obtained for the device after the tenth cycle at the 0.24 $mAcm^{-2}$ current density. The energy-power density relationship of different on-chip hybrid devices is shown in Figure 6.12d. The on-chip LIHC with 10 sec LFP deposition duration delivered the highest areal energy density with a maximum value of ~ 5.03 $\mu Whcm^{-2}$ and a maximum areal power density of ~ 0.42 $mWcm^{-2}$. The maximum areal energy densities of the devices with 5 and 20 sec LFP deposition durations were ~ 1.70 and 1.53 $\mu Whcm^{-2}$, respectively. The maximum areal energy density realized was about 5 times higher than the symmetric carbon//carbon EC which gave a maximum areal energy density of ~ 1.05 $\mu Whcm^{-2}$. The corresponding maximum volumetric energy and power densities of the on-chip LIHC with 10 sec LFP deposition duration was ~ 7.91 $\mu Whcm^{-3}$ and 0.25 Wcm^{-3}, respectively. The cyclability of the on-chip LIHC with 10 sec LFP deposition duration at a constant current density of 0.24 $mAcm^{-2}$ is presented in Figure 6.12e. The capacity increased for the first 1-550 cycles and decreased sharply at about 550th cycle. The capacity further increased after the 560th cycle until the 1450th cycle where it sharply decreased again. Thereafter, an almost steady capacity (~ 3.67 $\mu Ahcm^{-2}$) was maintained up to the 2000th cycle. The capacity increase observed at initial cycles may be

due to electro-activation process in the electrode materials of the on-chip LIHC [32-34]. Prolonged cycling may facilitate the improved accessibility of electrolyte to the active materials leading to capacity increase. Similar to the rate capability test result in Figure 8c, the sharp capacity decrease in the cyclability curve may also be attributed to the gradual detachment of LFP electrode material particles from the carbon microelectrode with prolonged cycling. Optimizing the EPD parameters for the LFP electrode material may improve the cycling stability of the LIHC. The on-chip LIHCs exhibit iR drop in the GCD curves presented in Figure 8d. The iR drop correlates to the internal resistance of the cells including ohmic resistance (R_s), ionic resistance (R_i), solid electrolyte interface resistance (R_{SEI}) and charge transfer resistance (R_{ct}) [35]. The Nyquist plots of the on-chip LIHC with different LFP deposition durations is presented in Figure S5 to give insight into the electrochemical performance results observed. The plots consist of one depressed semicircle at the high frequency region and a sloping line at the low frequency region. The intercept of the plots correlates to the R_s, while the depressed semicircle may be related to the R_{ct} [35]. The sloping line in the low frequency region represents the impedance of electrolyte ion diffusion known as the Warburg diffusion (W_s) [36, 37]. The cell with 20 sec LFP deposition duration showed the largest suppressed semicircle in the Nyquist plot which may be attributed to high R_i in the cell. The R_i may be influenced by the resulting electrode porosity with prolonged LFP deposition durations. The LFP electrode structure after prolonged EPD process may exhibit the smallest pore structure distribution due to a dense packing of electrode material particles leading high ion transport resistance [38].

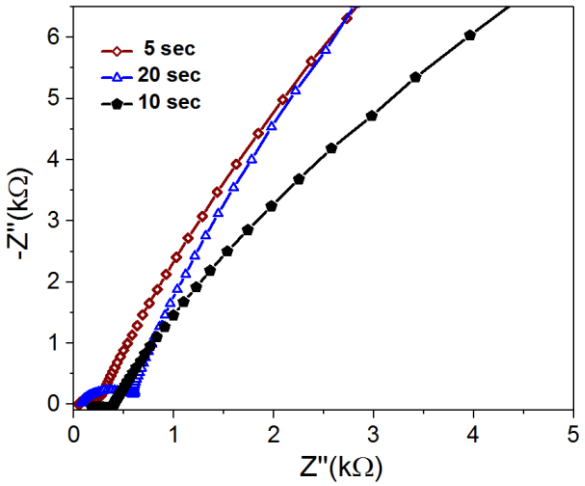

Figure 6.13: Nyquist plots of the LIHC with different LFP deposition durations.

The performance comparison of the on-chip LIHC demonstrated in this work with other microscale ECs described in literature is presented in Table 6.1. We can see from Table 6.1 that the maximum volumetric energy density of our on-chip LIHC exceeds microscale some symmetric and asymmetric reported in literature.

Table 6.1: Performance comparison with other aqueous microscale ECs

`Anode	**Cathode**	**Electrolyte**	**Potential window (V)**	**Maximum volumetric power density (Wcm^{-3})**	**Maximum volumetric energy density ($mWhcm^{-3}$)**	**Ref.**
$K_2Co_3(P_2O_7)_2.2H_2O$	*$K_2Co_3(P_2O_7)_2.2H_2O$*	*PVA/KOH*	*0-1.07*	*54.5*	*0.96*	[39]
MOS_2@rGO-CNT	*MOS_2@rGO-CNT*	*PVA/H_2SO_4*	*0-1*	-	*5.6*	[40]
Graphene	*Graphene*	*PVA/H_2SO_4*	*0-0.8*	*0.3*	*1.41*	[41]
CNT	*CNT*	*PVA/H_3PO_4*	*0-0.8*	*0.4*	*0.18*	[42]
rGO	*MnO_x*	*1 M Na_2SO_4*	*0-1.1*	*3.44*	*1.02*	[43]
VOx/rGO	*VN/rGO*	*LiCl/PVA*	*0- 1.6*	-	*1.74*	[44]
Carbon	*$LiFePO_4$*	*1 M Li_2SO_4*	*0-1.4*	*0.25*	*7.91*	*This work*

A high operating potential is one of the main requirements for high energy density in electrochemical energy storage systems. In this study, a maximum operating potential of 1.4 V was attained in contrast to the typical 1 V in aqueous electrolyte systems due to irreversible water hydrolysis at ~ 1.2 V. It has been previously described that the Li_2SO_4 electrolyte salt employed in this study exhibit strong Li^+ and SO_4^{2-} solvation which may suppress water hydrolysis and expand the operation potential [45]. This is an initial study on the application of C-MEMS technique for the development of on-chip LIHC. Future efforts will include capacity and rate performance matching of the capacitor-type carbon microelectrode with the battery-type cathode to ensure optimal performance of the on-chip LIHC system. It is also expected that improving the capacitive behavior of the carbon microelectrode, the incorporation of other battery-type electrode materials capable of providing faster kinetics or employing high voltage electrolytes would ensure higher energy-power density tradeoffs in the on-chip LIHC system. The C-MEMS approach demonstrated in this study exhibits promising potential for the facile development of high-performance on-chip LIHCs with 3D microelectrodes.

6.4 **Conclusion**

The construction and evaluation of an aqueous on-chip LIHC with C-MEMS-based interdigital 3D carbon microelectrodes was described in this study. Oxygen plasma-treated 3D carbon microelectrodes served as the capacitor-type electrode in the LIHC, while LFP integrated on the carbon microelectrodes was used as the battery-type cathode. The

carbon//LFP LIHC delivered an areal energy density up to ~ 5.03 μWhcm^{-2}, about 5 times higher than symmetric 3D carbon microelectrode EC evaluated. The approach described in this study may provide a promising alternative for the development of on-chip LIHCs as energy storage units for miniaturized electronic devices.

6.5 References

1. P. Huang *et al.*, "On-chip and freestanding elastic carbon films for micro-supercapacitors," *Science (80-.).*, vol. 351, no. 6274, pp. 3717–3720, 2016.

2. M. F. El-kady and R. B. Kaner, "Scalable fabrication of high-power graphene micro-supercapacitors for flexible and on-chip energy storage," *Nat. Commun.*, vol. 4, pp. 1475–1479, 2013.

3. P. Simon and Y. Gogotsi, "Materials for electrochemical capacitors," *Nature*, vol. 7, pp. 845–854, 2008.

4. J. Jiang *et al.*, "Progress of Nanostructured Electrode Materials for Supercapacitors," *Adv. Sustain. Syst.*, vol. 2, p. 1700110, 2018.

5. J. W. Long, D. Bélanger, T. Brousse, W. Sugimoto, M. B. Sassin, and O. Crosnier, "Asymmetric electrochemical capacitors — Stretching the limits of aqueous electrolytes," *MRS Bull.*, vol. 36, pp. 513–522, 2011.

6. H. Gao, F. Xiao, C. B. Ching, and H. Duan, "High-Performance Asymmetric Supercapacitor Based on Graphene Hydrogel and Nanostructured MnO 2," *ACS Appl. Mater. Interfaces*, vol. 4, pp. 2801–2810, 2012.

7. T. Brousse and B. Daniel, "To Be or Not To Be Pseudocapacitive ?," *J. Electrochem. Soc.*, vol. 162, no. 5, pp. 5185–5189, 2015.

8. Y. Shao *et al.*, "Design and Mechanisms of Asymmetric Supercapacitors," *Chem. Rev.*, vol. 118, pp. 9233–9280, 2018.

9. G. G. Amatucci, F. Badway, A. Du Pasquier, and T. Zheng, "An Asymmetric Hybrid Nonaqueous Energy Storage Cell," *J. Electrochem. Soc.*, vol. 148, no. 8, pp. A930–A939, 2001.

10. D. Cericola and R. Kötz, “Electrochimica Acta Hybridization of rechargeable batteries and electrochemical capacitors : Principles and limits,” *Electrochim. Acta*, vol. 72, pp. 1–17, 2012.

11. S. Li and X. Wang, “Micro Li-ion capacitor with activated carbon / graphite con fi guration for energy storage,” *J. Power Sources*, vol. 282, pp. 394–400, 2015.

12. N. A. Kyerematen, T. Brousse, and D. Pech, “Microsupercapacitors as miniaturized energy- storage components for on-chip electronics,” *Nat. Publ. Gr.*, vol. 12, no. 1, pp. 7–15, 2016.

13. J. Pu, T. Zhang, and J. Liu, “High-energy-density , all-solid-state microsupercapacitors with three- dimensional interdigital electrodes of carbon / polymer electrolyte composite,” *Nanotechnology*, vol. 27, p. 045701, 2015.

14. C. Shen, X. Wang, W. Zhang, and F. Kang, “A high-performance three-dimensional micro supercapacitor based on self-supporting composite materials ☪,” *J. Power Sources*, vol. 196, no. 23, pp. 10465–10471, 2011.

15. R. Agrawal, E. Adelowo, A. R. Baboukani, M. F. Villegas, A. Henriques, and C. Wang, “Electrostatic Spray Deposition-Based Manganese Oxide Films — From Pseudocapacitive Charge Storage Materials to Three-Dimensional Microelectrode Integrands,” *Nanomaterials*, vol. 7, no. 198, 2017.

16. C. Lethien and L. Bideau, “Environmental Science micro-supercapacitors for powering the internet of things,” *Energy Environ. Sci.*, vol. 12, p. 96, 2019.

17. R. Agrawal, E. Adelowo, A. R. Baboukani, M. F. Villegas, A. Henriques, and C. Wang, “Electrostatic Spray Deposition-Based Manganese Oxide Films — From Pseudocapacitive Charge Storage Materials to Three-Dimensional Microelectrode Integrands,” *Nanomaterials*, vol. 7, p. 198, 2017.

18. M. Beidaghi, W. Chen, and C. Wang, “Electrochemically activated carbon micro-electrode arrays for electrochemical,” *J. Power Sources*, vol. 196, no. 4, pp. 2403–2409, 2011.

19. F. Galobardes, C. Wang, and M. Madou, “Investigation on the solid electrolyte interface formed on pyrolyzed photoresist carbon anodes for C-MEMS lithium-ion batteries,” *Diam. Relat. Mater.*, vol. 15, pp. 1930–1934, 2006.

20. H. Min *et al.*, “Fabrication and properties of a carbon / polypyrrole three-dimensional microbattery,” *J. Power Sources*, vol. 178, pp. 795–800, 2008.

21. C. Wang, G. Jia, L. H. Taherabadi, and M. J. Madou, “A novel method for the fabrication of high-aspect ratio C-MEMS structures,” *J. Microelectromechanical Syst.*, vol. 14, no. 2, pp. 348–358, 2005.

22. W. Chen *et al.*, “Integration of Carbon Nanotubes to C-MEMS for On-chip Supercapacitors,” *IEEE Trans. Nanotechnol.*, vol. 9, no. 6, pp. 734–740, 2010.

23. M. Beidaghi and C. Wang, “Micro-supercapacitors based on three dimensional interdigital polypyrrole/C-MEMS electrodes,” *Electrochim. Acta*, vol. 56, no. 25, pp. 9508–9514, 2011.

24. M. Domingo-Garcıa, F. J. Lopez-Garzon, and M. Perez-Mendoza, “Effect of Some Oxidation Treatments on the Textural Characteristics and Surface Chemical Nature of an Activated Carbon,” *J. Colloid Interface Sci.*, vol. 240, pp. 233–240, 2000.

25. A. Shindo and K. Izumino, “Structural Variation During Pyrolysis of Furfuryl Alcohol and Furfural-Furfuryl Alcohol Resins,” *Carbon N. Y.*, vol. 32, no. 7, pp. 1233–1243, 1994.

26. L. G. Nair, A. S. Mahapatra, N. Gomathi, K. Joseph, S. Neogi, and C. P. R. Nair, “Applied Surface Science Radio frequency plasma mediated dry functionalization of multiwall carbon nanotube,” *Appl. Surf. Sci.*, vol. 340, pp. 64–71, 2015.

27. L. Lai *et al.*, “Preparation of Supercapacitor Electrodes through Selection of Graphene Surface Functionalities,” *ACS Nano*, vol. 6, no. 7, pp. 5941–5951, 2012.

28. J. Niu, W. G. Pell, and B. E. Conway, “Requirements for performance characterization of C double-layer supercapacitors : Applications to a high specific-area C-cloth material,” *J. Power Sources*, vol. 156, pp. 725–740, 2006.

29. V. Khomenko and E. Frackowiak, “Determination of the specific capacitance of conducting polymer / nanotubes composite electrodes using different cell configurations,” *Electrochim. Acta*, vol. 50, pp. 2499–2506, 2005.

30. P. He, J. Liu, W. Cui, J. Luo, and Y. Xia, “Electrochimica Acta Investigation on capacity fading of LiFePO 4 in aqueous electrolyte,” *Electrochim. Acta*, vol. 56, no. 5, pp. 2351–2357, 2011.

31. P. He, X. Zhang, Y. Wang, L. Cheng, and Y. Xia, “Lithium-Ion Intercalation Behavior of LiFePO 4 in Aqueous and Nonaqueous Electrolyte Solutions,” *J. Electrochem. Soc.*, vol. 155, pp. 144–150, 2008.

32. H. Wang, Q. Hao, X. Yang, L. Lu, and X. Wang, “A nanostructured graphene / polyaniline hybrid material for supercapacitors,” *Nanoscale*, vol. 2, pp. 2164–2170, 2010.

33. M. Beidaghi and C. Wang, “Electrochimica Acta Micro-supercapacitors based on three dimensional interdigital polypyrrole / C-MEMS electrodes,” *Electrochim. Acta*, vol. 56, no. 25, pp. 9508–9514, 2011.

34. M. Beidaghi and C. Wang, “Micro-Supercapacitors Based on Interdigital Electrodes of Reduced Graphene Oxide and Carbon Nanotube Composites with Ultrahigh Power Handling Performance,” *Adv. Funct. Mater.*, vol. 22, pp. 4501–4510, 2012.

35. P. L. Moss, G. Au, E. J. Plichta, and J. P. Zheng, “Investigation of solid electrolyte interfacial layer development during continuous cycling using ac impedance spectra and micro-structural analysis,” *J. Power Sources*, vol. 189, pp. 66–71, 2009.

36. W. J. Cao and J. P. Zheng, “Li-ion capacitors with carbon cathode and hard carbon / stabilized lithium metal powder anode electrodes,” *J. Power Sources*, vol. 213, pp. 180–185, 2012.

37. P. Pazhamalai, K. Krishnamoorthy, and M. S. P. Sudhakaran, “Fabrication of High-Performance Aqueous Li-Ion Hybrid Capacitor with LiMn 2 O 4 and Graphene,” *chemelectrochem*, vol. 4, pp. 396–403, 2017.

38. C. Hitz and A. Lasia, “Experimental study and modeling of impedance of the her on porous Ni electrodes,” *J. Electroanal. Chem.*, vol. 500, pp. 213–222, 2001.

39. H. Pang, Y. Zhang, and W. Lai, “Lamellar K 2 Co 3 (P 2 O 7) 2 . 2H 2 O nanocrystal whiskers : High-performance fl exible all-solid-state asymmetric micro-supercapacitors via inkjet printing,” *Nano Energy*, vol. 3, pp. 303–312, 2015.

40. W. Yang, L. He, X. Tian, M. Yan, H. Yuan, and X. Liao, “Carbon-MEMS-Based Alternating Stacked MoS 2 @ rGO- CNT Micro-Supercapacitor with High Capacitance and Energy Density,” *Small*, vol. 13, p. 1700639, 2017.

41. Q. Zhang, L. Huang, Q. Chang, W. Shi, L. Shen, and Q. Chen, “Gravure-printed interdigital microsupercapacitors on a fl exible polyimide substrate using crumpled graphene ink,” *Nanotechnology*, vol. 27, p. 105401, 2016.

42. L. Liu, D. Ye, Y. Yu, L. Liu, and Y. Wu, “Carbon-based fl exible micro-supercapacitor fabrication via mask-free ambient micro-plasma-jet etching,” *Carbon N. Y.*, vol. 111, pp. 121–127, 2017.

43. R. Agrawal and C. Wang, “On-Chip Asymmetric Microsupercapacitors Combining Reduced Graphene Oxide and Manganese Oxide for High Energy-Power Tradeoff,” *Micromachines*, vol. 9, p. 399, 2018.

44. K. Shen, J. Ding, and S. Yang, “3D Printing Quasi-Solid-State Asymmetric Micro-Supercapacitors with Ultrahigh Areal Energy Density,” *Adv. Energy Mater.*, vol. 1800408, pp. 1–7, 2018.

45. K. Fic, G. Lota, M. Meller, and E. Frackowiak, “Novel insight into neutral medium as electrolyte for high-voltage supercapacitors,” *Energy Environ. Sci.*, vol. 5, pp. 5842–5850, 2012.

CHAPTER 7

Summary and Future Work

7.1 Summary

This dissertation presents the design, fabrication, and evaluation of both scale-up and on-chip LIHCs. The traditional LIHC system predominantly based on the combination of bulk storage and surface charge storage mechanisms present challenges related to kinetics and capacity mismatch between the battery-type anode and capacitor-type cathode. Moreover, the most widely employed battery-type material based on bulk storage mechanism exhibit limited cyclability, which restricts long term operation of LIHCs. Furthermore, considering the potential of LIHC to provide high energy capacitive energy storage, it is desirable to extend the concept to on-chip ECs.

The scale-up system involves the application of nanostructured carbon capable of providing high capacity and good ion transport kinetics. In the LIHC system, rGO-CNT prepared by ESD was employed as both anode and cathode. The rGO-based material was partially reduced and contained residual oxygen functionalities after the ESD process. As the anode materials, the high specific surface area of rGO-CNT can enable rapid and high lithium storage capacity through electrochemical adsorption/desorption of lithium-ions. Considering the material as a cathode, the residual oxygen functionalities of the rGO-CNT can act as redox active sites to reversibly trap lithium-ions at high voltage to give rapid and high lithium storage capacity. The LIHC assembled with rGO-CNT are therefore fully enabled to provide high capacity and rapid reversible surface charge/discharge characteristics.

Anode prelithiation plays a vital role in realizing high electrochemical performance in the scale-up LIHC. Electrochemical and direct lithium contact prelithiation methods were implemented on the anode side of the LIHC to achieve higher cell voltage and improved energy density. The LIHCs delivered energy densities multiple times higher than symmetric EC employing the same rGO-CNT material. The LIHCs also gave electrochemical performance characteristics intermediate between LIBs and ECs. This rGO-based material configuration may set a different path for realizing high energy density and high power density trade-off of LIHC system.

A novel on-chip LIHC was demonstrated with 3D interdigital carbon microelectrodes derived by a scalable fabrication process based on C-MEMS technique. The carbon microelectrodes were subjected to oxygen plasma treatment to give enhanced discharge capacity. The oxygen plasma-treated carbon microelectrode was used as a capacitor-type cathode while battery-type LFP was integrated on the 3D carbon structures by EPD to realize the on-chip LIHC system. The LFP thickness was adjusted to achieve optimum electrochemical performance. The on-chip LIHC device evaluated in an aqueous electrolyte shows superior areal electrochemical performance compared with the best symmetric 3D interdigital carbon microelectrodes with a footprint area normalized energy density up to ~ 5.03 $\mu Whcm^{-2}$.

The proposed approaches demonstrated in this dissertation suggest new prospects for the development of high-performance scale-up and on-chip LIHC devices. Partially reduced graphene oxide-based films derived by ESD with features such as high capacity and good ion transport kinetics could play an important role in the practical implementation of high-performance all-rGO-based LIHC. This study also opens a new possibility in the

development of high-performance on-chip ECs with the demonstration of an on-chip LIHC using high aspect ratio 3D carbon platform based on C-MEMS technology.

7.2 Future Work

As demonstrated in this dissertation, partially reduced GO-CNT can provide high capacity and good kinetics for application as both anode and cathode in LIHC. However, there is still a huge capacity and kinetics difference between the anode and cathode in the LIHC. The dominant mechanism in the material as a function of film thickness needs to be determined. A film thickness range of ~ 2.5 to 5.2 μm was employed in this study but the influence of the rGO-CNT film thickness on the ion transport kinetics and discharge capacity needs to be well established to realize a balanced LIHC system. A combination of theoretical modeling and experimental balancing method and will be useful in realizing the full potential of the LIHC system.

There is the need to develop strategies to optimize the anode prelithiation process in the rGO-based LIHC. The direct contact rGO-CNT anode prelithiation method described in chapter 4 appear promising. However, it remains challenging to control the degree of prelithiation for implementation in commercial large-scale device assembly. Identifying the factors influencing the lithium doping kinetics when applying the prelithiation method may provide information on how to control the degree of prelithiation in the rGO-based material for the fabrication of high-performance LIHC. The role of material thickness (both active material and lithium foil), as well as their surface morphologies on the lithium doping kinetics of the rGO-based material, should be examined.

One of the main accomplishments of this work is the development of on-chip LIHC with 3D carbon microelectrodes derived by C-MEMS technique. The 3D carbon microelectrodes can be further modified to give enhanced discharge capacity as capacitor-type electrode to match up with the high capacity LFP electrode. Moreover, the carbon microelectrodes sometimes delaminate from the surface of the wafer. Further efforts should focus on how to improve the adhesion of carbon microelectrodes to the silicon wafer. One of the major advances in this on-chip LIHC will be the replacement of liquid electrolyte with a high voltage solid electrolyte. Effort in this direction has started with half-cell studies on the application of a gel polymer electrolytes (GPE) consisting of ionic liquids (ILs) and a lithium salt incorporated. IL-based GPE are highly attractive for future energy storage devices[1-3]. ILs are generally non-flammable and exhibit remarkably wide electrochemical stability window [4]. IL-based GPE can give advantageous attributes such as freedom from leakage ease of packaging and improved energy density due to wider voltage range. A well-packaged high-performance on-chip LIHC with 3D carbon microelectrodes and IL-based GPE may provide a standalone compact and integrable microscale high energy density capacitive energy storage for miniature electronic devices.

7.3 References

1. F. Croce, S. Sacchetti, and B. Scrosati, “Advanced , high-performance composite polymer electrolytes for lithium batteries,” vol. 161, pp. 560–564, 2006.

2. J. W. Fergus, “Ceramic and polymeric solid electrolytes for lithium-ion batteries,” *J. Power Sources*, vol. 195, no. 15, pp. 4554–4569, 2010.

3. M. Safa, A. Chamaani, N. Chawla, and B. El-zahab, “Electrochimica Acta Polymeric Ionic Liquid Gel Electrolyte for Room Temperature Lithium Battery Applications,” vol. 213, pp. 587–593, 2016.

4. F. Croce, S. Sacchetti, and B. Scrosati, “Advanced , high-performance composite polymer electrolytes for lithium batteries,” *J. Power Sources*, vol. 161, pp. 560–564, 2006.

VITA

EBENEZER DOTUN ADELOWO

2019	Ph.D. Candidate, Materials Science and Engineering, Florida International University, Miami, FL, USA.
2012	M.Sc. Materials Engineering, Obafemi Awolowo University, Ile-Ife, Nigeria.
2008	B.Sc. Metallurgical and Materials Engineering, Obafemi Awolowo University, Ile-Ife, Nigeria.

Awards and Honors:

- Graduate Teaching/Research Assistantship, MME, FIU(*2015;2016;2017; 2018)*
- Dissertation Year Fellowship, Florida International University (2018)

Publications

1. Adelowo, E., Baboukani, A. R., Chen C., and Wang, C., Electrostatically sprayed reduced graphene oxide-carbon nanotubes electrodes for lithium-ion capacitors, C-Journal of Carbon Research, 2018, 4,31.

2. Agrawal, R., Adelowo, E., Baboukani, A. R., Villegas, M. F., Henriques, A., Wang, C., Electrostatic Spray Deposition Based Manganese Oxide Films – From Pseudocapacitive Charge Storage Materials To Three-dimensional Microelectrode Integrands, Nanomaterials 2017, 7, 198.

3. Safa, M., Hao Y., Chamaani, A., Adelowo, E., Chawla N., Wang, C., El-Zahab B., Capacity Fading Mechanism in Lithium-Sulfur Battery using Poly(Ionic Liquid) Gel Electrolyte, Electrochimica Acta, 2017,258, 1284-1292.

4. Adelowo, E., Baboukani, A. R., Agrawal, R., and Wang, C., Electrochemical Performance of Lithium-Ion Capacitor Using Reduced Graphene Oxide–Carbon Nanotube Pre-Lithiated by Direct Contact Method ECS Trans. 2018 85,13, 469-474.

5. Rabiei Baboukani A., Adelowo E., Agrawal R., Khakpour I., Drozd V., Li W., Wang C., Electrostatic Spray Deposited Sn-SnO2-CNF Composite Anodes for Lithium Ion Storage ECS Trans. 2018 85,13, 331-336.

6. Adelowo, E., Agrawal, R., Okpowe, O., Rabiei Baboukani, A., Wang, C., Development of high-performance hybrid capacitors, Energy Harvesting and Storage: Materials, Devices, and Applications IX, Proceedings of SPIE, 2019, 1097907.

7. Adelowo, E., Baboukani, A., and Wang, C., Lithium-Ion Capacitors Based on Reduced Graphene Oxide/Carbon Nanotube Thin Films Fabricated by Electrostatic Spray Deposition, 233rd ECS Meeting, Seattle, WA, May 13-17, 2018.

8. Adelowo, E. Agrawal, R., and Wang, C., Lithium-Ion Capacitor Based on $LiFePO_4$ and Nanostructured Carbon By Electrostatic Spray Deposition, 231stECS Meeting, New Orleans, LA, May 28-June1, 2017.

9. Rabiei Baboukani A., Adelowo E., Agrawal R., Khakpour I., Drozd V., Li W., Wang C., Electrostatic Spray Deposited Sn-SnO2-CNF Composite Anodes for Lithium Ion Storage, 233rd ECS conference 2018, Seattle, WA, May 12-17, 2018.